Geometry and Construction of Upper Crustal Intrusions; Sawtooth Ridge, Henry Mountains, Southern Utah.

by

Tanner Evan Eischen

July, 2020

Director of Thesis: Eric Horsman

Major Department: Geological Sciences

The plumbing systems of volcanos are commonly constructed by interconnected, upper crustal sheet intrusions (i.e. dikes and sills). Active systems and the processes that contribute to their construction are difficult to study directly, but it is possible to indirectly observe these processes by studying ancient upper crustal intrusions now exposed at the surface. The Sawtooth Ridge intrusion is one such shallow, Oligocene intrusion located on the northeastern margin of Mount Hillers in the Henry Mountains of southern Utah. While many adjacent and similarly sized intrusions are well understood (Maiden Creek Sill, Trachyte Mesa laccolith, Black Mesa Bysmalith), previous works concerning the Sawtooth Ridge intrusion have been inconclusive. Through a combination of field and lab techniques, constraints are provided on the emplacement history and subsurface geometry of the Sawtooth Ridge intrusion, and subsequently, the processes responsible for its construction.

Field mapping suggests the first- and second-order geometries of the Sawtooth Ridge intrusion are more complex than a traditional dike or sill. The intrusion extends approximately 4 km from the northeast flank of Mount Hillers with an irregular, step-like upper surface. Lobes of igneous rock separate islands of sedimentary host rock and several dikes extend perpendicularly from the main crest of the intrusion. Along with geochemical data, this suggests that the intrusion was built incrementally through the injection of two or more batches of magma. Data from field observations and petrofabric analysis suggest that magma from the Mount Hillers intrusive center was transported sub-vertically towards the NE to construct the Sawtooth Ridge intrusion. Magnetic anomaly modelling suggests that the subsurface geometry of the main intrusive body is most accurately represented by a series of parallel, dike/tube

hybrids. Data suggest a three-step model of construction in which a series of parallel dike/feeder tubes intruded from the southwest. As the magma ascended to a critical elevation, the minimum stress direction was no longer oriented horizontally, causing magma to transition to a tube- or tongue-like propagation. As this intrusive stage inflated to a critical aspect ratio, principal stress directions rotated again causing magma to be emplaced as vertical dikes extending perpendicularly from the main intrusive body.

Geometry and Construction of Upper Crustal Intrusions

Sawtooth Ridge, Henry Mountains, Southern Utah

A Thesis

Presented to the Faculty of the Department of Geological Sciences

East Carolina University

In Partial Fulfillment of the Requirements for the Degree

Master of Science in Geology

By

Tanner E. Eischen

July, 2020

GEOMETRY AND CONSTRUCTION OF UPPER CRUSTAL INTRUSIONS, SAWTOOTH RIDGE, HENRY MOUNTAINS, SOUTHERN UTAH

by

Tanner Evan Eischen

APPROVED BY:

DIRECTOR OF THESIS:_____
Eric Horsman, PhD

COMMITTEE MEMBER:_____
Scott Giorgis, PhD

COMMITTEE MEMBER:_____
Adriana Heimann, PhD

COMMITTEE MEMBER:_____
Terri Woods, PhD

DEPARTMENT CHAIRPERSON:_____
Stephen Culver, PhD

DEAN OF THE
GRADUATE SCHOOL:_____
Paul J. Gemperline, PhD

Acknowledgements

Most of all I would like to thank my advisor Dr. Eric Horsman whose guidance in field/lab work and scientific writing were essential in completing this project. Not only that, with his encouragement, support, and willingness to fulfill my endless requests for letters of recommendation he has assisted greatly in the progression of my Earth science career.

I would like to thank my committee members Dr. Terri Woods, Dr. Adriana Heimann, and Dr. Scott Giorgis for both the review of my thesis, and the support they provided during my time as an M.S. student.

I would like to thank the East Carolina University Department of Geological Sciences for allowing me to pursue an M.S. degree.

Finally, I would like to thank the National Science Foundation and the Geological Society of America for providing funding for my research.

Table of Contents

List of Figures

1. Introduction

The plumbing systems beneath volcanos are constructed from the successive emplacement of shallow intrusions. Because plumbing systems and their construction produce volcanic/magmatic hazards, geothermal energy, and economic mineral deposits it is useful to study magma transport and intrusion assembly in the upper crust (e.g. Magee et al., 2016). However, it is difficult to directly study *active* upper crustal magma systems and the processes behind their construction through methods other than geophysics or geodesy (e.g. Horsman et al., 2018). Ancient upper crustal igneous intrusions now exposed at the surface provide an opportunity to indirectly observe these construction processes.

It is understood that many shallow plutons are constructed incrementally from numerous relatively small magma injections, rather than cooling from one large body of magma. Various characteristics can provide evidence for incremental assembly in ancient upper crustal intrusions, and detailed field work and fabric analysis have documented pulsed construction ranging from the batholith- to individual-sill-scale (Saint Blanquat et al., 2001, 2011; Glazner et al., 2004). Unfortunately, evidence of incremental assembly can be complicated by a lack of exposure and the presence of syn- or post-tectonic overprint. The Henry Mountains in southern Utah are a group of upper crustal igneous intrusions with excellent exposures and a lack of tectonic overprint, allowing us to circumvent some of these complications.

The Henry Mountains are a suite of five Oligocene intrusive centers (Nelson et al., 1992), and represent a great analogue to modern upper crustal magma systems (Fig. 1). This study focuses on the Sawtooth Ridge intrusion extending approximately four kilometers from the eastern flank of Mount Hillers. The Sawtooth Ridge intrusion, for many reasons, provides an

excellent opportunity to study the shallow construction processes of subvolcanic systems. First, as with many of the Henry Mountains intrusions, exposure of igneous rock and contacts with sedimentary host-rock are exceptional (Fig. 2). Second, the intrusion was emplaced into originally sub horizontal strata during a period of no regional deformation and experienced no post-emplacement tectonic activity. This ensures that igneous rock has experienced no tectonic overprint, which often complicate interpretations (e.g. Paterson et al., 1998; Saint-Blanquat et al., 2011). This relative simplicity means that magmatic fabrics and deflection of host rock can be interpreted as a product of magmatic processes (Horsman et al., 2010). Third, previous work concerning the geometry of the Sawtooth Ridge intrusion has been inconclusive (Hunt et al., 1953; Murdoch, unpublished mapping). Hunt et al. (1953) hypothesize that Sawtooth Ridge is either a dike with discordant contacts or a horizontal pipe with more-or-less concordant contacts. The NE end of the Sawtooth Ridge intrusion appears to display a tube or pipe-like geometry (Fig. 2). However, many similarly sized intrusions within the Henry Mountains display either a sheet- or tongue-like geometry (e.g. Maiden Creek sill, Trachyte Mesa laccolith, and the Copper Ridge laccolith; Horsman et al., 2005; Morgan et al., 2008; Maurer, 2015). Is the Sawtooth Ridge intrusion a dike/series of dikes? A sill? A tube? A tongue? Or some type of hybrid?

The goal of this study is to constrain the geometry of the Sawtooth Ridge intrusion and the processes behind the construction of this small upper crustal intrusion in the Henry Mountains region. To accomplish this goal methods including field observations, major- and trace-element geochemistry, anisotropy of magnetic susceptibility, shape preferred orientation, and magnetic anomaly modelling were used. These techniques test two hypotheses: 1) the Sawtooth Ridge intrusion displays a complex geometry unlike adjacent intrusions and 2) the Sawtooth Ridge intrusion was constructed through two or more smaller component intrusions.

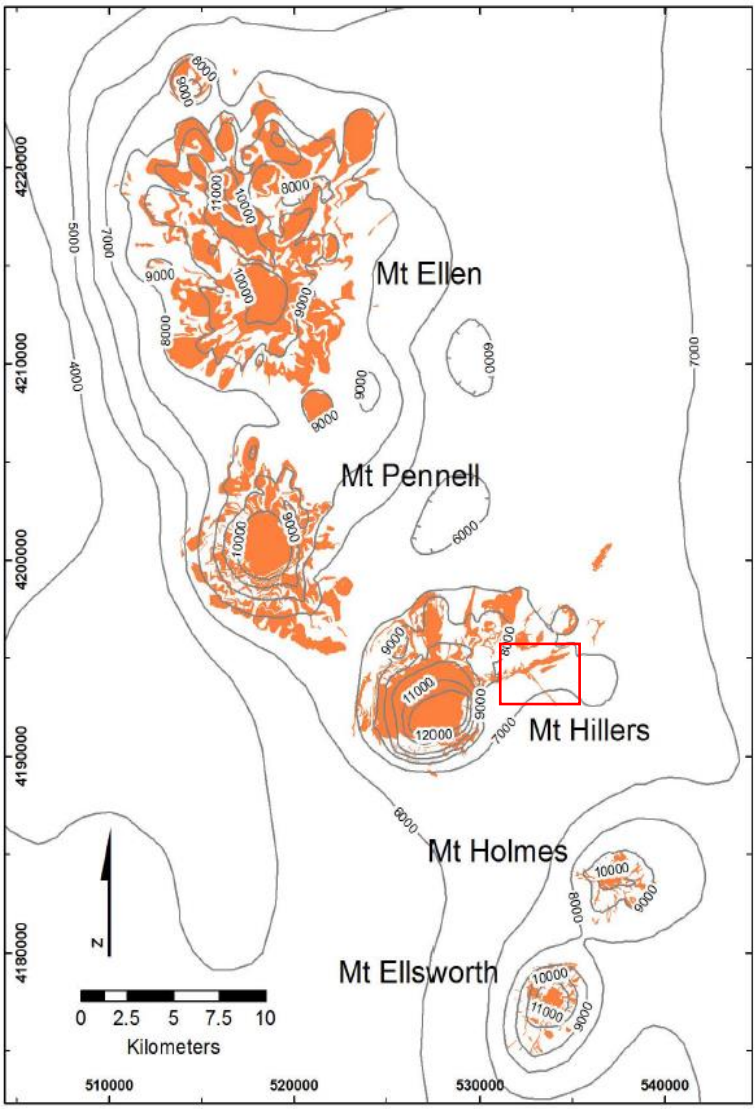

Figure 1. Structure contour map for the Henry Mountains region. Patterns show deflection of host rock from the regional W dip due to intrusive centers. 1000 foot contour interval and contours drawn for the top of the Blue Gate Shale. Igneous rock in orange. Extent of Sawtooth Ridge study area outlined in red. Inset map shows the location of the Colorado Plateau and Henry Mountains in the North American Cordillera. Modified from (Horsman et al., 2010).

Figure 2. Field photograph of the NE end of Sawtooth Ridge. Contacts between igneous intrusion (ig) and host rock (sed) are labeled. Notice the deflection of host rock and the concordant contact between intrusion and overlying host rock. Cliff is approximately 30 m tall. (Horsman et al., 2009).

2. Shallow Magmatic Processes

Volcanic activity contributes to the generation of volcanic hazards, atmospheric CO_2, and other potentially dangerous debris. Much of this activity is driven by the movement of magma in interconnected shallow sheet intrusions that comprise subvolcanic plumbing systems. It is often difficult to directly study active magma chambers and the processes behind their formation. For example, high precision geodetic measurements can record the cyclic displacement of topographic surfaces at or around volcanos which is interpreted to be the injection of magma at depth. However, this interpretation provides few constraints in terms of source/origin of magma, vertical and lateral transport of magma through the shallow crust, the influence of rheological characteristics and local/regional stress fields on emplacement, etc. To make interpretations such as these, it is useful to review mechanisms of magma transport in the upper crust.

a. Vertical Ascent of Magma

Traditional ideas of magma ascent in the shallow crust that involve low-inertia, Stokes-type flow (e.g. diapers) have largely been replaced with ideas of magma ascent through dike propagation and/or through pre-existing fractures. As magma ascends, its temperature decreases rapidly. As temperature decreases, melt viscosity increases exponentially. High melt viscosities lead to increased drag against wall rock, suggesting that rapid ascent to the shallow crust is necessary if magma is to remain fluid enough for shallow emplacement. Ascent velocities are much greater (up to six orders of magnitude) in dike conduits than in diapiric flow (Petford et al., 2000), suggesting that magma ascent in the shallow crust is more accurately represented by ascent through dikes rather than low-inertia diapirism. Petford et al. (1993) calculate critical dike widths in which magmas of a specified density and viscosity will ascend rapidly enough to avoid crystallization prior to emplacement in the shallow crust. This suggests that not only is rapid

ascent through dikes required for emplacement in the shallow crust, but that there must exist a certain dike width that allows for magma ascent without premature solidification.

b. Emplacement

In this study, *emplacement* refers to the transition from vertical ascent to lateral movement. The vertical *ascent* of magma in dike conduits is driven primarily by a density contrast between magma and wall rock, which is sustained through the decompression of rising magma. If density contrasts are also the primary mechanism driving *emplacement*, the transition from vertical to horizontal movement should be initiated at a point where no density contrast exists (i.e. a point of neutral buoyancy). However, Vignearesse and Clemens (2000) show that a point of neutral buoyancy between granitic magma and most sedimentary host rocks does not exist. Many other lines of evidence suggest this is not the dominant mechanism driving emplacement. For example, basaltic magma flows would almost never reach the Earth's surface because of their high density, but this is a common occurrence. Both field observations from Johnson and Pollard (1973) and geophysical data from Thomson and Hutton (2004) show sills intruding strata of differing densities, and even transgressive sills intruding into different horizons within one stratigraphic section. There can only be one point of neutral buoyancy for a given magma in a stratigraphic section, so, there must be other factors driving the transition from ascent to emplacement.

Stress fields and rheologic contrasts are strong factors governing emplacement in many settings. For example, hydraulic fractures initially open parallel to the least principal stress direction (Anderson, 2005). A schematic of stress relationships in an opening fracture is shown in (Fig. 3). As the radius of the fracture tip approaches zero, the theoretical stress at the fracture tip approaches infinity. This localization of stress causes instantaneous deformation, expanding

the fracture in a plane perpendicular to the minimum stress direction (Parsons et al., 1992; Anderson, 1951). For example, magma emplaced in the brittle upper crust during periods of no tectonic strain will likely experience a minimum principal stress oriented vertically, encouraging sill formation. Rigidity contrasts are another important factor governing emplacement in the Henry Mountains. Field evidence suggests that the interface between an overlying rigid layer and an underlying less-rigid layer could halt vertical dike ascent and encourage horizontal sill formation (Fridleiffson, 1977). Kavanaugh et al. (2006) tested this theory using analogue experiments. In these experiments, layers of gelatin with contrasting rigidities were injected with wax to mimic a dike ascending through heterogenous crust (Fig. 4). Their experiments show that in the absence of external stresses not only is an interface required for sill formation, but specifically an interface with a rigid layer underlain by a less-rigid layer. Subsequently, when a sill solidifies it creates another high-contrast interface favorable for further sill emplacement (Menand et al., 2011).

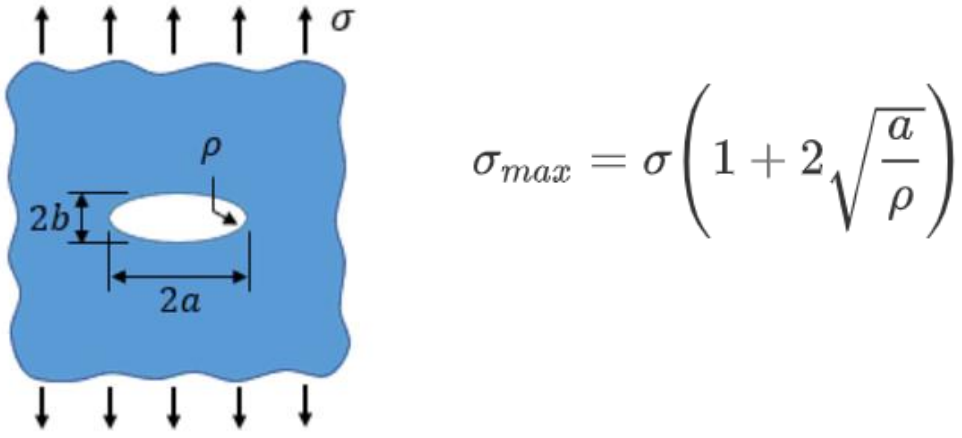

Figure 3. Schematic of a generalized fracture opening in a hypothetical stress field. σ = minimum stress direction, σ_{max} = theoretical stress value, ρ = radius of ellipse curvature, a = ½ length of fracture ellipse. (Anderson, 2005).

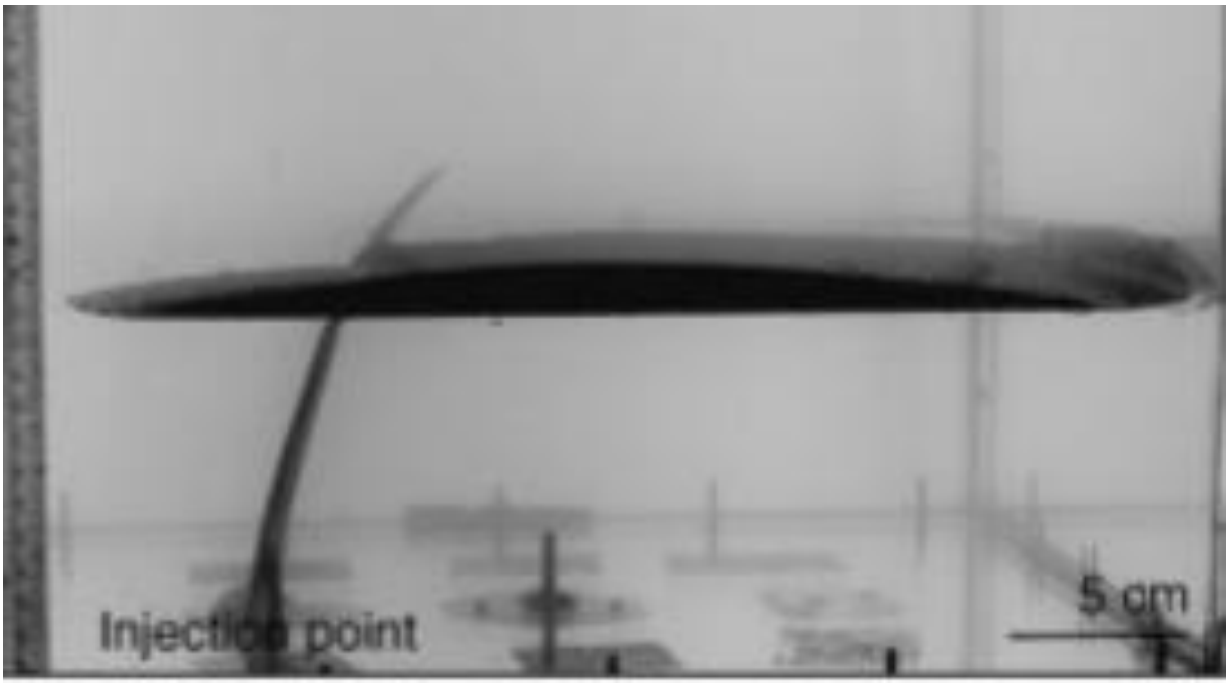

Figure 4. The emplacement of a laccolith as shown in the experiments conducted by Kavanaugh et al. (2006). Wax (dark material) as injected into layers of gelatin (clear/light material) with contrasting viscosities. (Kavanaugh et al., 2006)

3. Background

a. Geologic Setting

i. Colorado Plateau

The Colorado Plateau is a geologic province consisting of mostly sub horizontal Paleozoic through Neogene sedimentary strata and covers 350,000 km^2 in the North American Cordillera and is 45-50 km thick in most areas (Fig. 5, 6) (Hunt, 1956). Precambrian basement is overlain by (in places) several kilometers of Phanerozoic sedimentary and (minor) igneous rock. While the borders of the plateau experienced intense Cretaceous to Eocene crustal shortening, Oligocene volcanism, and Cenozoic magmatism, uplift, and extension (Nelson et al., 1992), the interior of the Colorado Plateau (i.e. the location of the Henry Mountains) was left largely unaffected and undeformed (Nelson and Davidson, 1993).

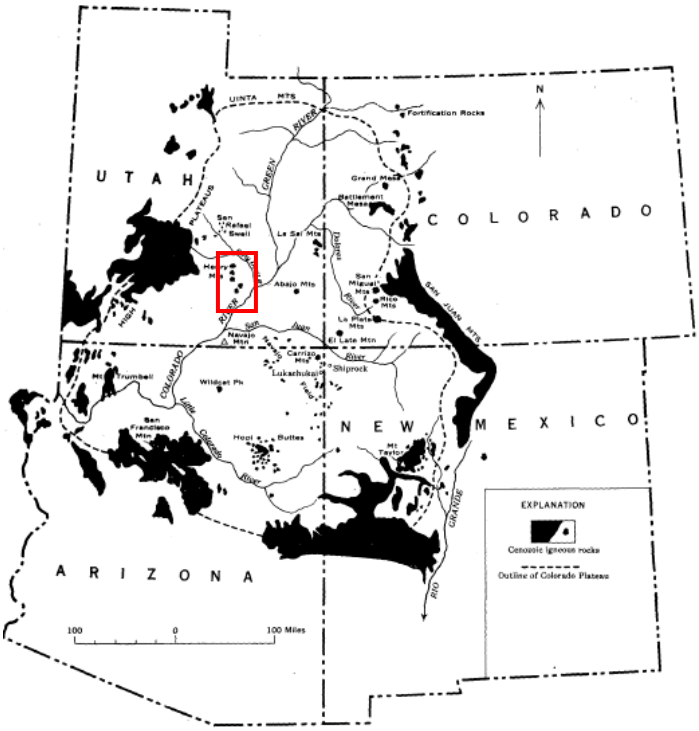

Figure 5. Map showing the extent of the Colorado Plateau province and the distribution of Cenozoic igneous rocks within it. Henry Mountains outlined in red. (Hunt, 1956).

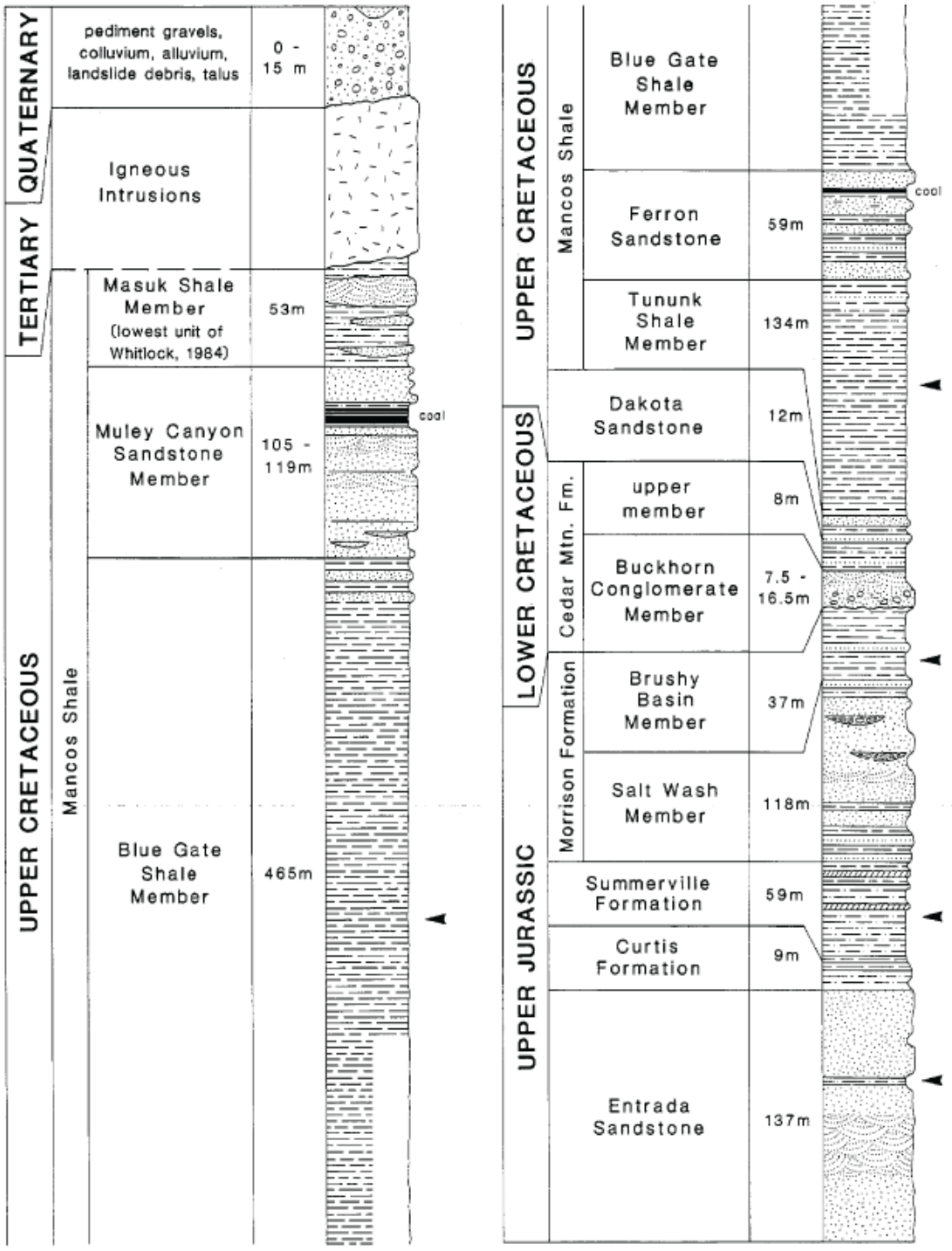

Figure 6. Stratigraphic section of the Colorado Plateau sedimentary strata as found at Mount Ellen of the Henry Mountains. Black Arrows represent strata that are preferentially intruded. The Upper Jurassic and Lower Cretaceous strata become particularly important in the Mount Hillers and Sawtooth Ridge area. (Hunt, 1956).

ii. The Henry Mountains

The Henry Mountains are a group of five Cenozoic igneous intrusive centers emplaced at 2-4 km depth into the nearly flat-laying stratigraphy of the Colorado Plateau. The first-order geometry of each center is a central laccolithic body from which smaller intrusions radiate. Emplacement of the intrusions uplifted and domed sedimentary host rock causing local bedding orientations to deviate from the regional west dipping (1-2°) orientation of Colorado Plateau strata. Magmatism originated from an east-west trending magmatic belt produced during the waning stages of the Laramide orogeny, and lasted from 32-23 Ma (Nelson et al., 1992). This postdates the minor regional deformation of the Colorado Plateau associated with Laramide activity. Along with a lack of post-magmatic tectonic deformation, this ensures that any host rock deflection is due to magmatic processes alone. Most of the exposed igneous rock in the Henry Mountains has a bulk andesite-to-trachyandesite composition and is classified texturally as a plagioclase-hornblende-porphyry (Hunt et al., 1953; Nelson et al., 1992). The matrix is composed of microcrystalline feldspar, amphibole, and oxides, and typically comprises at least 50% of total rock volume. Dominant phenocrysts include euhedral feldspar 0.2-1 cm in diameter, comprising 30-35% of total rock volume, and 0.1-0.5 cm long euhedral needles of amphibole, comprising 5-15% of total rock volume (Horsman et al., 2005).

iii. Mount Hillers and Sawtooth Ridge

The Mount Hillers intrusive center (Fig. 7a) is reportedly the best exposed and largest of the Henry Mountains intrusive centers and is composed of many laccolithic bodies (Horsman et al., 2005). The main intrusive body of Mount Hillers is a concordant and asymmetric laccolith with two different roof units and two different floor units (Fig. 7b). Collectively, the components of the Mount Hillers intrusive center have created up to~2.5 km of vertical displacement in the surrounding sedimentary host rock. Generally, displacement of host rock decreases moving radially outward from the center of each main laccolith. This displacement resulted in a dome centered around Mount Hillers with a diameter of ~15 km (Hunt 1953; Jackson and Pollard, 1988).

Several small, well-exposed intrusions are present up to 10 km from the eastern flank of Mount Hillers (Fig. 7a) (Maiden Creek sill, Black Mesa bysmalith, Trachyte Mesa laccolith, Sawtooth Ridge intrusion). Previous work has thoroughly constrained the geometries and emplacement histories of the Maiden Creek Sill, Black Mesa Bysmalith, and Trachyte Mesa Laccolith (Hunt et al., 1953; Horsman et al., 2005; Saint-Blanquat et al., 2006; Morgan et al., 2008). However, the Sawtooth Ridge intrusion has not yet been studied in as much detail as other proximal intrusions of similar size, and it remains poorly understood. The Sawtooth Ridge intrusion extends ~4 km from the eastern flank of the Mount Hillers intrusive center, and the main crest of the ridge trends ~050 (Fig. 7a). The Sawtooth Ridge Intrusion is emplaced in the Salt Wash and Brushy Basin members of the Upper Jurassic Morrison Formation, and the Upper Cretaceous Dakota and Ferron Sandstones.

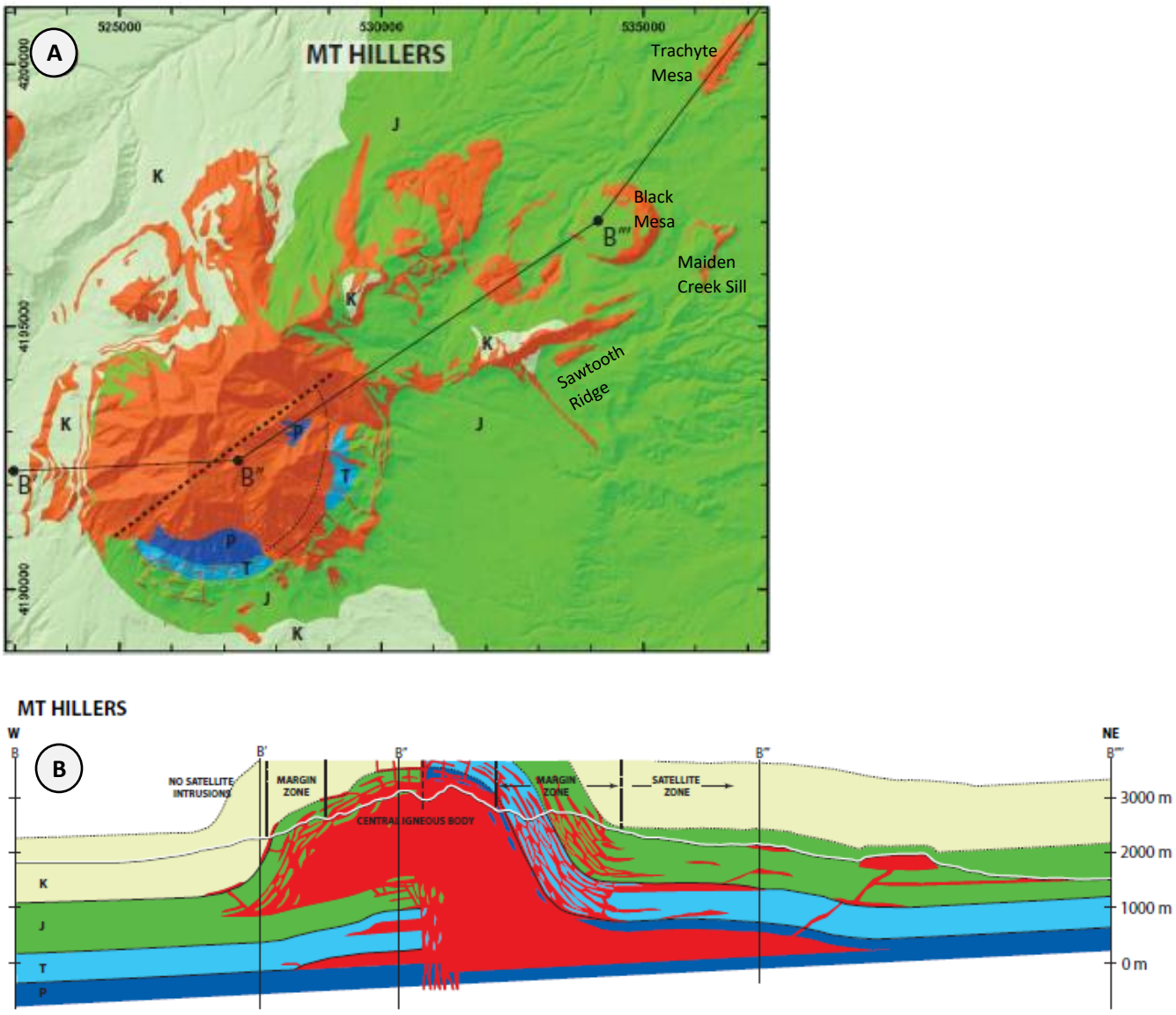

Figure 7. Geologic map and cross-section. (a) The Mount Hillers intrusive center and surrounding satellite intrusions. Igneous rocks depicted in warm colors while sedimentary host rocks depicted in cool colors. (P = Permian, T = Triassic, J = Jurassic, K = Cretaceous) Sawtooth Ridge and the proximal satellite intrusions discussed in this paper are labeled. (b) A cross section running from B-B''''. Modified from (Horsman et al., 2018).

b. Previous Work on the Henry Mountains

Recent works in the Henry Mountains provide examples of shallow intrusions that were constructed through smaller component intrusions (Figs. 8a and b) (Maiden Creek sill, Trachyte Mesa laccolith, Black Mesa bysmalith; Horsman et al., 2005; Morgan et al., 2008; Saint-Blanquat et al., 2006). Pulsed construction can lead to stepwise growth of intrusive bodies. For example, an intrusion constructed through pulses of magma may start out as a sill and, through subsequent injections of magma, may inflate to become a laccolith, and eventually a punched laccolith (Horsman et al., 2010). The geometries of these intrusions have varying characteristics, including volume of magma and interaction with host rock, and show a positive relationship between size and complexity. Their proximity and similarities in size to Sawtooth Ridge making them useful in understanding the construction of the Sawtooth Ridge intrusion. For each satellite intrusion in this section I outline its observed geometry, inferred construction history, and interaction with host rock.

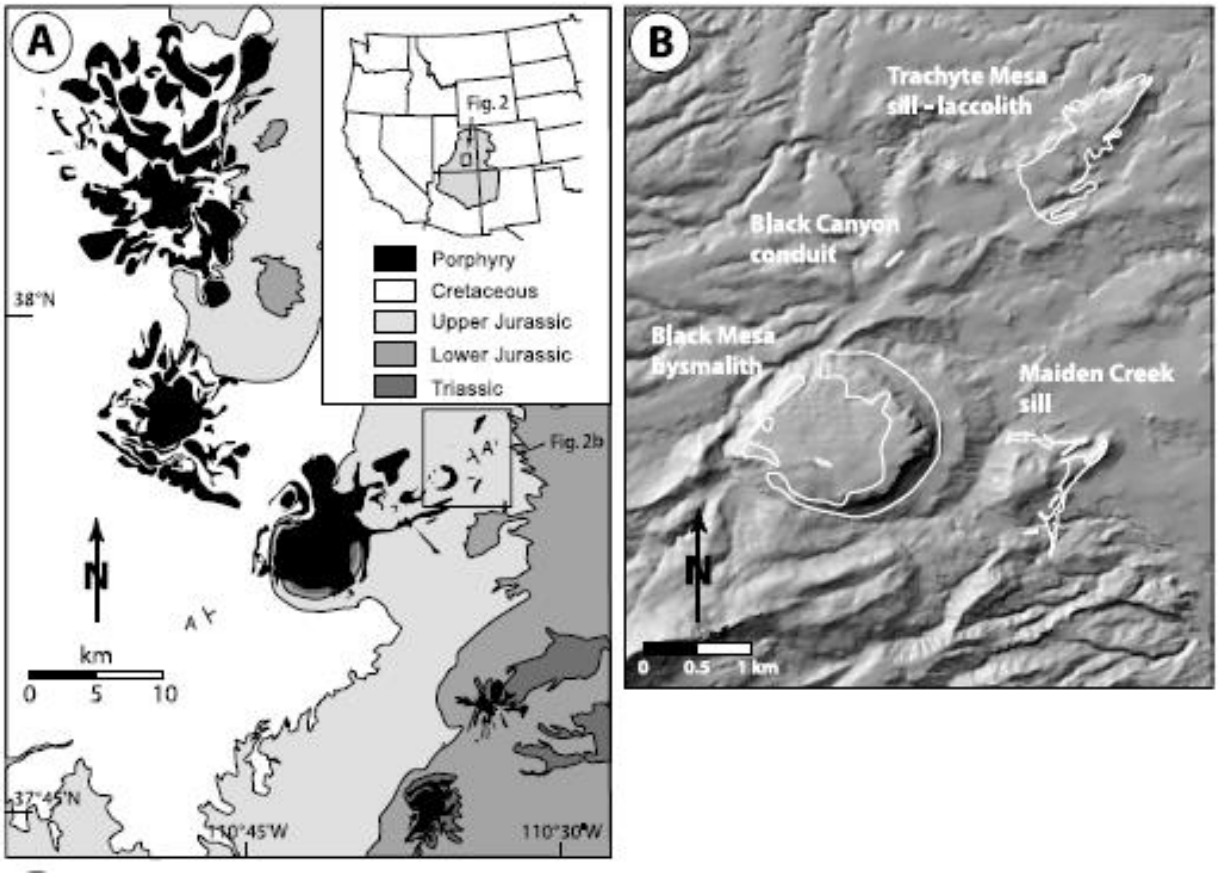

Figure 8. (a) Greyscale map of the Henry Mountains region. Igneous rock is shown in black. Inset map shows the location of the Henry Mountains Region within the Colorado Plateau. Extent of B outlined in the black square. (b) Hillshade map of small intrusions proximal to Mount Hillers and Sawtooth Ridge. Igneous exposure outlined in white. (Horsman et al., 2010).

i. Maiden Creek Sill (MCS)

Horsman et al. (2005) describe the geometry of the MCS as an elliptical main body with several finger-like lobes protruding from it in map view, and as a simple sill in cross-section (Fig. 9). The main body has concordant upper contact and a concordant base and was intruded at an estimated depth of ~3 km into the Entrada sandstone (Wilson et al., 2019). However, basal contacts beneath finger-like lobes cut upward through the stratigraphic section. Total volume of igneous rock is <0.03 km^3 and both the main body and fingers of the MCS are constructed of at least two sequentially emplaced sheets, where the extent and geometry of the second sheet is controlled by the first (Horsman et al, 2005). Many lines of evidence for pulsed construction are observed: solid-state deformation at igneous-igneous contacts (Fig. 10); presence of intercalated sedimentary rocks between the sheets; and continuous bulbous terminations observed in cross section at the margins of the intrusion. Through detailed analysis of magmatic fabric orientation, Horsman et al. (2005) found that magma likely originated from a feeder to the west and flowed from the center of the main body outward to the observed finger-like lobes (Fig. 9). The fingers of the MCS are far fewer in number than with respect to the intrusion's size than observed at other locations, and they are significantly larger relative to intrusion size than those elsewhere.

The presence of these fingers leads to two possible interpretations: 1) the main body may be a region that has coalesced into a sheet of magma behind several propagating fingers as described by Pollard et al. (1975), or, 2) the fingers may be secondary intrusions fed by the main body, rather than features driving its propagation (Horsman et al., 2005; Wilson et al., 2019).

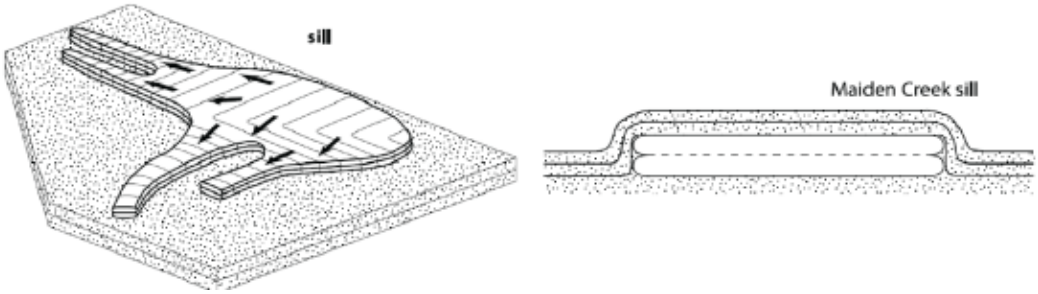

Figure 9. Schematic diagram showing the interpreted mode of construction of the Maiden Creek Sill from two different angles. Black arrows represent magma flow direction during emplacement. Speckled patterns represent sedimentary host rock. Modified from (Horsman et al., 2010).

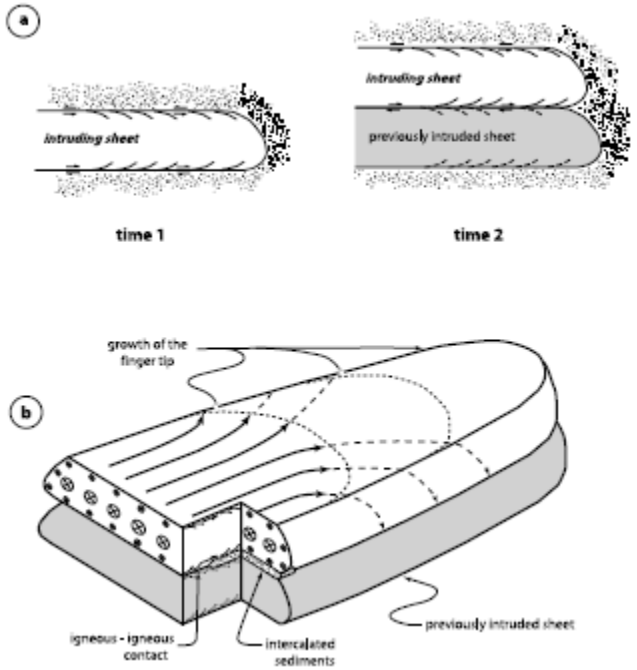

Figure 10. Schematic diagram showing the emplacement of separate sheets of igneous rock atop one another. (a) Igneous-Igneous contacts are clearly visible when time for cooling is allowed between emplacement events. (b) black arrows represent magma flow directions in a divergent flow regime and intercalated sedimentary rocks are visible in between igneous sheets (Horsman et al., 2005).

ii. Trachyte Mesa laccolith (TML)

The (TML) is a flat-topped igneous body that is 2.2 km long and 0.7 km wide (Morgan et al., 2008; Whetmore et al., 2009) (Fig. 11). Its thickness ranges from 5 m in the NE to greater than 50 m in the SW, and the long axis of the intrusion lies along a line radiating from the core of Mount Hillers ~13 km to the SW. Many igneous-sedimentary contacts are exposed along the steep sides and top of the intrusion, including much of the concordant contact (Morgan et al., 2008). Field observations suggest that current TML exposure corresponds closely to that of its original intrusive geometry, so, a rough estimate of intrusive volume can be calculated. Using the intrusion dimensions and a range of 20-40 m for an average thickness, total igneous rock volume for the TML is estimated to range from .2-.4 km^3.

Stacked, bulbous terminations of igneous rock and the presence of 2-3 cm thick shear zones along internal contacts are the most striking lines of evidence pointing to incremental assembly in the TML. The presence of sandstone lenses isolated between igneous terminations suggest either the presence of individual magma sheets, or the finger-like propagation of this intrusion's margins. Magnetic fabrics determined from anisotropy of magnetic susceptibility (AMS) correspond well with observed macroscopic hornblende orientations and are used as a proxy for magma flow direction (Morgan et al., 2008) (Fig. 12). AMS results led Morgan et al. (2008) to create a model of emplacement involving the initiation of either: 1) wide sheets emanating from a central transport channel, or, 2) finger-like sheets that emanate from a transport channel and coalesce to form wider sheets (Fig. 12).

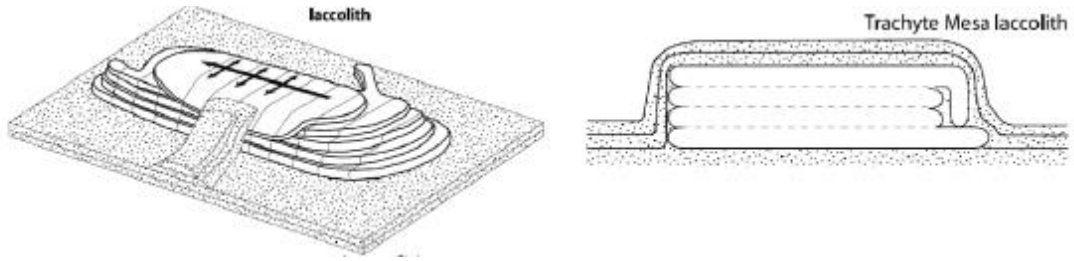

Figure 11. Schematic diagram showing the interpreted mode of construction of the Trachyte Mesa Laccolith from two different angles. Black arrows represent magma flow direction during emplacement. Speckled patterns represent sedimentary host rock. Modified from (Horsman et al., 2010).

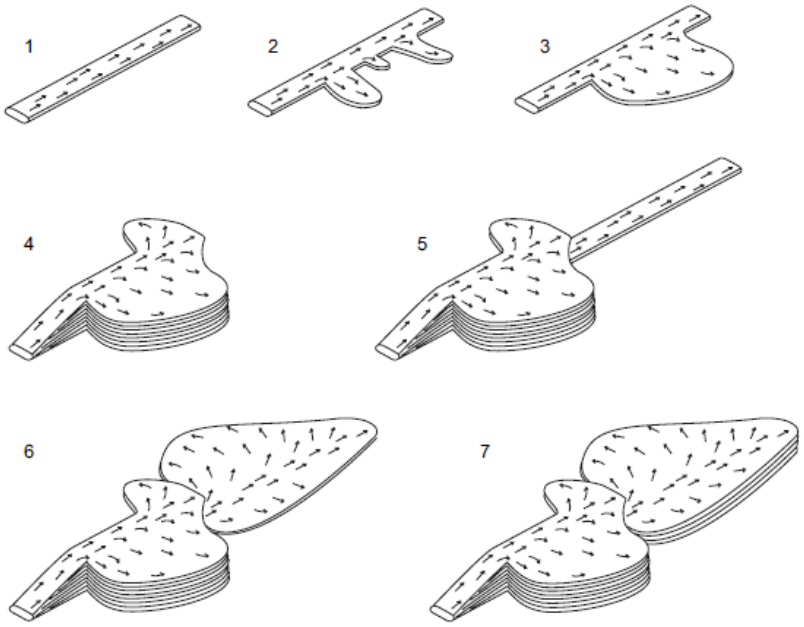

Figure 12. Schematic diagram depicting the emplacement of Trachyte Mesa Laccolith split into seven time steps. Black arrows represent magma flow direction during emplacement. Modified from (Horsman et al., 2010).

iii. Black Mesa bysmalith

Saint-Blanquat et al. (2006) describe the Black Mesa bysmalith (BMB) as a cylindrical pluton 150-250 m thick and 1.7 km in diameter (Fig. 13). The BMB is asymmetrical with thicker sequences of igneous rock in the SE., and the total volume of igneous rock is estimated to range from .3-.5 km^3. The roof of the intrusion is flat, dips slightly to the north, and is topped by concordant sedimentary strata of the Morrison Formation. The base of the intrusion in flat and concordant with the underlying Summerville formation. The BMB was fed by a vertical dike near its SE end. Many lines of evidence point to a history of pulsed construction including: internal sub horizontal contacts marked by a sharp variation in diorite texture, heterogeneous magnetic susceptibility vertical profile, and a weak petrographic zonation.

On the thinner NW side of the BMB, igneous rock was accommodated through the bending, rotation, and faulting of Morrison formation without a loss of continuity. However, on the thicker SE side of the BMB, igneous rock was accommodated through faulting of Morrison formation strata as the roof of the intrusion lifted upwards, causing a clear discontinuity in host rocks. Saint-Blanquat et al (2006) provide the following model of emplacement: 1) sill intrusion and growth initiated growth by lateral propagation (sill stage), 2) lateral growth ceases and transitions to vertical inflation through the bending of overburden once a critical length/thickness ratio is achieved (sheeted growth stage), and 3) the fracturing of wall rocks allows for the roof of the BMB to punch, or lift sedimentary strata up with it (fault-assisted growth stage) (Fig. 14).

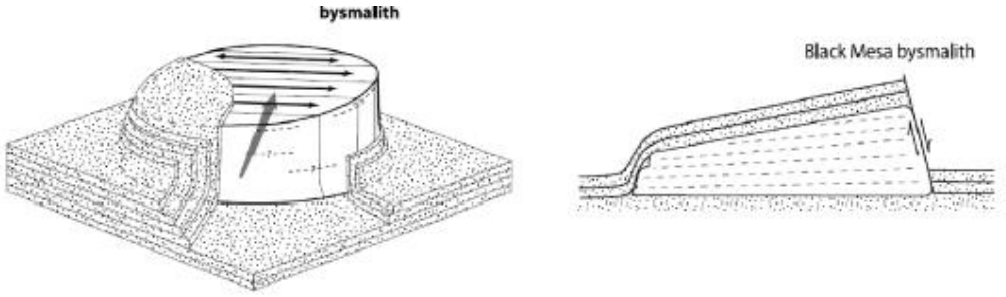

Figure 13. Schematic diagram of the assembly of Black Mesa Bysmalith from two different angles. Black arrows represent magma flow directions during emplacement and speckled layers represent sedimentary host rock. Modified from (Horsman et al., 2010).

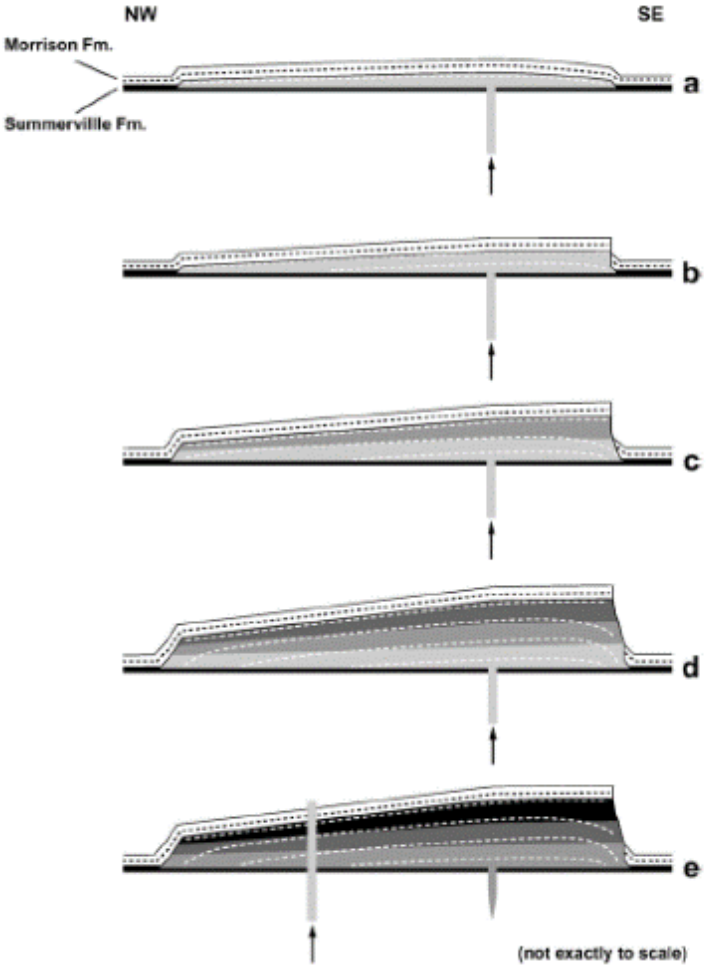

Figure 14. Schematic diagram depicting the growth of the Black Mesa Bysmalith in five time steps. (a) the BMB grows through lateral propagation. (b) The BMB grows through vertical inflation. (c) Vertical inflation continues. Notice the bending of overburden on the NW end and the faulting of overburden on the SE end. (d) Vertical inflation continues. (e) The BMB has become a punched laccolith. (Saint-Blanquat et al., 2006).

d. Previous Work on Sawtooth Ridge

i. Gilbert (1877)

Gilbert (1877) describes the Sawtooth Ridge intrusion (which he named the 'Jerry Butte') as 'the most conspicuous adjunct to Mount Hillers.' While it is topographically striking, its structure is unclear. Gilbert interprets the intrusion as the crest of a great dike that is several hundred feet wide and two miles long. The central-western portion of the dike is higher and forms the peak of the butte. Radiating from this point are three dikes of notable size. The lower Cretaceous strata sheltered between these dikes have been preserved from erosion and are lifted minimally above their original positions. The inclination of beds around the Jerry Butte are so complicated by the dips of the nearby Pulpit, Steward, and Hillers arches that no interpretations regarding the form of the butte could be made (Fig. 15).

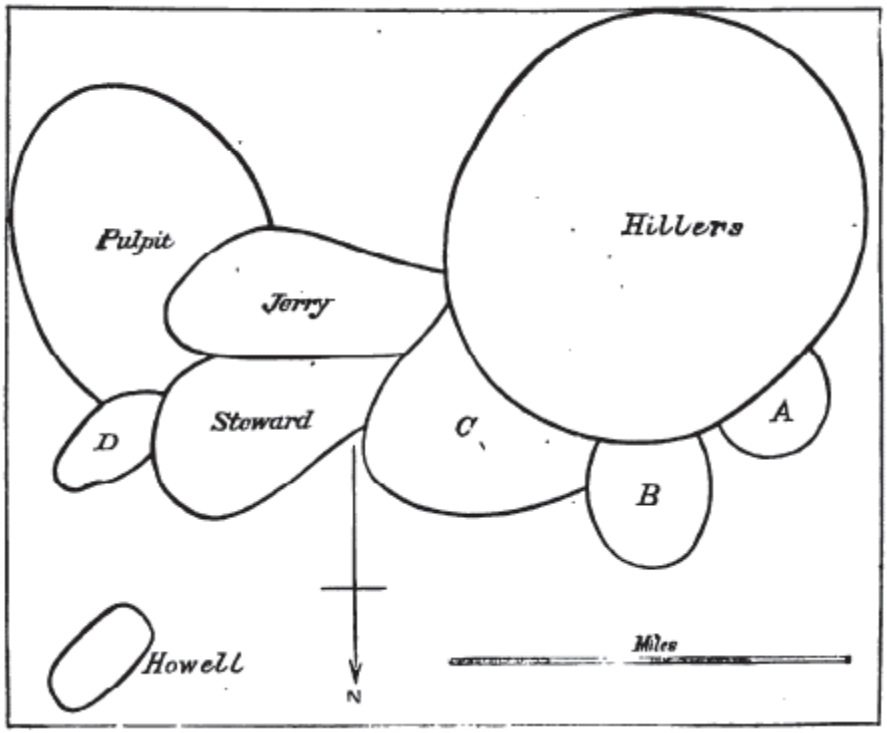

Figure 15. Sketch drawn by Gilbert (1877) depicting the various igneous exposures of the Mount Hillers intrusive center. 'Jerry' butte is equivalent to Sawtooth Ridge. North arrow is oriented toward the bottom of sketch.

ii. Hunt et al. (1953)

Hunt et al. (1953) describe the Sawtooth Ridge intrusion as an extremely rough and jagged exposure of porphyry with an irregular upper contact. Its top consists of several porphyry ridges with sedimentary host rock preserved between them (Fig. 16). The central part of the intrusion bulges discordantly upward with Ferron sandstone capping its peak. An exposure along the intrusion's NE end cuts discordantly upward through the Morrison formation, sending small sills into it (Fig. 17). The roof of this exposure is concordant with overlying Morrison strata, and Morrison formation dips 4°W. The SW end of the Sawtooth Ridge intrusion consists of parallel porphyry ridges with Morrison formation strata in a trough between them. The strata dip 30° from the ridges into the trough, which deepens eastward. Sills and dikes extend laterally from the sides of the intrusion at right angles (Fig. 16). Hunt et al. (1953) describe these as notable exceptions to the general rule that Henry Mountain intrusive structures radiate from their central stocks.

Hunt et al. (1953) provide two interpretations regarding the geometry of the Sawtooth Ridge intrusion: 1) the exposed porphyry may be the bulging upper part of a discordant dike, or, 2) the porphyry may be a sub horizontal cylindrical body trending roughly NE and extending to no great depth.

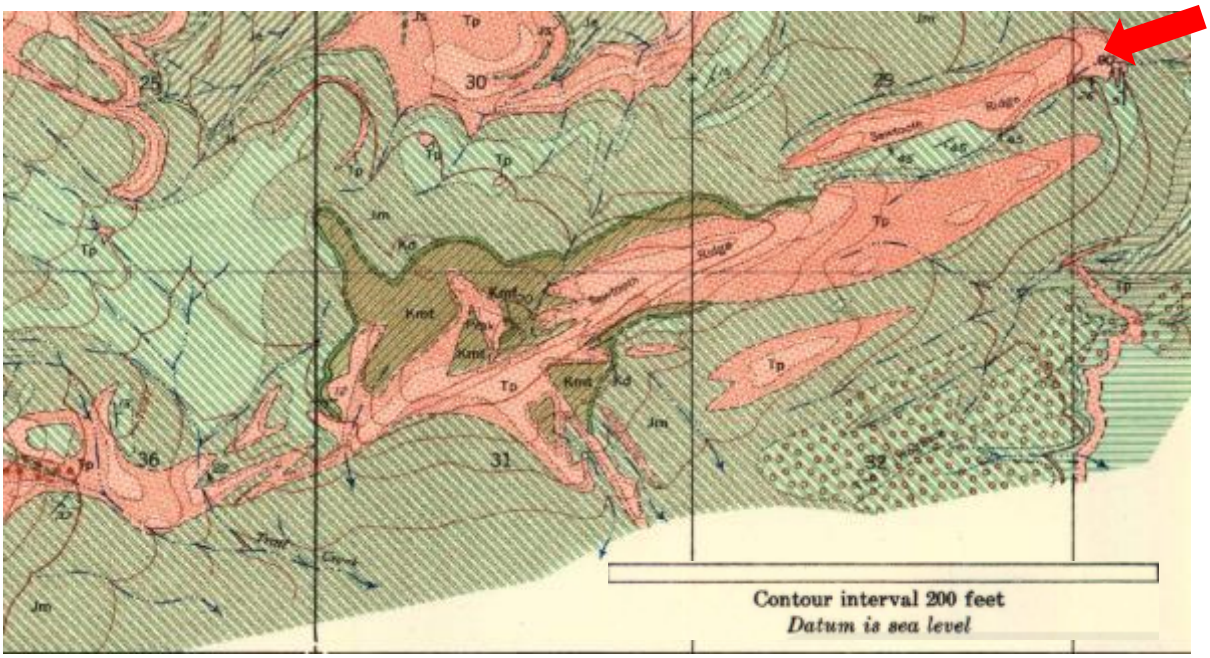

Figure 16. Geologic map of Sawtooth Ridge created by Hunt et al. (1953). Green colors represent sedimentary host rock while pink represents igneous rock. Red arrow represents the location of the outcrop shown in Figure 17.

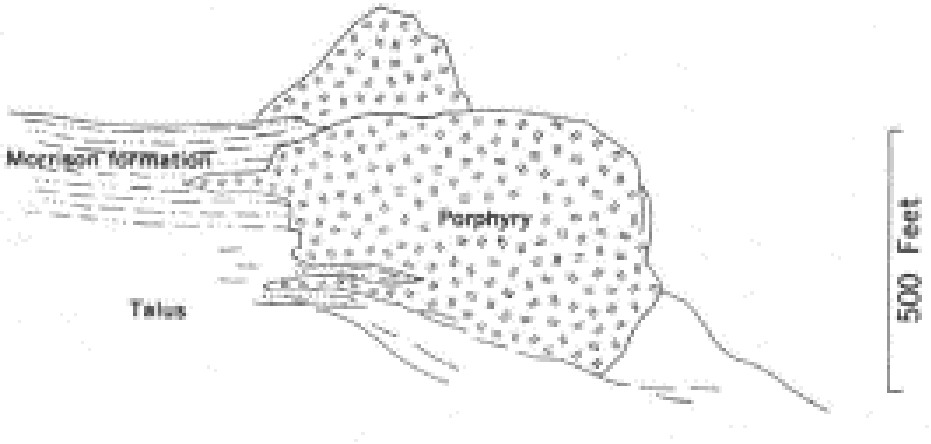

Figure 17. Gilbert's Sketch of the NE end of the Sawtooth Ridge intrusion indicated by the blue arrow in Figure 16. (Hunt et al., 1953).

iii. Murdoch, Unpublished Mapping

L. Murdoch of Clemson University conducted structural mapping of the Sawtooth Ridge intrusion in the 1970's (Fig. 18). This is the most recent and detailed work on Sawtooth Ridge and was, unfortunately, never published. Murdoch was able to identify three different textures of igneous rock amongst the exposures and assigned relative timings of emplacement to each. Murdoch was also able to produce three interpretive cross-sections perpendicular to the crest of the ridge (Fig. 19). Murdoch interpreted the Sawtooth Ridge intrusion as a series of parallel dikes.

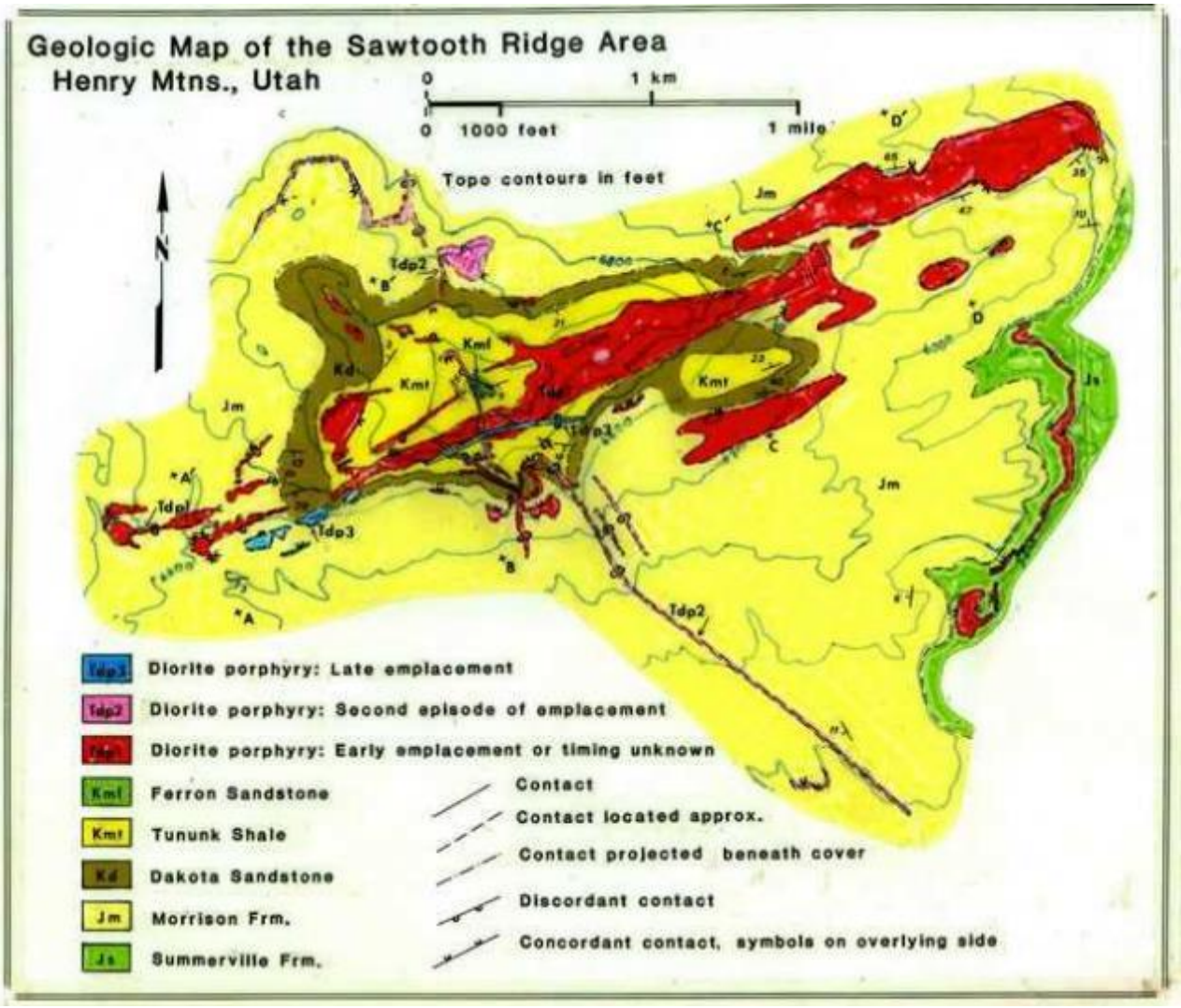

Figure 18. Unpublished geologic map of Sawtooth Ridge created by L. Murdoch of Clemson University.

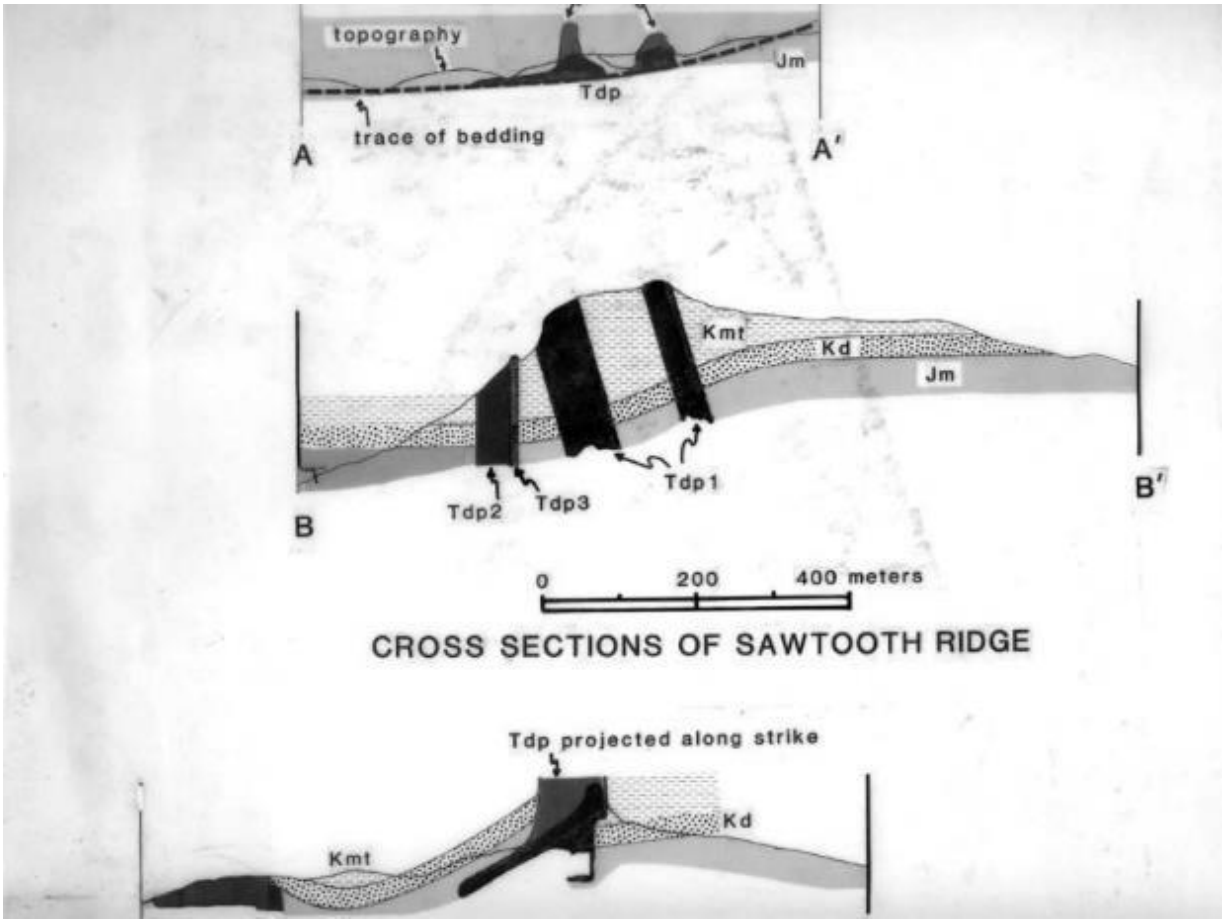

Figure 19. Unpublished cross-sections through Sawtooth Ridge created by L. Murdoch of Clemson University. Locations of these cross-sections are shown in Figure 18.

4. Methods

I have proposed two hypotheses concerning the Sawtooth Ridge intrusion: (1) the intrusion has a complex geometry, and (2) Sawtooth Ridge was constructed through two or more intrusions/injections. To test these hypotheses, I used a combination of field observations, Major- and trace- element, geochemistry, anisotropy of magnetic susceptibility, image analysis of shape preferred orientation, and magnetic anomaly modelling.

a. Field Measurements

Previous works concerning the geometry of the Sawtooth Ridge intrusion are inconclusive (Gilbert, 1877 and Hunt et al., 1953), and the most comprehensive map to date (L. Murdoch, unpublished mapping) lacks detail necessary to make concrete interpretations. In this study, field observations were combined with some of these previous works to create a detailed geologic map of the Sawtooth Ridge intrusion. This map was initially created in the field and later digitized using ArcMap. Two cross-sections through the intrusion were created to aid in showing geometric interpretations.

Field work also included the collection of oriented samples, observation of igneous rock characteristics, measurement of foliation and lineation in igneous rock fabric (Fig. 20), bedding of sedimentary host rock, and the nature of igneous-sedimentary contacts (i.e. degree of concordance, curvature vs. linearity, sharp vs. gradational).

Initially, the intrusion appears to have (at least) two components: a main ridge crest trending generally NE-SW, and a set of smaller features trending orthogonally (NW-SE) from the main crest.

Figure 20. Collection of field fabrics using a Brunton compass. Tanner Eischen is shown for scale.

b. Geochemistry

Whole-rock major and trace element compositions of 12 samples were analyzed (including duplicates) commercially by Bureau Veritas Commodities Canada Ltd. using inductively coupled plasma-mass spectrometry (ICP-MS) Drill cores (the same cores used during AMS analysis) from the interior of each sample were used for analysis to ensure freshness and minimize any effects weathering may have on chemical compositions. Samples were selected to cover a broad spatial distribution while including both the main ridge crest and its smaller, perpendicular features.

c. Fabric Analysis

i. Interpreting Magmatic Fabric Patterns

The term ‘fabric’ is used here to describe a preferred geometric arrangement of mineral grains. The formation of magmatic fabrics involves the rotation of crystals in a melt. Many fabric analysis techniques allow for the quantification of fabric orientations and are often used as a proxy for magma flow direction (e.g. Magee et al., 2016).Tectonic and regional stresses can alter or overprint earlier-formed magmatic fabrics making their interpretation difficult (Paterson et al., 1988; Saint-Blanquat et al., 2011). However, no tectonic or regional stresses have influenced the Henry Mountains porphyry during or after emplacement ensuring that fabrics are a result of magmatic processes (Horsman et al., 2005; Saint-Blanquat et al., 2006).

There are many ways to interpret fabric patterns and this must be done with caution. Before displacement pathways can be interpreted, there must be constraints on flow, strain, and particle behavior. For example, under low strain conditions a particle with a large aspect ratio (e.g. hornblende phenocryst) will rotate toward the flow direction much faster than a particle with a small aspect ratio (e.g. feldspar phenocryst). Thus, a high aspect ratio particle will tend to

align parallel with flow direction while a low aspect ratio particle will be less likely to align. However, these relationships become more complicated when considering populations of crystals, each with slightly different shapes, and especially at relatively high strain magnitudes (Patterson et al., 1998).

Flow dynamics must also be constrained to make meaningful interpretations. In convergent flow regimes where wide magma pathways become constricted and the maximum direction of extension is parallel to flow direction, crystals tend to align parallel to flow direction (Fig. 21a). In divergent flow regimes where channelized magma flows into a broader area and velocity decreases, both the direction of maximum extension and crystal alignment are perpendicular to flow directions (Fig. 21b). While crystals near wall-rock margins will experience drag forces and often align parallel to intrusion margins, the *in-situ* expansion of a magma chamber may produce fabrics at high angles (or even perpendicular) to intrusion margins.

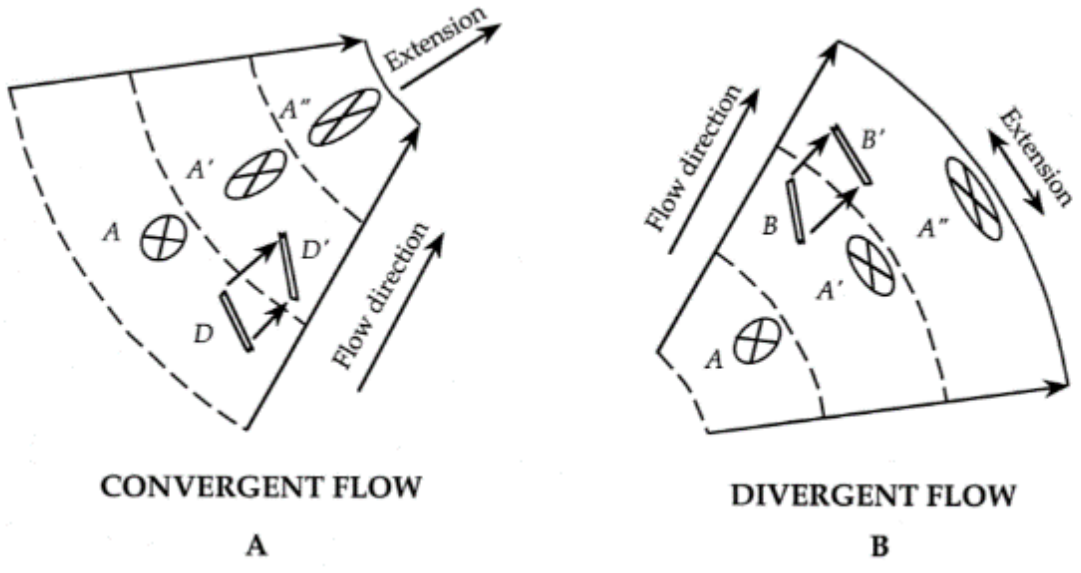

Figure 21. (a) Schematic showing the behavior of particles in a convergent flow regime. (b) Schematic showing the behavior of particles in a divergent flow regime.

ii. Anisotropy of Magnetic Susceptibility (AMS)

In many localities including the Henry Mountains, field fabrics are often absent or difficult to measure due to lack of quality exposure, etc. To circumvent this and obtain a more complete representation of igneous fabric, low-field anisotropy of magnetic susceptibility can be measured (e.g. Knight and Walker, 1988). Previous studies in the Henry Mountains have used AMS to quantify rock fabric and infer magma flow directions in intrusions similar to Sawtooth Ridge (Horsman et al., 2005; Saint-Blanquat et al., 2006; Morgan et al., 2008; Maurer, 2015). While this technique is particularly useful in igneous rocks where fabrics are weakly developed, it is important to remember that results are influenced by many factors including minerals controlling the magnetic signal and the possibility of composite fabrics (Rochette et al., 1992). The magnetic mineralogy of the Sawtooth Ridge intrusion rocks was not investigated for this study. However, previous studies of igneous rocks throughout the Henry Mountains suggest that the magnetic susceptibility signal is controlled primarily by pseudo-single domain and multi-domain titanomagnetite (Horsman et al., 2005 and Maurer, 2015). This allows for relatively straightforward interpretation of magnetic fabric (e.g. Ferre, 2003).

When collecting AMS data, a specimen of igneous rock is placed in a carefully controlled magnetic field, commonly referred to as the inducing field. The minerals in the rock become magnetized according to their susceptibility, interacting with and causing perturbations in the induced field (Rochette et al., 1992) (Fig. 22). The relationship between the original inducing field and the induced resultant field is described with a unitless tensor quantity known as magnetic susceptibility (K). The spatial distribution, shape, and preferential alignment of mineral grains (especially ferromagnetic grains) are the primary factors controlling magnetic susceptibility anisotropy of rocks. Data are visualized as an ellipsoid with three principal axes

referred to as K_1 (long), K_2 (intermediate), and K_3 (short) (Fig. 23). The magnitudes of the three axes can be used to calculate several scalar parameters:

1) K_m, the mean susceptibility, is a measure of the magnetic susceptibility in the sample and is defined as $K_m = (K_1 + K_2 + K_3)/3$.

(2) T, the mean shape factor, quantifies the degree of ellipticity with respect to a sphere: T = 0 represents a perfect sphere, T = -1 represents an infinitely prolate ellipsoid, and T = 1 represents an infinitely oblate ellipsoid. This parameter is defined as $T = (2 \ln[K_2/K_3]/\ln[K_1/K_3]) -1$. (3) P', the mean degree of anisotropy, represents the intensity of the AMS ellipsoid and is defined as $P' = \exp(^2[(n_1 - n_b)^2 + (n_2 - n_b)^2 + (n_3 - n_b)^2]^{1/2}$ where $n_i = \ln(k_i)$ and $n_b = \ln(n_1 * n_2 * n_3)^{1/3}$.

(4) L, magnetic lineation, represents the ratio between long and intermediate axes and is defined as $L = K_1/K_2$.

(5) F, magnetic foliation, represents the ratio between intermediate and short axes and is defined as $F = K_2/K_3$.

Low-field AMS analysis was conducted on 27 oriented hand samples from the Sawtooth Ridge intrusion. From each sample, 25-mm-diameter cores were drilled and oriented in the laboratory. Oriented cores were cut into 22-mm-long specimens to produce 4 to 6 specimens from each sample. The AMS of the specimens was measured using an AGICO MFK1-A Kappabridge at East Carolina University. The SAFYR and AniSoft software supplied by AGICO were used to collect and visualize the data.

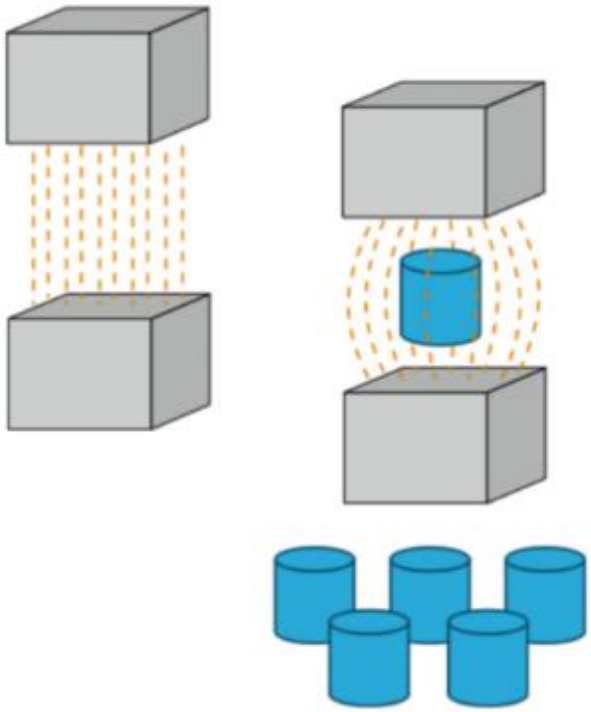

Figure 22. Graphic showing the perturbations in an induced magnetic field when a specimen is placed into an inducing field. (Horsman, Personal communication).

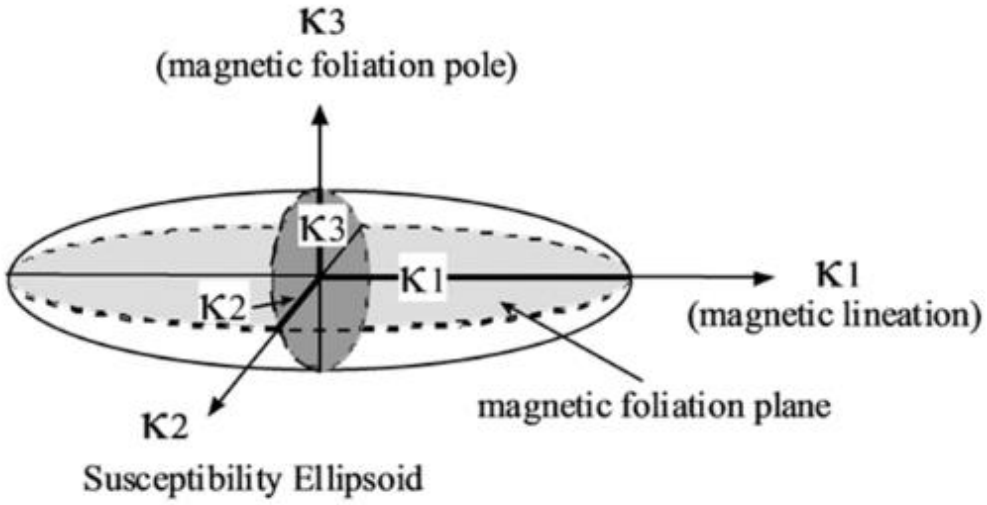

Figure 23. Example of 3d fabric ellipsoid produced from AMS.

iii. Shape Preferred Orientation (SPO)

Shape preferred orientation analysis provides another quantitative measure of rock fabric by measuring the preferred mean elongation direction of crystals (Laueneau et al., 1990; Laueneau and Cruden, 1998). Phenocrysts suspended in a viscous, cooling melt can record the last moment of strain created by the flowing magma (Patterson et al., 1998). Thus, they can be an indicator of magma flow directions in a crystallizing magma.

12 oriented samples from the Sawtooth Ridge intrusion were cut using a rock saw to have three planar surfaces in mutually perpendicular orientations. The orientations of these surfaces were measured with a Brunton compass after cutting. Each planar surface was then digitally scanned and uploaded to the Intercept2003 program (Fig. 24a) (Laueneau and Robin, 2005). Using the grey scale threshold filter, each image was manipulated into a two-color binary image to isolate the desired phenocrysts (Fig. 24b). Because the knowledge that in low strain environments high aspect ratio crystals will more easily align with magma flow direction than high aspect ratio crystals, the orientations of hornblende (rather than feldspar) phenocrysts were analyzed for this study. The image is then divided into a specified number of overlapping bins, each of which provides the boundaries for a separate calculation of phenocryst orientation. The overlapping nature of these bins limits error caused by an uneven distribution of mineral grains, etc. (Fig. 24c). Using the intercept method, a two-dimensional shape fabric ellipse was calculated. The intercept method involves a clipped image along which run sets of parallel lines with a spacing of 1 pixel between each (Fig. 24d). The number of intercepts between isolated hornblende crystals and parallel lines are counted in each possible orientation, and direction with the least counts corresponds to the elongation direction of the mineral phase in question (Laueneau et al., 2010). This technique counts only phase boundaries, so, it is most successful

when the mineral phase in question is abundant yet highly dispersed, as is hornblende in the Sawtooth Ridge intrusion porphyry.

Three-dimensional ellipsoids were computed mathematically using the program Ellipsoid2003 in which 2-d ellipse data (Fig. 24e) from each of the three mutually perpendicular rock faces are combined. This three-dimensional ellipsoid (Fig. 24f) includes the orientation and length of the three principal axes (K_1, K_2, and K_3). Just as with AMS analysis, the scalar parameters T (shape factor) and P' (degree of anisotropy) can be calculated.

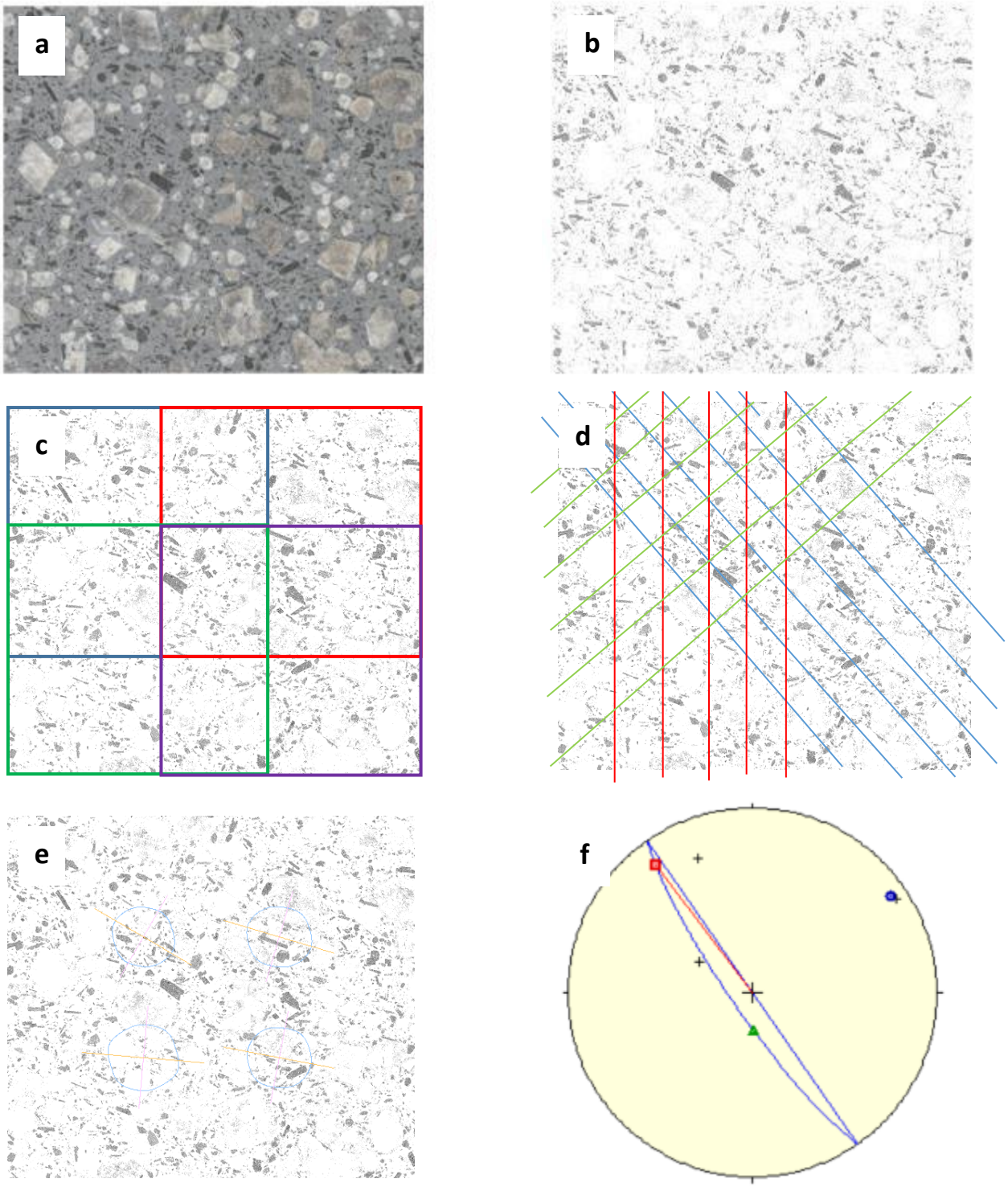

Figure 24. Graphic representation of the SPO procedure. (a) Rock face is scanned to create a digital image. (b) A grey level filter is applied to isolate desired phenocrysts. (c) Digital image is divided into specified number of overlapping bins to mitigate error due to heterogenous phenocryst distribution. (d) The intercept calculation is applied to the digital image using sets of parallel lines. Different colors of lines represent separate intercept calculations conducted at different orientations. (e) a 2d ellipse is calculated for each of the overlapping bins. (f) After a 2d ellipse from ach of three rock faces is combined into a 3d ellipsoid, a lower hemisphere equal area projection depicting the orientations of the ellipsoid's principal axes is produced. Red square = major axis orientation, blue circle= intermediate axis orientation, green triangle = minor axis orientation, blue line = plane of foliation

e. Magnetic Anomaly Modelling

Local variations in Earth's magnetic field are referred to as magnetic anomalies and are caused by the interaction between subsurface features and the ambient magnetic field at Earth's surface. Anomalies can be measured with a magnetometer and used to make interpretations about shallow subsurface features. However, the magnitude and nature of an anomaly is affected by a subsurface feature's magnitude of magnetic susceptibility, shape, and proximity to the location of measurement. Different combinations of susceptibility, shape, and proximity can produce similar variations in Earth's magnetic field, complicating interpretations. Fortunately, if constraints are placed on magnetic susceptibilities and the proximity of features to the surface, varying subsurface geometries can be associated with magnetic anomaly profiles (Fig. 25) allowing for simple interpretations of subsurface intrusion geometry. Using a Geometrics G858 magnetometer, bulk magnetic susceptibility was measured along two transects perpendicular to the main crest of the Sawtooth Ridge intrusion (Fig. 26). An additional profile was collected across a dike to test this method on a simple intrusion geometry. Magnetic anomaly and GPS data were filtered and smoothed using the Geometrics MagMap and MagPick software. To test possible intrusion geometries, magnetic anomaly data were forward modelled using the GM-SYS and Oasis Montaj software.

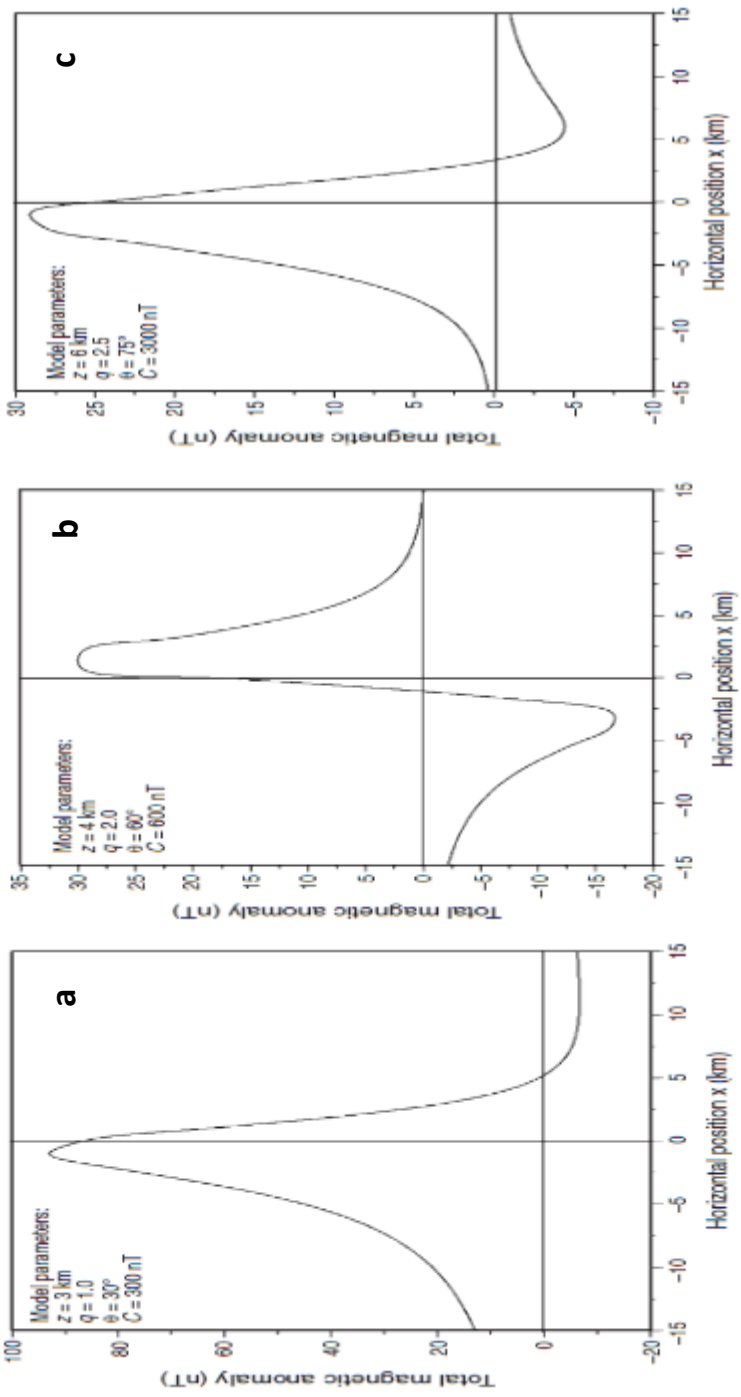

Figure 25. Simplified plot showing total magnetic anomaly curve produced by different anomaly geometries (a) a thin sheet (b) a horizontal cylinder (c) a sphere. (Abdelrahman et al., 2012)

5. Results

a. Field Measurements

Field measurements and observations were used to construct a detailed map of the Sawtooth Ridge intrusion (Fig. 26). The geologic map covers a region approximately 15.5 km^2 in area and the crest of Sawtooth Ridge is approximately 4.6 km long. At first glance, the first-order geometry of the intrusion appears to be a pipe or tube. However, the second order geometry of the intrusion is more complex; lenses of sedimentary host rock are isolated between lobes of igneous rock; relatively small igneous features extend perpendicularly from the main crest of the ridge (e.g. a 2.5 km long dike extending from the SE side of the intrusion); and sedimentary-igneous contacts are complex (Fig. 26). For example, both concordant and discordant contacts are present across the intrusion, and some even change in nature (e.g. from concordant to discordant) along their length. These contacts are almost exclusively sharp and straight, with little evidence of gradational contacts. The upper surface of the intrusion has a highly variable topography peaking in the center of the ridge near the outcrop of Ferron sandstone. There are no obvious outcroppings of the intrusion's bottom contact. Based on field observations and the results of other analytical techniques, cross sections were constructed through the intrusion and surrounding host rocks (location shown in Figure 27).

Bedding measurements (Fig. 28) show that sedimentary host rocks generally dip away from the main intrusive feature and are increasingly domed upward with proximity. However, not all bedding measurements follow this trend, particularly in areas where sedimentary host rocks are isolated between lobes of igneous intrusion.

Observed field fabrics are defined primarily by the alignment of hornblende phenocrysts and are dominantly linear in shape. The majority of measured fabrics are magmatic in origin.

Magmatic fabric orientations vary depending on location (Fig. 29) but are generally found near the center of intrusive features. Exposures on the SW edge of the intrusion have moderate to steeply plunging fabric orientations trending towards the Mount. Hillers intrusive center, while orientations along the main crest are dominantly sub horizontal and trend parallel (NE/SW) to the intrusion. Solid state fabrics were scarce but may be present in locations where the measurement was taken at or near the intrusion margins and resulted in an orientation perpendicular to main intrusion (NW/SE). For example, at the peak of Sawtooth Ridge, there are linear fabrics trending to the NW/SE with sub horizontal plunges.

While much more difficult to make in the field, textural observations were made both in at the outcrop scale and in the lab using hand samples. At the outcrop scale, no textural contacts or cross-cutting relationships are visible, and textures are difficult to distinguish. However, some notable differences were observed such as a more blue-grey colored matrix in outcrops near the SW end of the intrusion, and an increased hornblende abundance at the NE end. At the hand-sample scale, porphyry samples were later classified into three textural groupings based on general observations of matrix color, phenocryst type, size, and abundance, presence of xenoliths, and type of weathering. The spatial distribution of these groupings is plotted atop bedrock geology in Figure 30a.

Samples classified as Texture 1 plot atop the parallel dike-like features at the intrusion's SW end and along the most NE ridge. Textually they are approximately 40-50% phenocrysts with plagioclase crystals up to 8 mm, hornblende crystals to 4 mm, and a medium grey matrix. Xenoliths are present (1-2 cm) along with small (1-2 mm) quartz pockets in some samples (Fig. 30b).

Samples classified as Texture 2 plot near the peak of Sawtooth Ridge and along the NE end of the main ridge. They are approximately 35-45% phenocrysts with plagioclase crystals up to 6 mm, hornblende crystals up to 3 mm, and a light-pale grey matrix. These samples display heavy oxidation on their weathered faces, and plagioclase crystals display oxidative alteration (Fig. 30c).

Samples classified as Texture 3 plot primarily atop features extending perpendicular from the main ridge crest. Texturally they are 40-50% phenocrysts with plagioclase crystals up to 7 mm, hornblende crystals up to 3 mm, and a dark grey matrix. Many of the phenocrysts in these samples seem to have poorly defined, gradational crystal boundaries with adjacent matrix, in contrast to the crisp, well-defined boundaries seen in textural groups one and two (Fig. 30d).

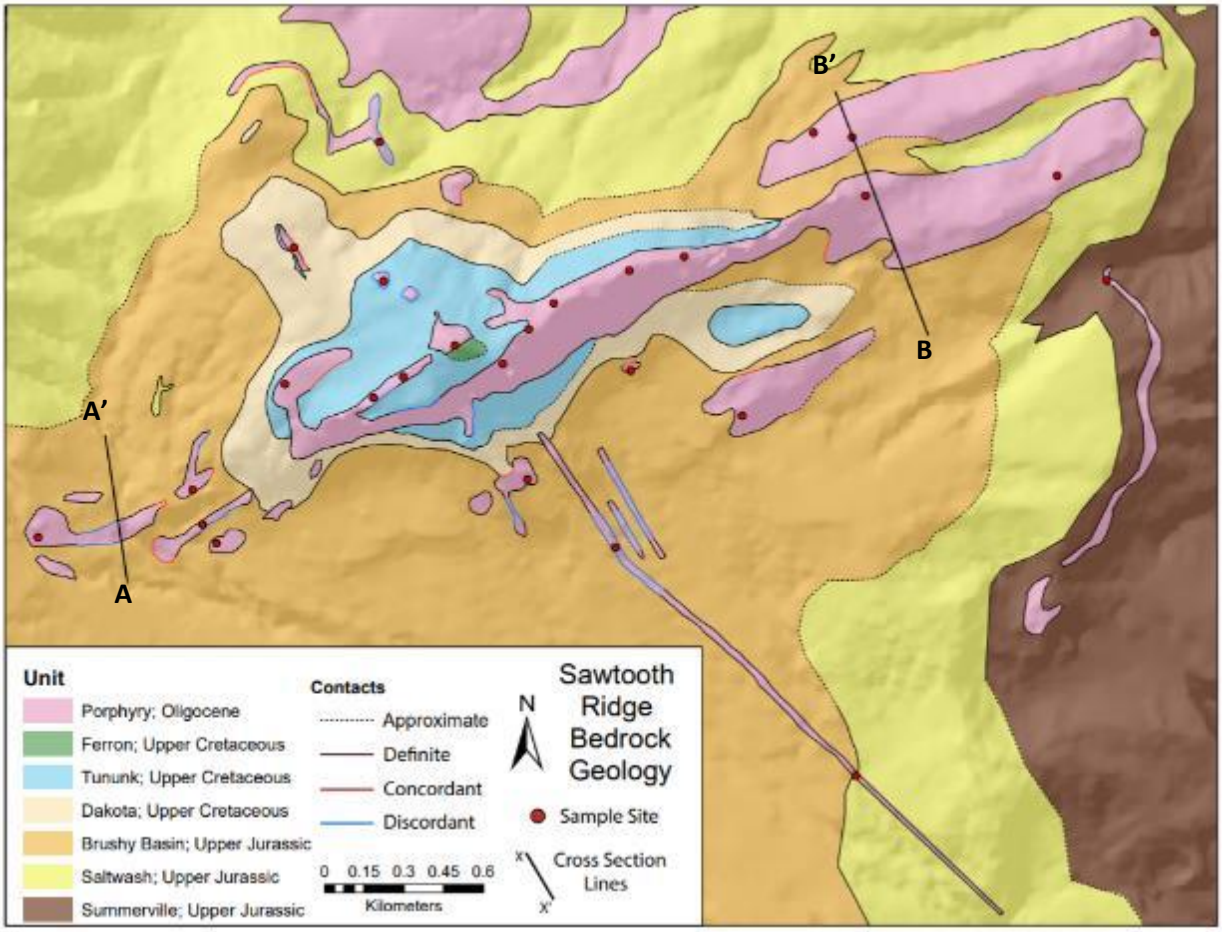

Figure 26. Sawtooth Ridge bedrock geology. Porphyry is shown in pink, sedimentary host rocks shown in all other colors. Sample sites (i.e. where an oriented sample was collected for later analysis) are shown as red dots. (NAD 1927 Zone 12N, Henry Mountains, southern Utah).

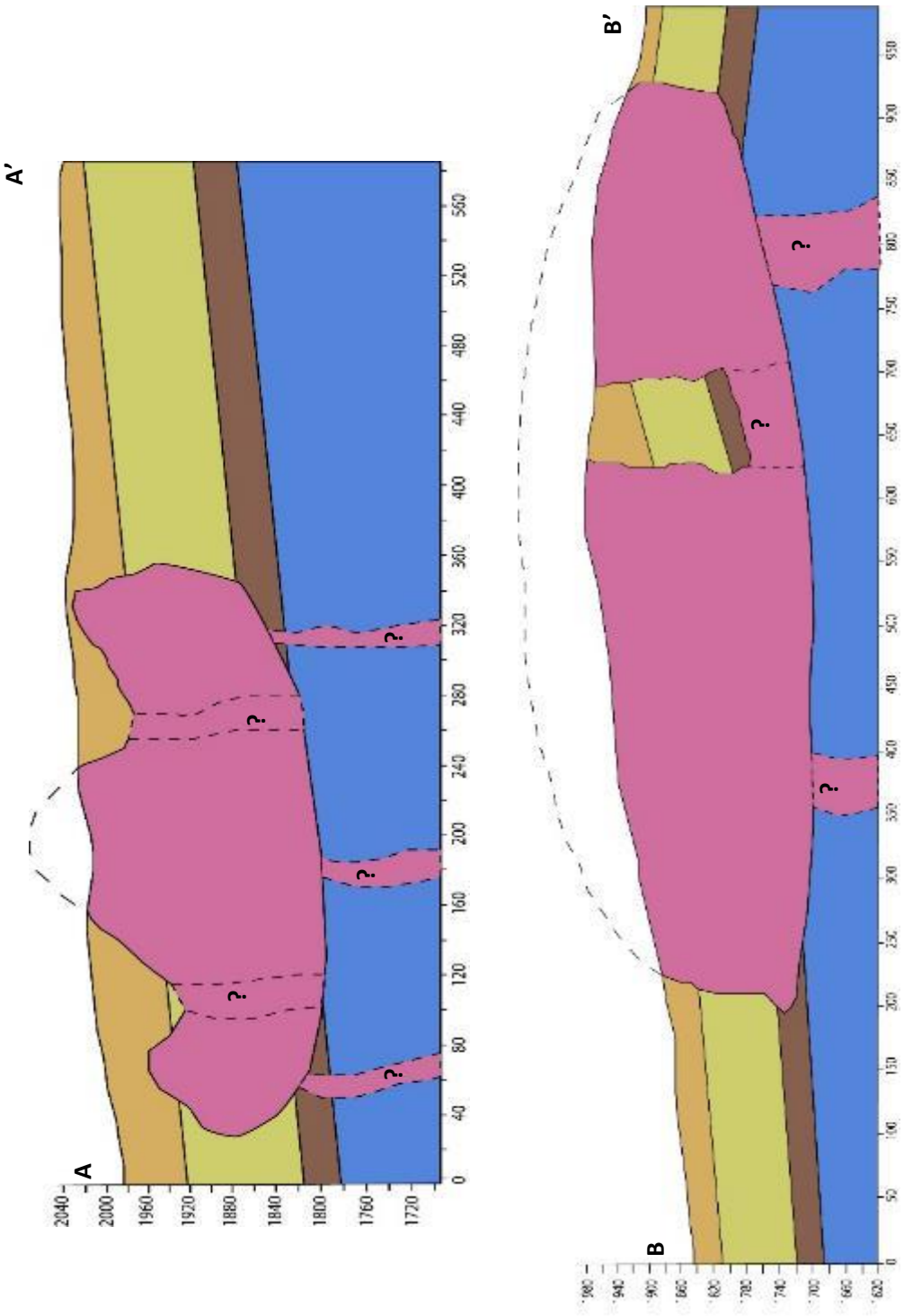

Figure 27. 2d profiles/Cross Sections intersecting the Sawtooth Ridge intrusion. Location of cross-section lines are shown in Figure 26. Porphyry is shown in pink, sedimentary host rocks shown in all other colors. '?' represents the uncertainty of intrusion geometry at depth.

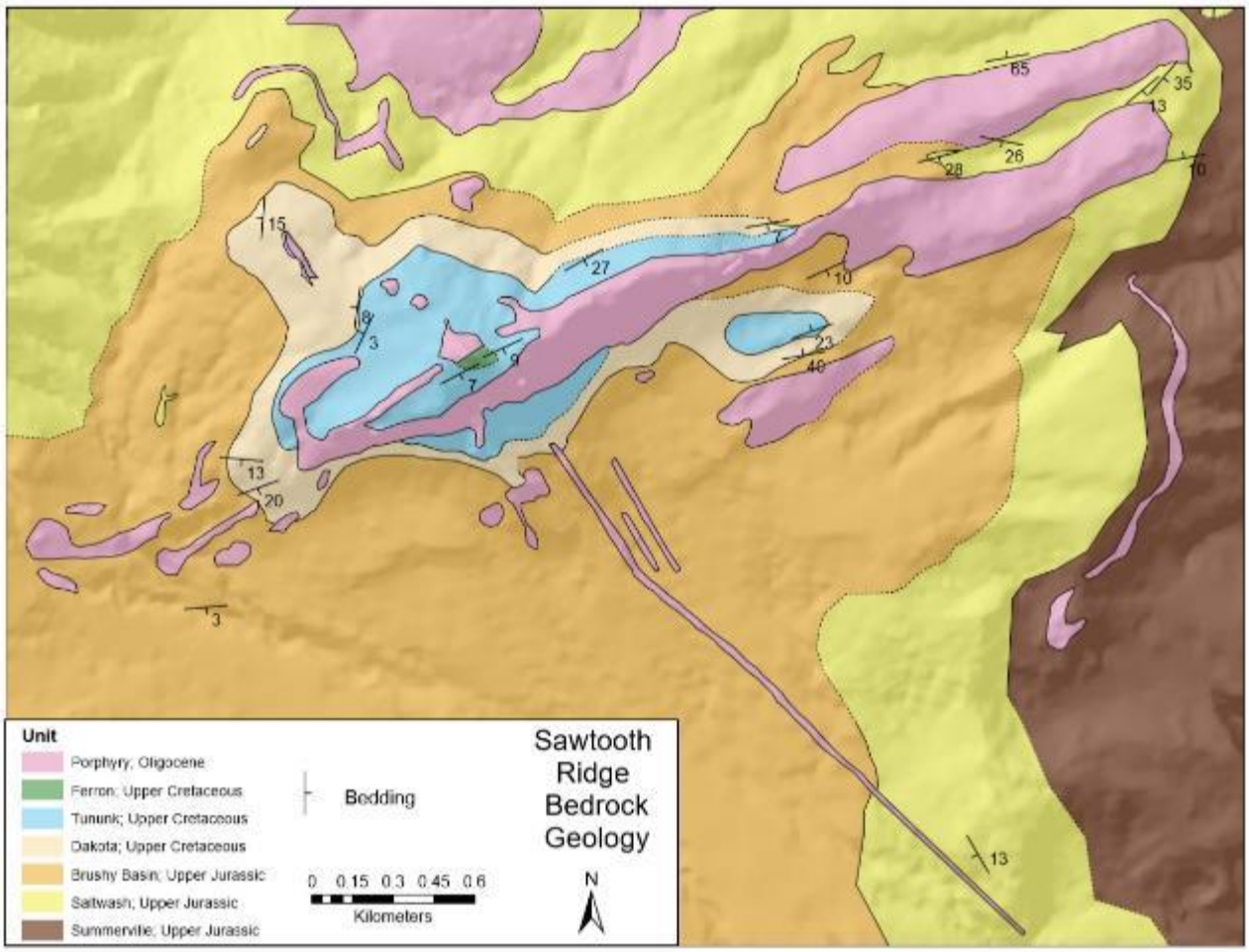

Figure 28 Local bedding measurements of sedimentary host rocks plotted atop Sawtooth Ridge bedrock geology.

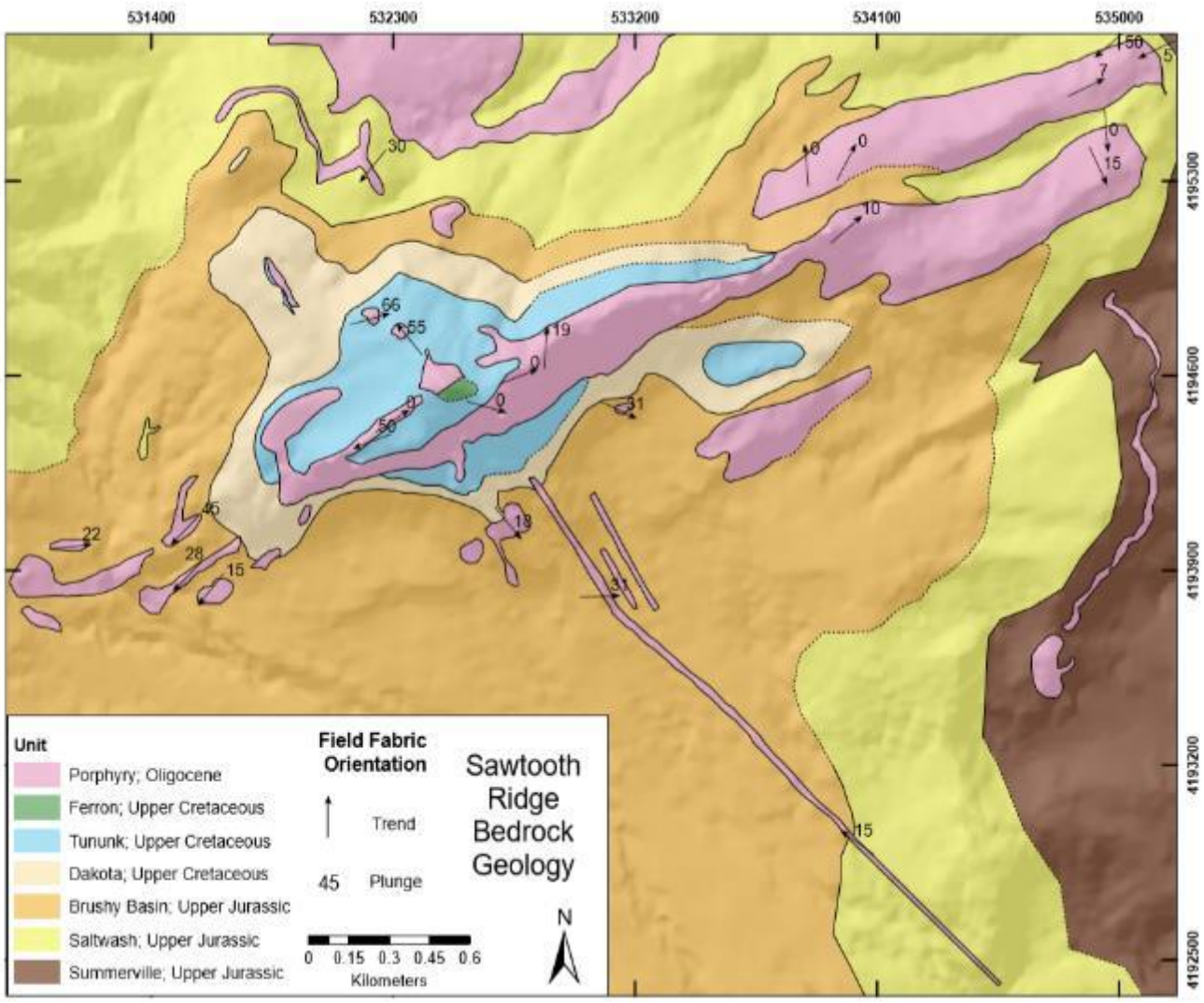

Figure 29. Field fabric measurements plotted atop Sawtooth Ridge bedrock geology.

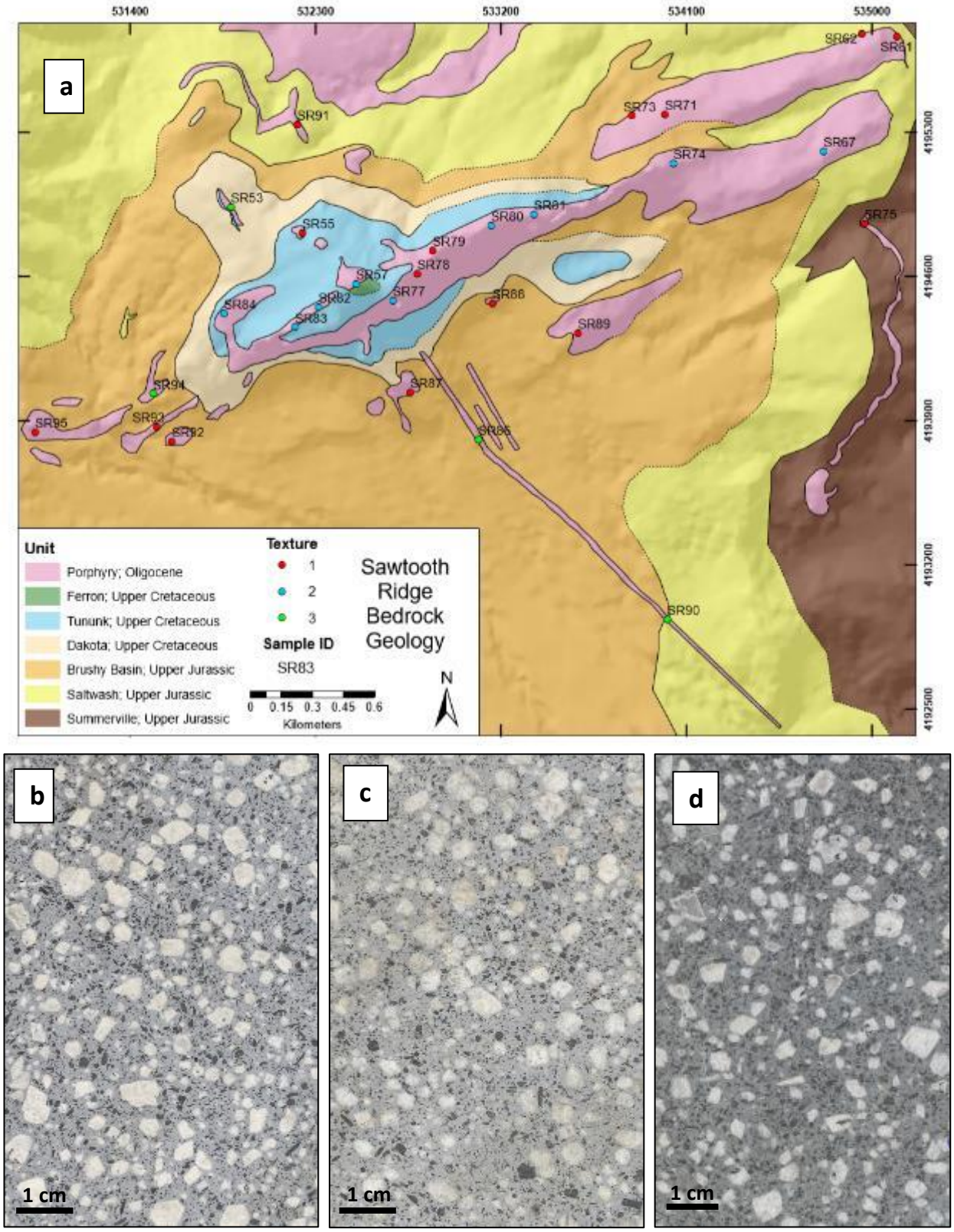

Figure 30. (a) Observed textural groupings plotted atop Sawtooth Ridge bedrock geology. (b) a scanned image of Texture 1. (c) a scanned image of Texture 2. (d) a scanned image of Texture 3.

b. Geochemistry

All geochemical data can be found in Appendix A. Total SiO_2 weight percent is plotted against total alkali oxide weight percent for all analyzed samples in Figure 31. As with most of the Henry Mountains' porphyry (Nelson and Davidson, 1993), all samples cluster on the border between andesite and trachyandesite compositions. Results are split into two clusters based on silica concentrations, however, within each cluster, concentrations are consistent. The 'silica rich' group displays silica concentrations that are 1-2% greater than the 'silica poor' group. Silica concentrations of the 'silica rich' group range from 60.81-61.54 weight percent with an average of 61.26% and a standard deviation of 0.27%. Silica concentrations of the silica poor group range from 59.04-59.94 weight percent with an average of 59.35% and a standard deviation of 0.34%.

In Figure 32, each cluster of silica concentrations is plotted atop a map of bedrock geology to show their spatial relationships. Samples from the 'silica rich' group plot along the main crest of the intrusion, the small isolated exposures of igneous rock in the SW portion of the map, and on one moderately sized isolated exposure off the SE side of the ridge crest (Fig. 32). Samples from the 'silica poor' cluster plot on the peak of the ridge crest, on the large isolated ridge of igneous exposure in the NW portion of the map, and on smaller features extending perpendicularly from the main ridge crest, including the long dike extending SE from the intrusion. Selected major and trace element compositions are shown plotted against total silica weight percent on Harker diagrams in Figure 33. There are little to no significant trends or differences in trace element concentrations between groups. The 'silica poor' group may be enriched in thorium compared to the 'silica rich' group, however, standard deviations suggest that these results are not significant.

Rare earth elements (RREs) are averaged for each group and normalized to CL Chondrite in Figure 34. The RRE averages of the 'silica rich' group are consistently less than those of the 'silica poor' group. However, the error bars plotted on the 'silica rich' group represent one standard deviation of this average and suggest that the difference in RREs may not be statistically significant. This is interesting because in a typical progression of fractional crystallization it is often the magma with a higher silica content that will also have higher concentrations of trace/RREs. However, in this case the 'silica poor' grouping has a higher concentration of trace/RREs. This seemingly backwards trend is also seen in a geochemical analysis of Henry Mountains porphyry conducted on the Copper Ridge intrusion on Mount Ellen (Maurer, 2015).

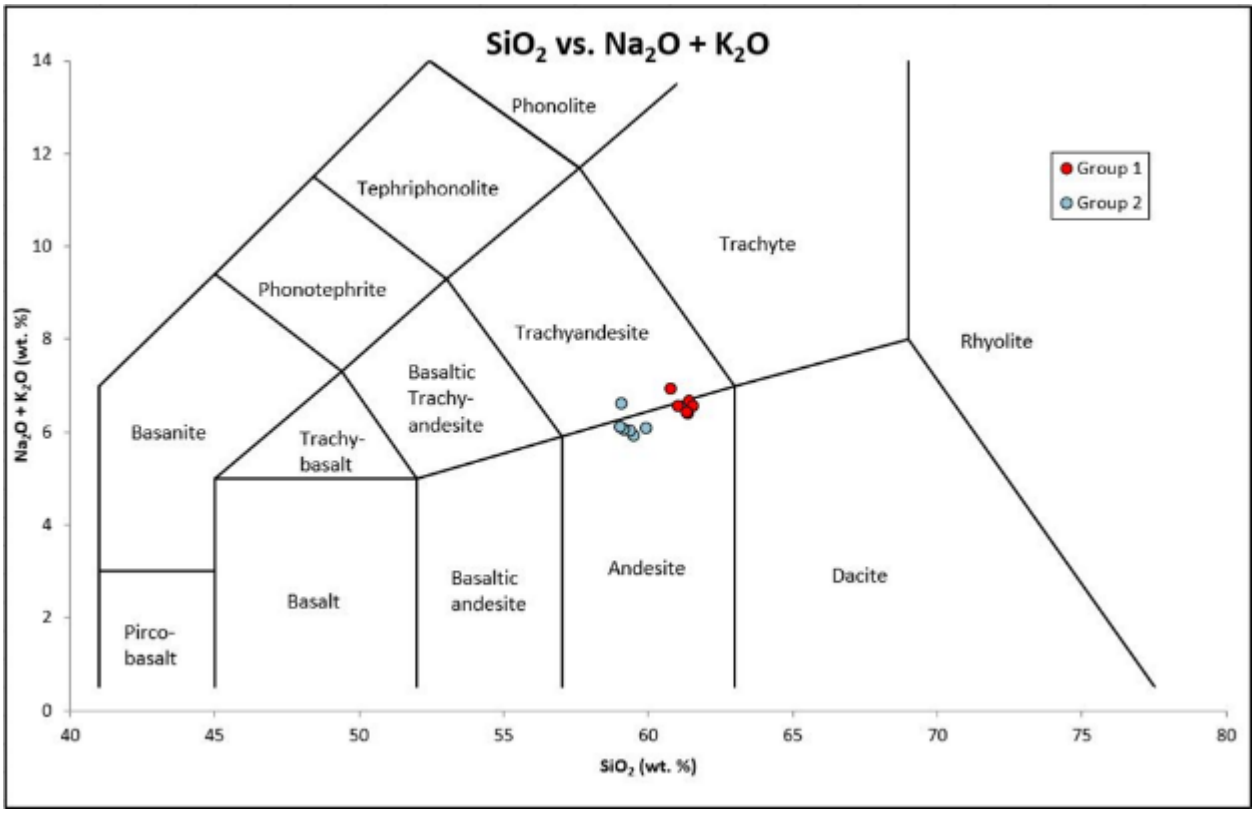

Figure 31. TAP classification diagram of samples from the Sawtooth Ridge Intrusion. Silica oxide weight percent plotted against total alkali oxide weight percent.

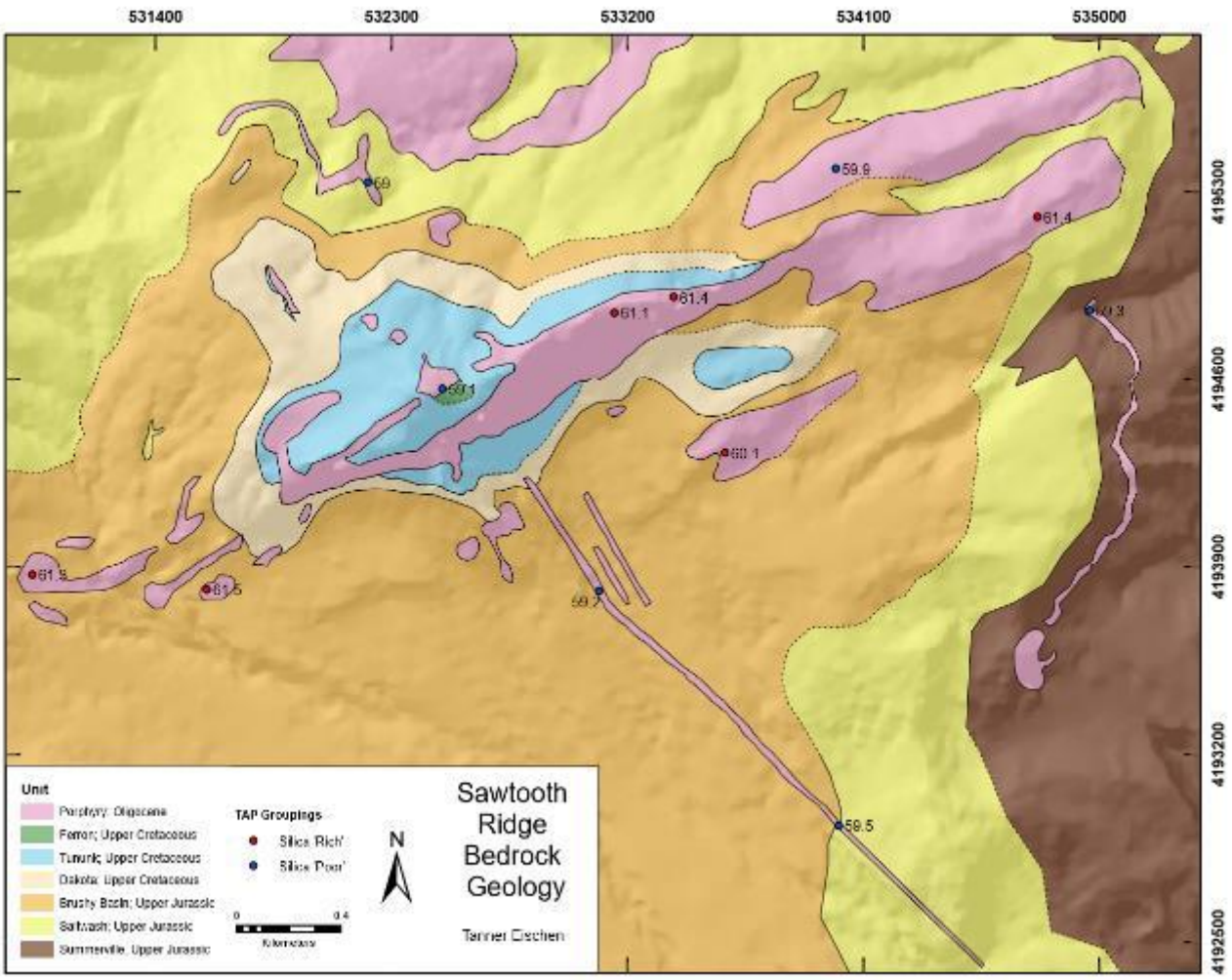

Figure 32. Map of the Sawtooth Ridge Intrusion showing the location of geochemical samples. The 'Silica Rich' grouping is shown in red while the 'Silica Poor' grouping is shown in blue. Numbered labels show total silica oxide weight percent for each sample.

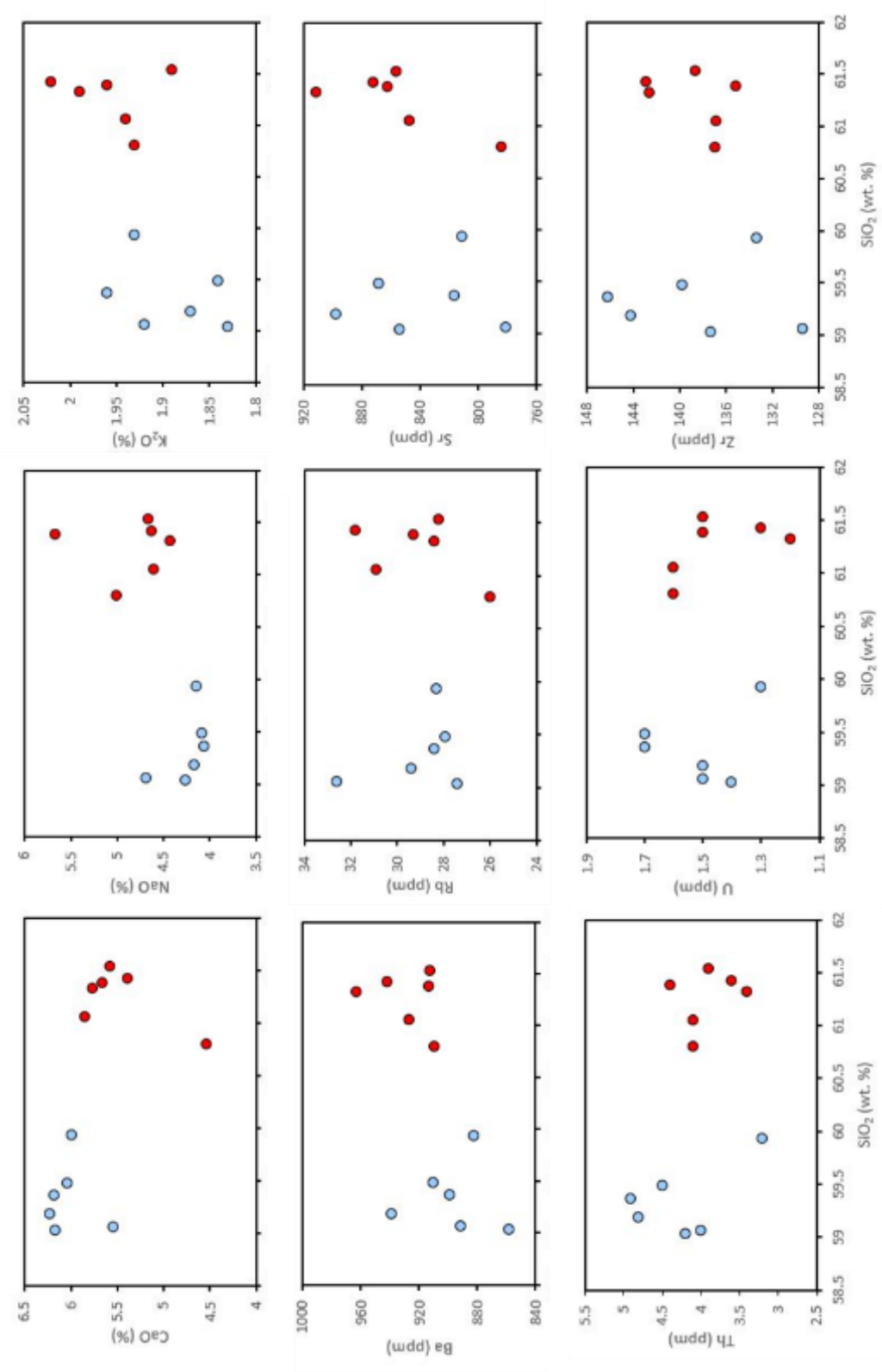

Figure 33. Harker diagram showing the relationship between SiO2 weight percent and different major and trace element concentrations. The 'Silica Rich' grouping is shown in red while the 'Silica Poor' grouping is shown in blue.

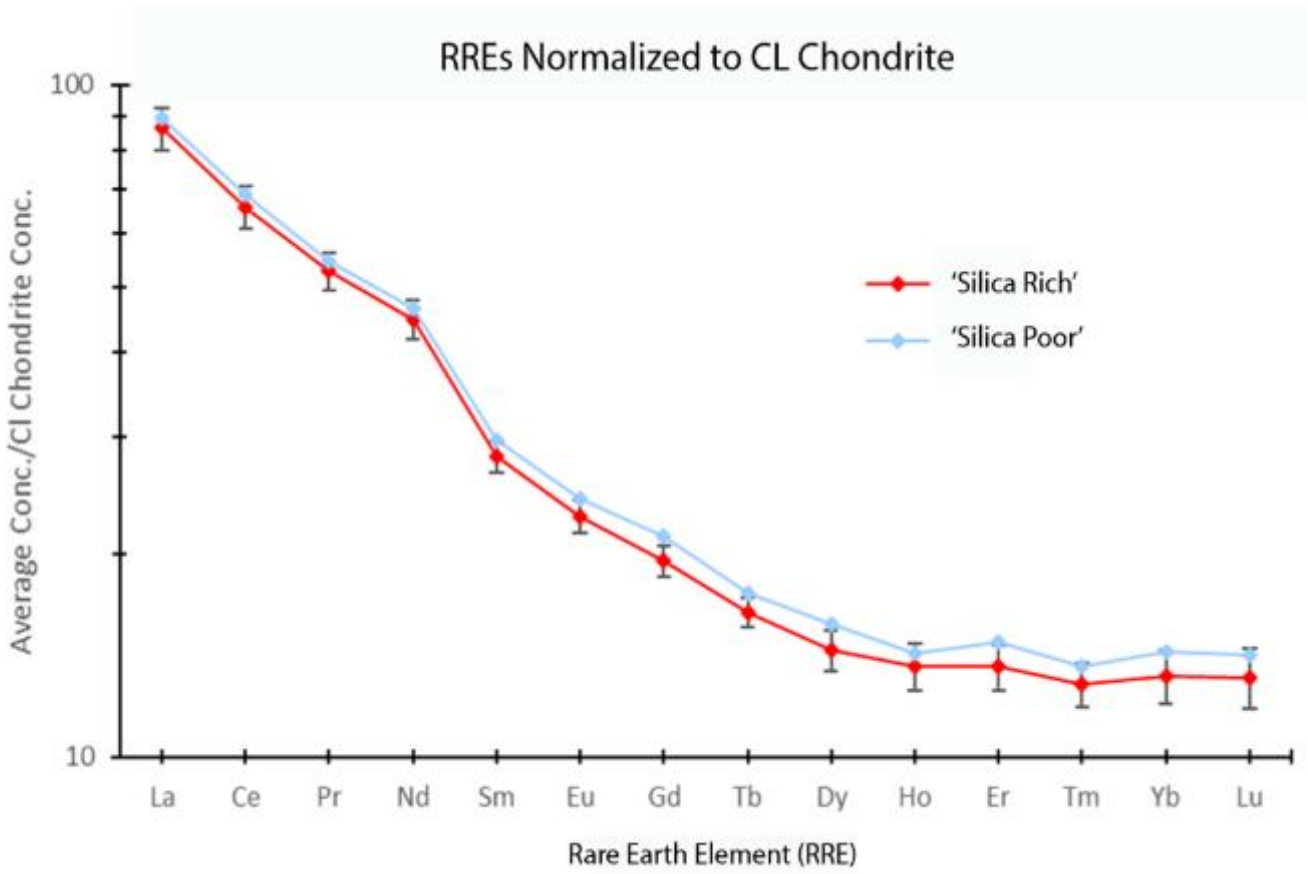

Figure 34. Spider plot showing the average RRE concentrations for both groupings normalized to the CL chondrite standard.

c. Anisotropy of Magnetic Susceptibility

All AMS data can be found in Appendix B. K_1 orientations (magnetic lineations) for each sample are plotted atop bedrock geology (Fig. 35). Individual stereonets for each sample are also plotted on a map of bedrock geology (Fig. 36). Each of these stereonets display the orientation of K_1, K_2, and K_3 axes and their respective confidence ellipses. These plots show that lineations are generally sub horizontal with variable trends.

The principal AMS axis orientations for all collected samples are plotted on an equal area lower-hemisphere stereographic projection in Figure 37. Plotted in this fashion, orientations of K_1, K_2, and K_3 appear to show no significant patterns or groupings. However, a strong girdle distribution with two local maxima exists in the orientation of K_1 axes. When separated by these two maxima, patterns in AMS data become recognizable (Figs. 38 and 39). K_1 orientations of *maximum 1* trend NE-SW with dominantly sub horizontal plunges (Fig. 38b), K_2 orientaions are sub vertical with variable trends (Fig. 38c), and K_3 orientations cluster in the NW quadrant with a sub horizontal plunge (Fig. 38d). K_1 orientations of *maximum 2* trend NW-SE with dominantly sub horizontal plunges (Fig. 39b), K_2 axes cluster in the SW quadrant with sub horizontal plunges (Fig. 39c), and K_3 axes cluster in the N-NE direction with variable plunges (Fig. 39d). Kamb contouring highlights the stark difference between K_1 orientations of *maximum 1* and *maximum 2* (Fig. 40a and b). In summary, K_1 axes (magnetic lineations) of *maximum 1* are oriented perpendicularly to the ridge crest with sub horizontal plunges, while K_1 axes (magnetic lineations) of maximum 2 are oriented parallel to the ridge crest with sub horizontal plunges.

The spatial extent of each maxima are plotted atop a map of Sawtooth Ridge igneous exposure in Fig. 41a and 41b. *Maximum 1*, which trends NE-SW, is located primarily in the southwestern portion of igneous exposure, and the northeastern-most lobe of igneous rock that

appears to be disconnected from the main ridge crest. *Maximum* 2, which trends NW-SE, is located along the northeastern portion of the main ridge crest and on many of the smaller perpendicular features extending from the main intrusive feature. Following the intrusion along its crest from the SW to the NE, there appears to be a transition in magnetic fabric orientation near the highest peak of the intrusion. At this point, magnetic fabric lineations transition from a ridge-parallel orientation to a ridge-perpendicular orientation.

AMS scalar parameters are plotted in Figure 42 and are separated into *maximum 1* and *maximum 2*. There are no apparent trends in bulk susceptibility (K_m) between *maximum 1* and *maximum 2* (Fig. 42a). Bulk susceptibilities of *maximum 1* range from 3.9×10^{-4} SI to 1.36×10^{-2} SI with an average of 9.15×10^{-3} SI and a standard deviation of 3.52×10^{-3} SI. Bulk susceptibilities of *maximum 2* range from 2.84×10^{-4} SI to 1.55×10^{-2} SI with an average of 8.39×10^{-3} SI and a standard deviation of 3.45×10^{-3} SI.

Shape factor (T) values of *maximum 1* range from -0.701 to 0.807 with an average of 0.132 and a standard deviation of 0.379. Shape factor values of *maximum 2* range from -0.374 to 0.665 with an average of 0.077 and a standard deviation of 0.342. The majority of samples from *maximum 1* plot in the oblate range with three samples plotting in the prolate range (Fig. 42b). Approximately fifty percent of samples from *maximum 2* plot in the oblate range and fifty percent in the prolate range. There are no apparent trends between T and Km (Fig. 42a)

The corrected degree of anisotropy (P_j) of *maximum 1* ranges from 1.013 to 1.052 with an average of 1.023 and a standard deviation of 0.010. The corrected degree of anisotropy of *maximum 2* ranges from 1.009 to 1.027 with an average of 1.018 and a standard deviation of 0.006. There are no trends between either P’ and T, or P’ and Km (Figs. 42b and c).

Lineation (L) values between maxima 1 and 2 are very similar. Lineation values of *maximum 1* range from 1.001 to 1.017 with an average of 1.009 and a standard deviation of 0.005. Lineation values of *maximum 2* range from 1.002 to 1.016 with an average of 1.008 and a standard deviation of 0.004. *Maximum 2* has both a smaller range of foliation (F) values and a smaller average than *maximum 1*. Foliation (F) values for *maximum 1* range from 1.002 to 1.034 with an average of 1.013 and a standard deviation of 0.008. Foliation values of *maximum 2* range from 1.003 to 1.015 with an average of 1.009 and a standard deviation of 0.004. There are no trends between L and F (Fig. 42d).

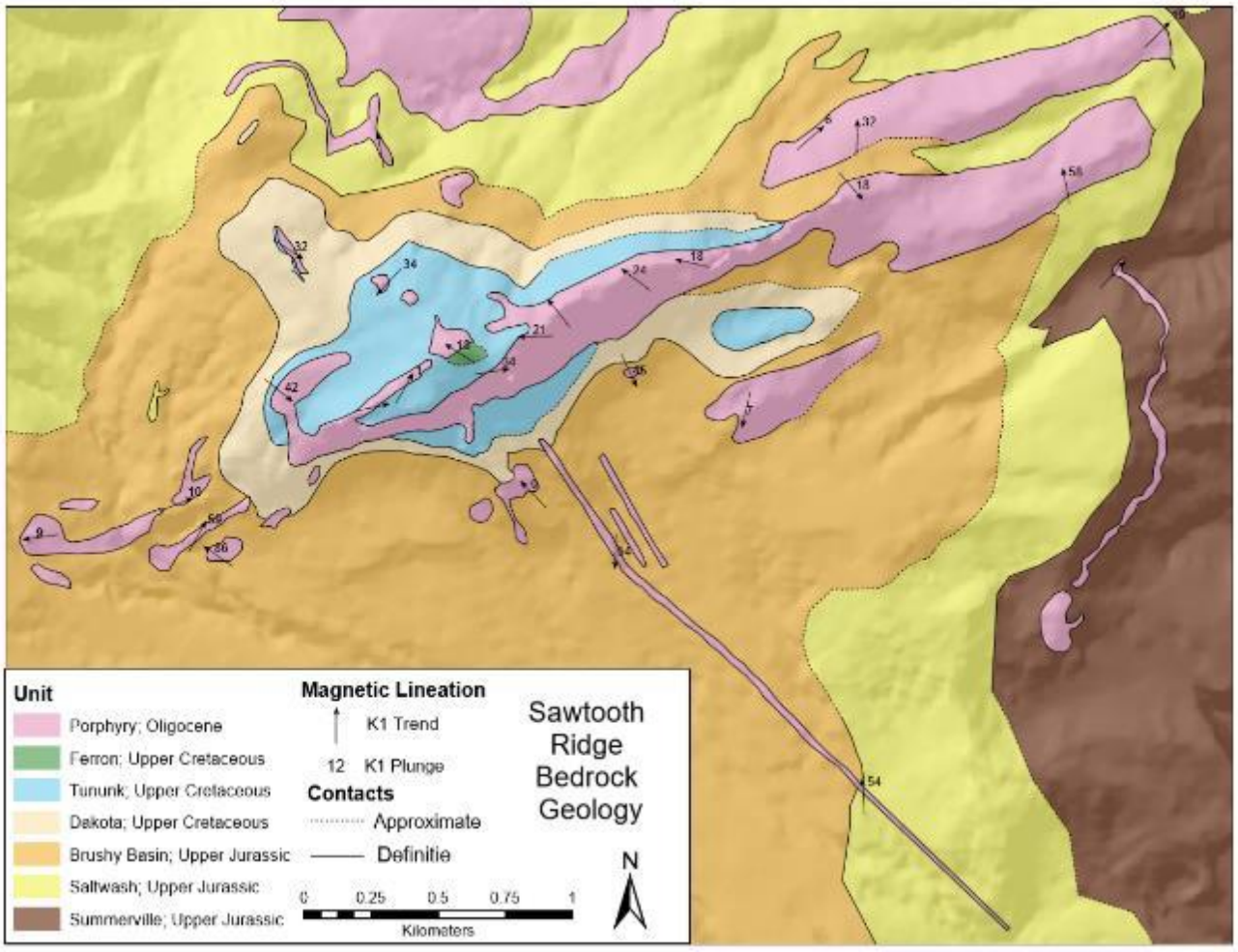

Figure 35. Map of Sawtooth Ridge showing the orientation of calculated AMS major axis lineations.

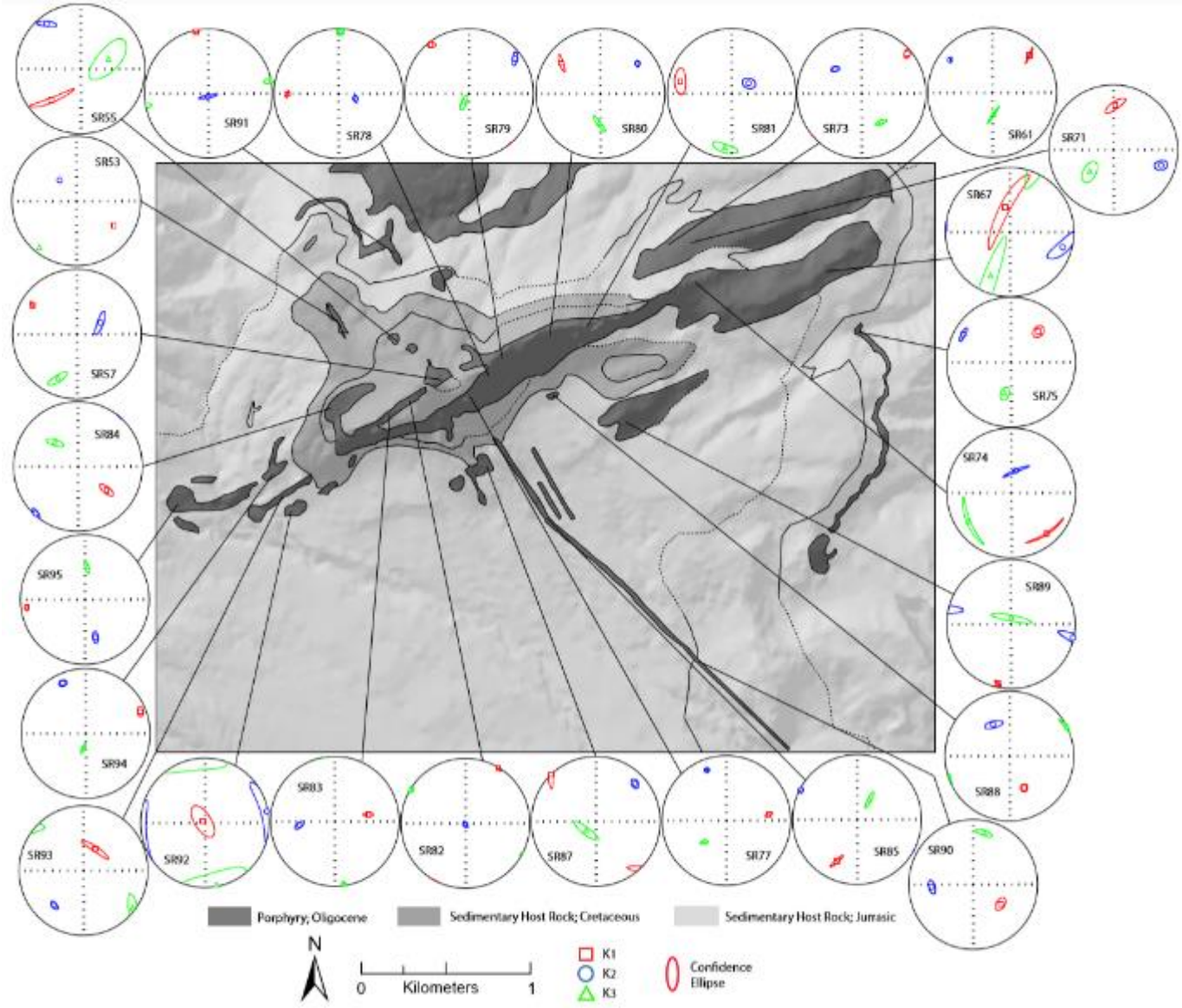

Figure 36. Map of Sawtooth Ridge showing calculated AMS fabric ellipsoids for each sample location.

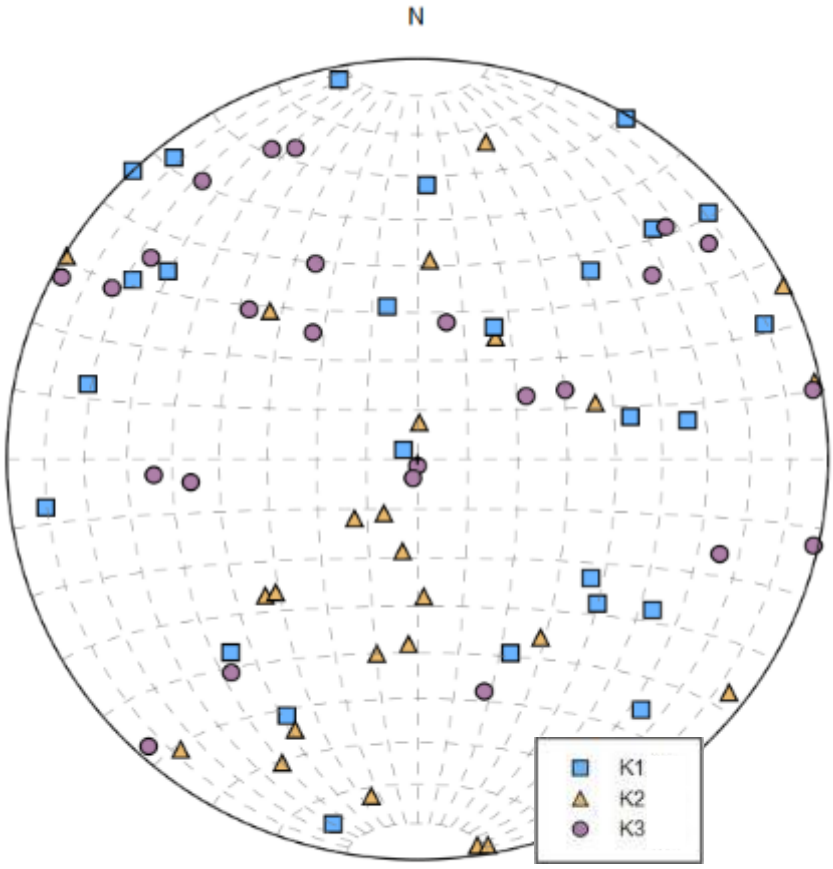

Figure 37. Calculated AMS ellipsoids plotted on equal area lower hemisphere stereographic projection. Shows orientations of K1, K2, and K3.

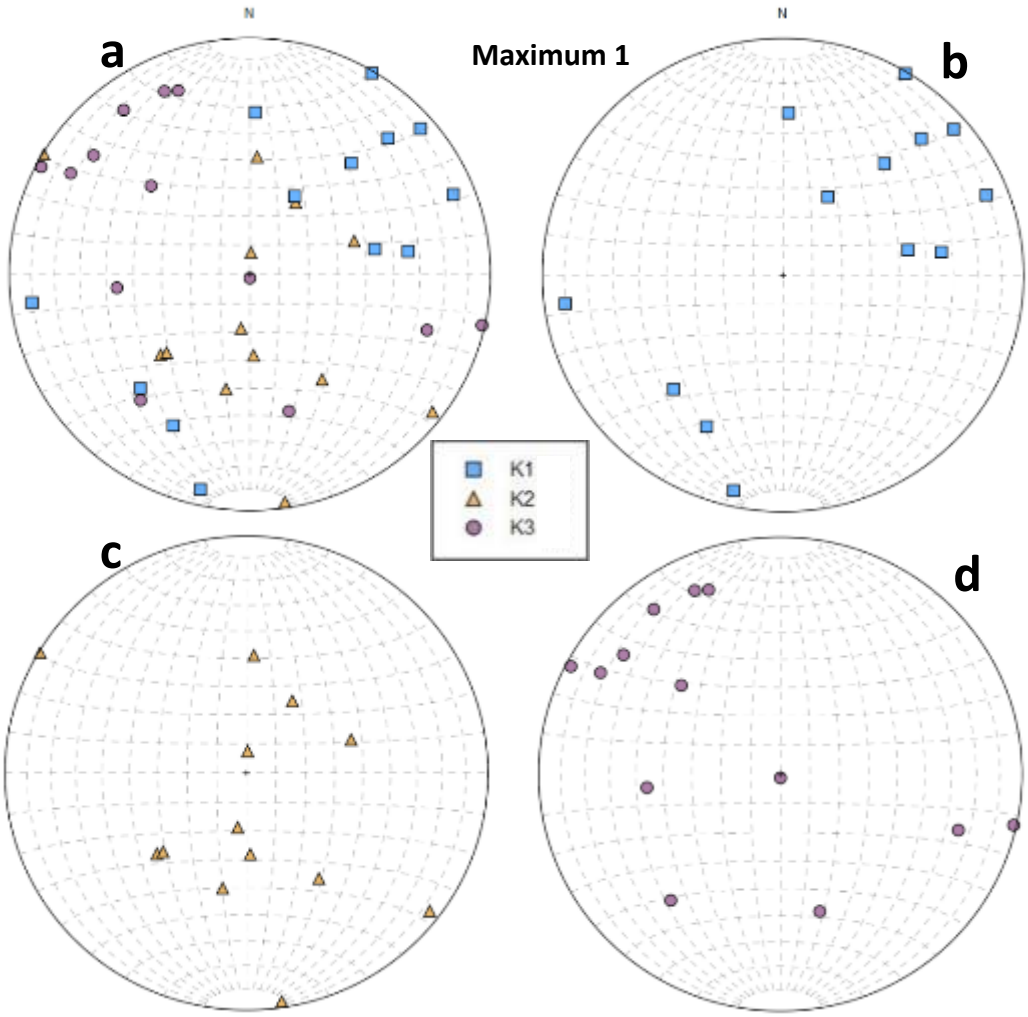

Figure 38. Equal area lower hemisphere stereographic projections of samples that constitute maximum 1 (NE-SW). (a) maximum 1 K1, K2, and K3 orientations; (b) Maximum 1 K1 orientations; (c) Maximum 1 K2 orientations; (d) Maximum 1 K3 orientations.

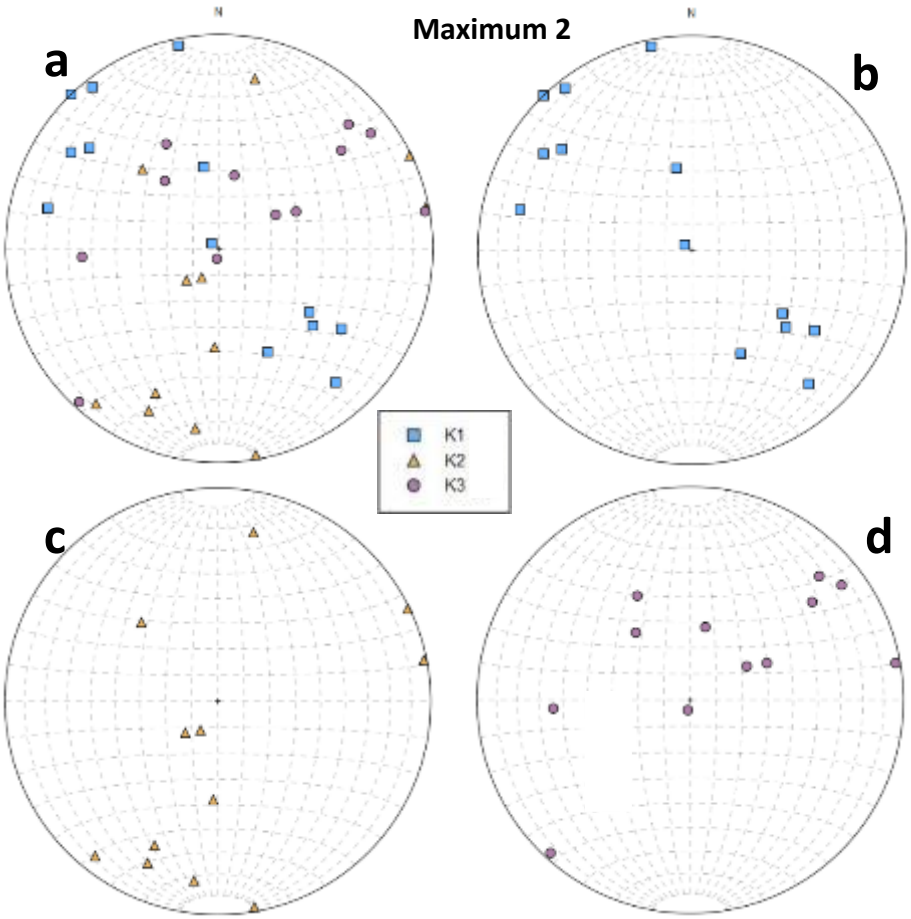

Figure 39. Equal area lower hemisphere stereographic projections of samples that constitute maximum 2 (NW-SE). (A) Maximum 2 K1, K2, and K3 orientations; (B) Maximum 2 K1 orientations; (C) Maxima 2 K2 orientations; (D) Maximum 2 K3 orientations.

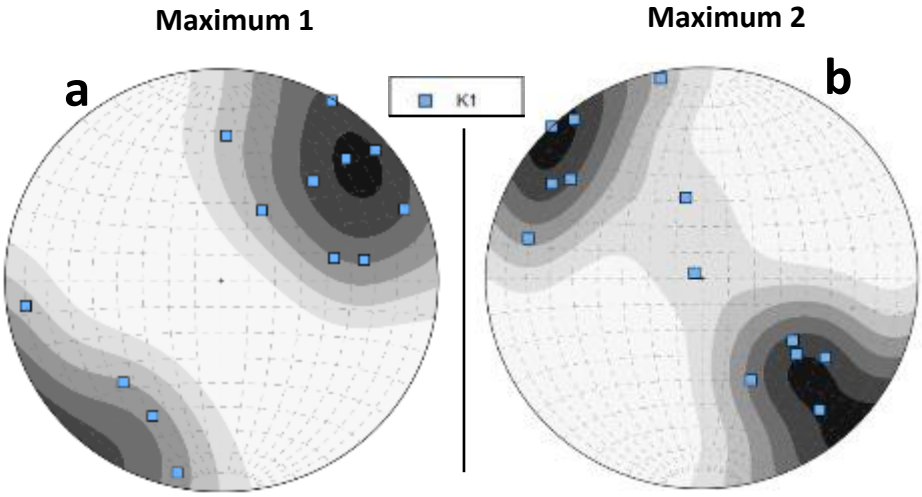

Figure 40. Equal area lower hemisphere stereographic projections juxtaposing maximum 1 against maximum 2. (a) K1 orientations for samples that constitute maximum 1 shown with exponential Kamb contours. (b) K1 orientations for samples that constitute maximum 2 shown with exponential Kamb contours.

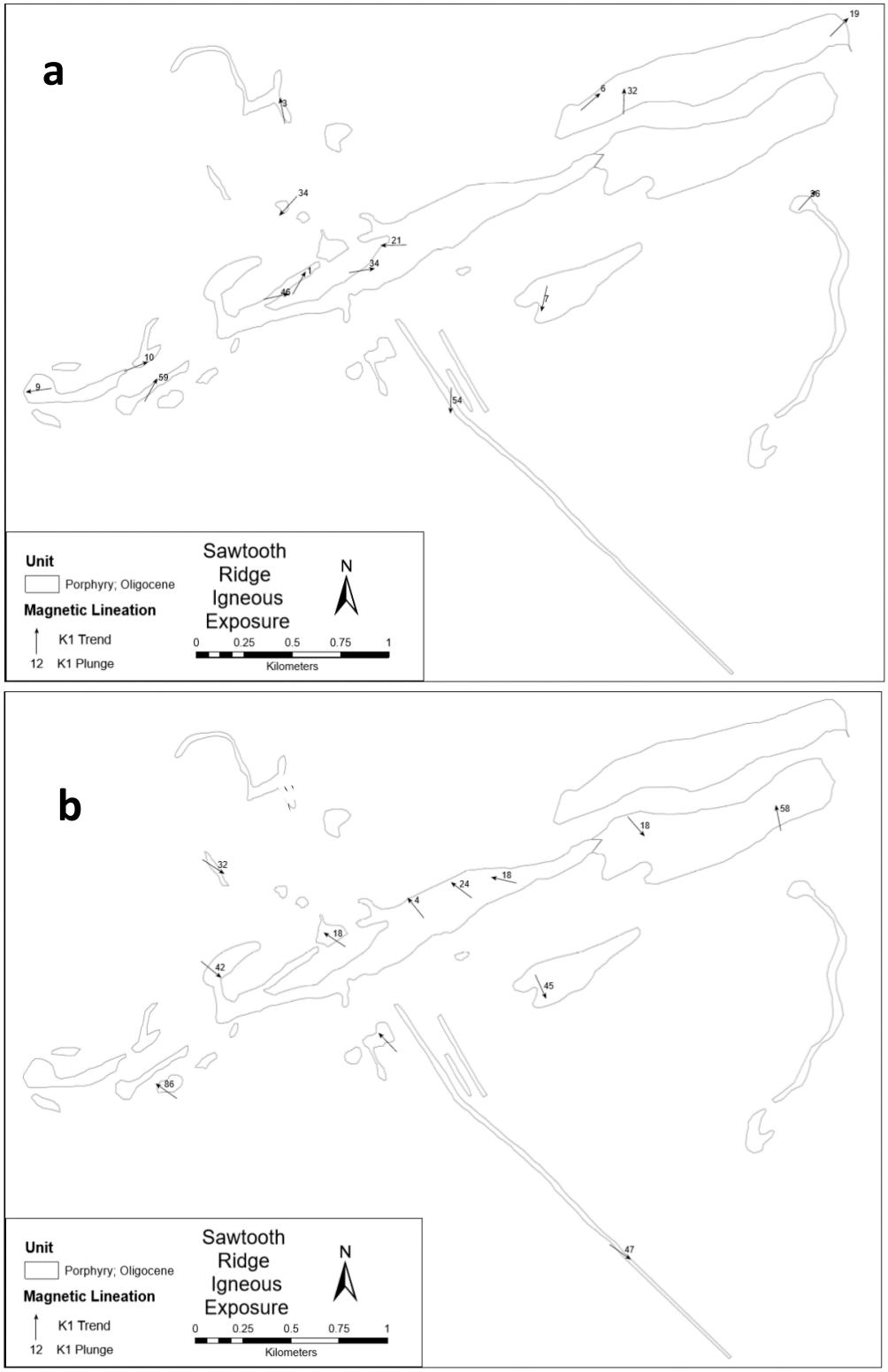

Figure 41. Maps of Sawtooth Ridge Igneous exposure showing (a) the calculated AMS major axis lineations for maximum 1 (b) the calculated AMS major axis lineations for maximum 2.

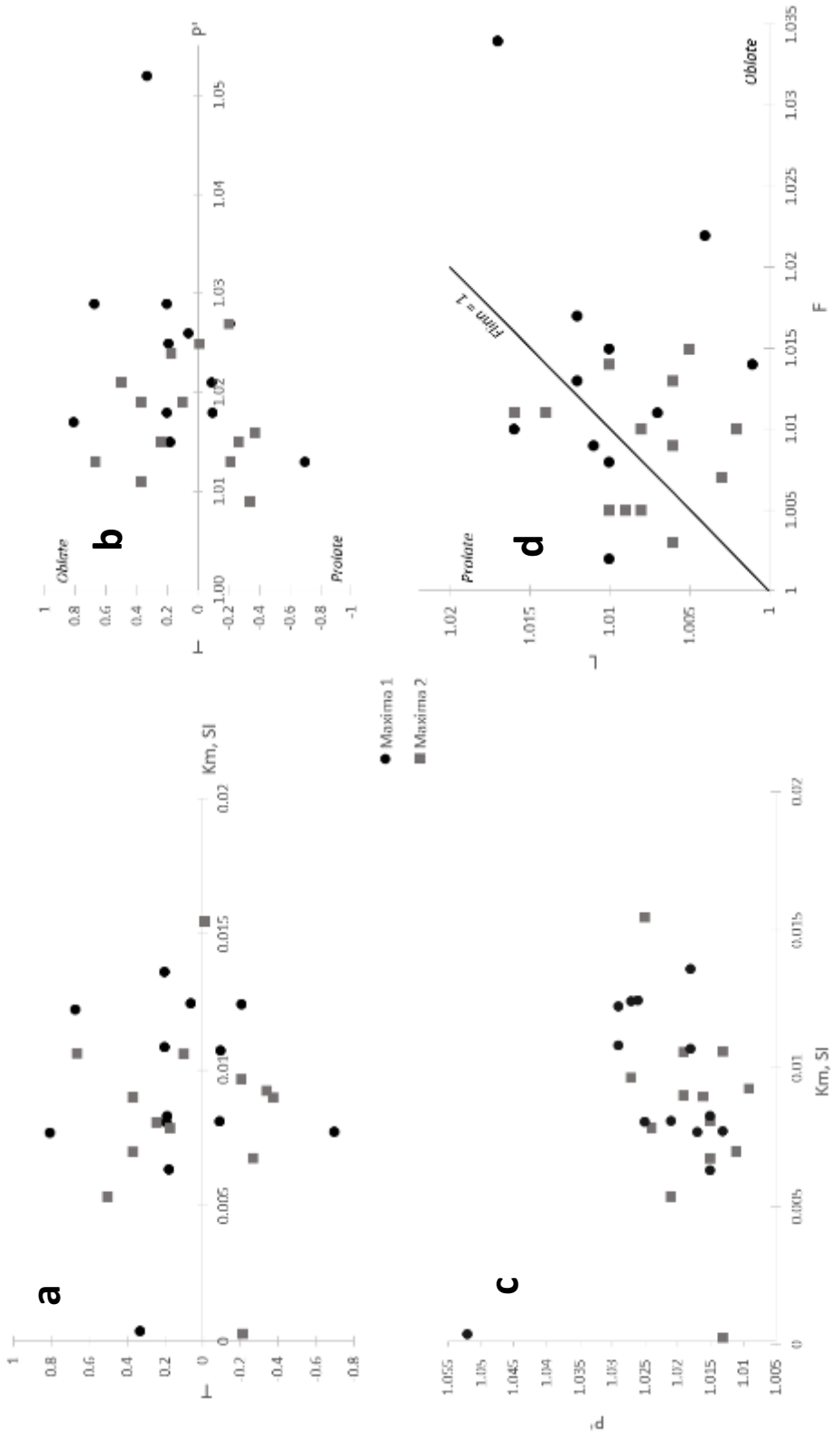

Figure 42. AMS scalar parameters plotted for all samples in maxima 1 and maxima 2. (a) Shape Factor vs. Mean Susceptibility (b) Shape Factor vs. Corrected Degree of Anisotropy (c) Corrected degree of Anisotropy vs. Mean Susceptibility (d) Lineation vs. Foliation

d. Shape Preferred Orientation

All SPO data can be found in Appendix C. K_1 orientations (lineations) for each sample are plotted atop bedrock geology in Figure 43. SPO results display a similar trend to AMS orientations; fabrics trend parallel to the main ridge crest in the SW portion of the intrusion and appear to transition to a perpendicular orientation beginning near the crest of the ridge and extending through the NE portion of the intrusion. Generally, K_1 orientations trend NW-SE and have moderate to shallow plunges (Fig. 43). This is highlighted by Kamb contouring of K_1 orientations in Figure 45. K_2 orientations cluster in the SW quadrant with plunges ranging from shallow-steep. K_3 orientations have variable trends but display a strong clustering in the NE quadrant and have trends ranging from moderate-steep.

As with AMS, scalar parameters can be calculated for SPO and are plotted in Figure 46. Shape factor (T) values range from -0.831 to 0.696 with an average of 0.081 and a standard deviation of 0.389. The majority of SPO ellipsoids plot in the oblate field. There are no observable trends between T and P'. The corrected degree of anisotropy (P') ranges from 1.045 to 1.277 with an average of 1.094 and a standard deviation of 0.0624.

Lineation (L) values range from 1.01 to 1.142 with an average of 1.044 and a standard deviation of 0.038. Foliation (F) values range from 1.008 to 1.118 with an average of 1.045 and a standard deviation of 0.0281. The majority of SPO ellipsoids are slightly oblate. There are no observable trends between L and F.

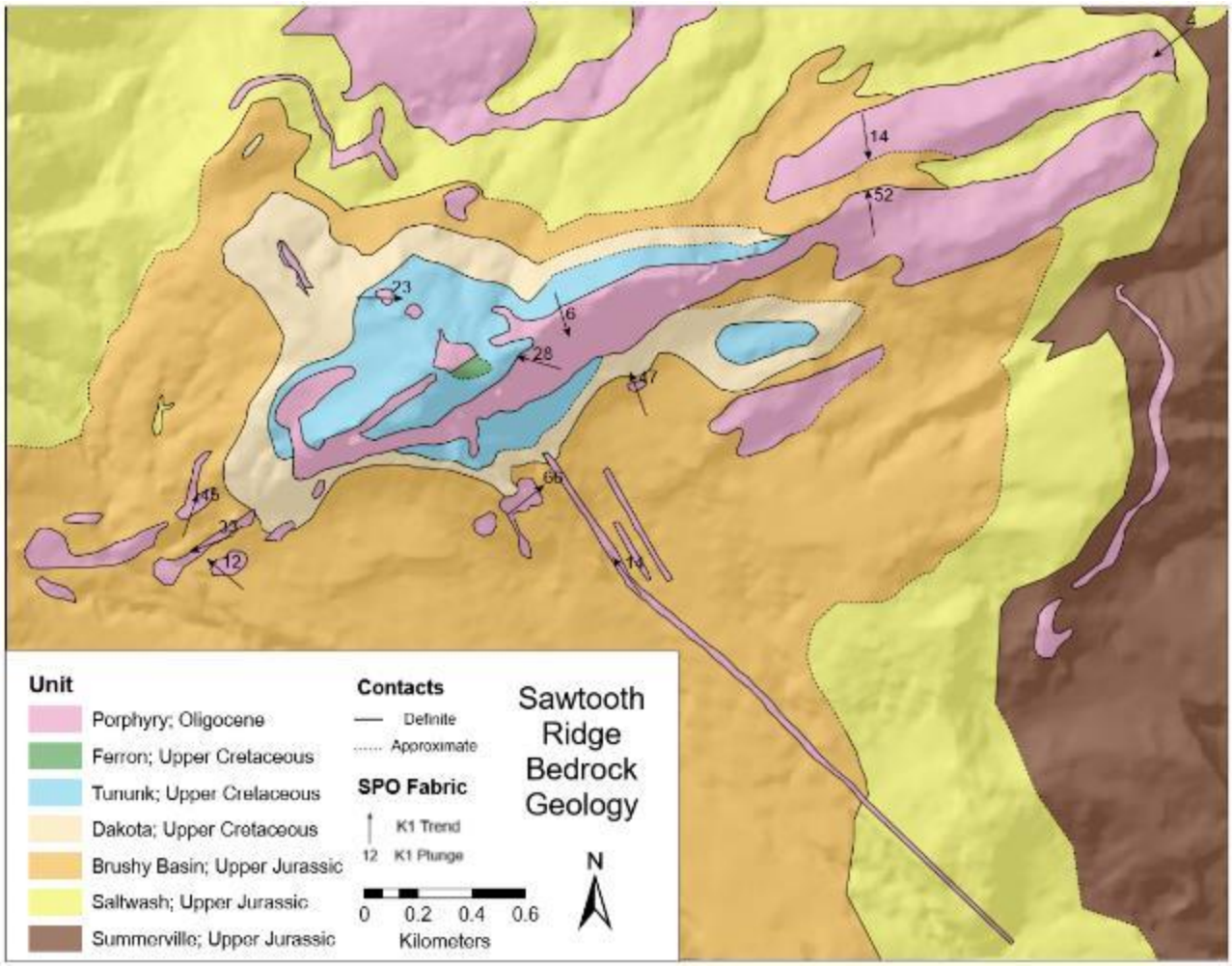

Figure 43. Map of Sawtooth Ridge showing the orientations of calculated SPO major axis lineations.

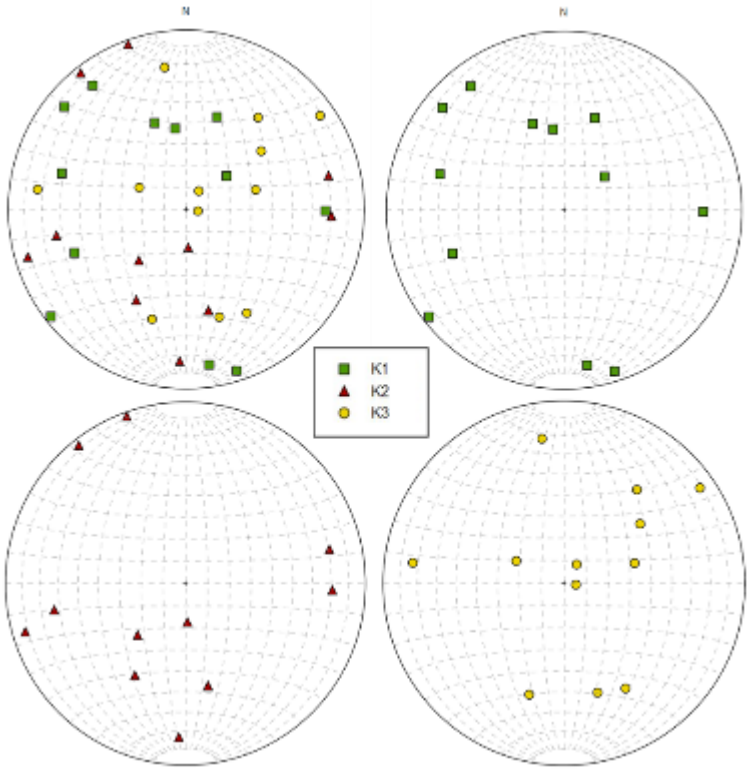

Figure 44. Equal area lower hemisphere stereographic projections of calculated SPO ellipsoids (a) K1, K2, and K3 orientations; (b) K1 orientations; (c) K2 orientations; (d) K3 orientations

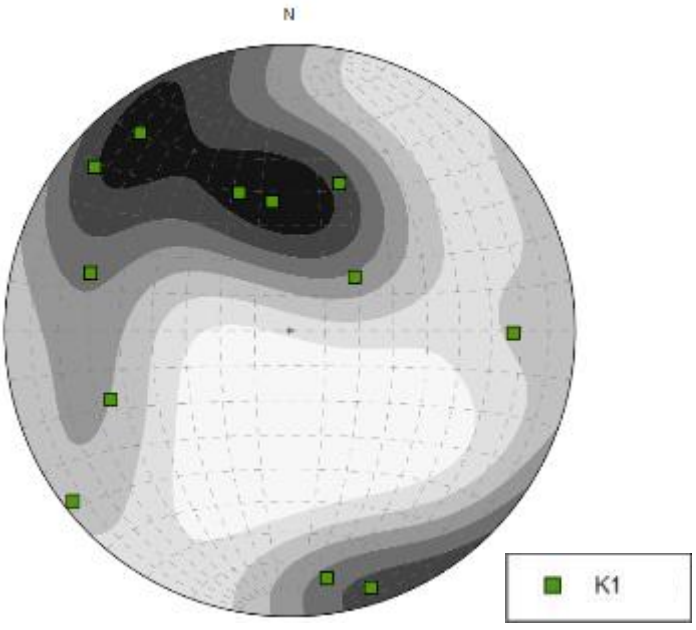

Figure 45. Equal area lower hemisphere stereographic projection of SPO K1 axes with exponential Kamb contouring.

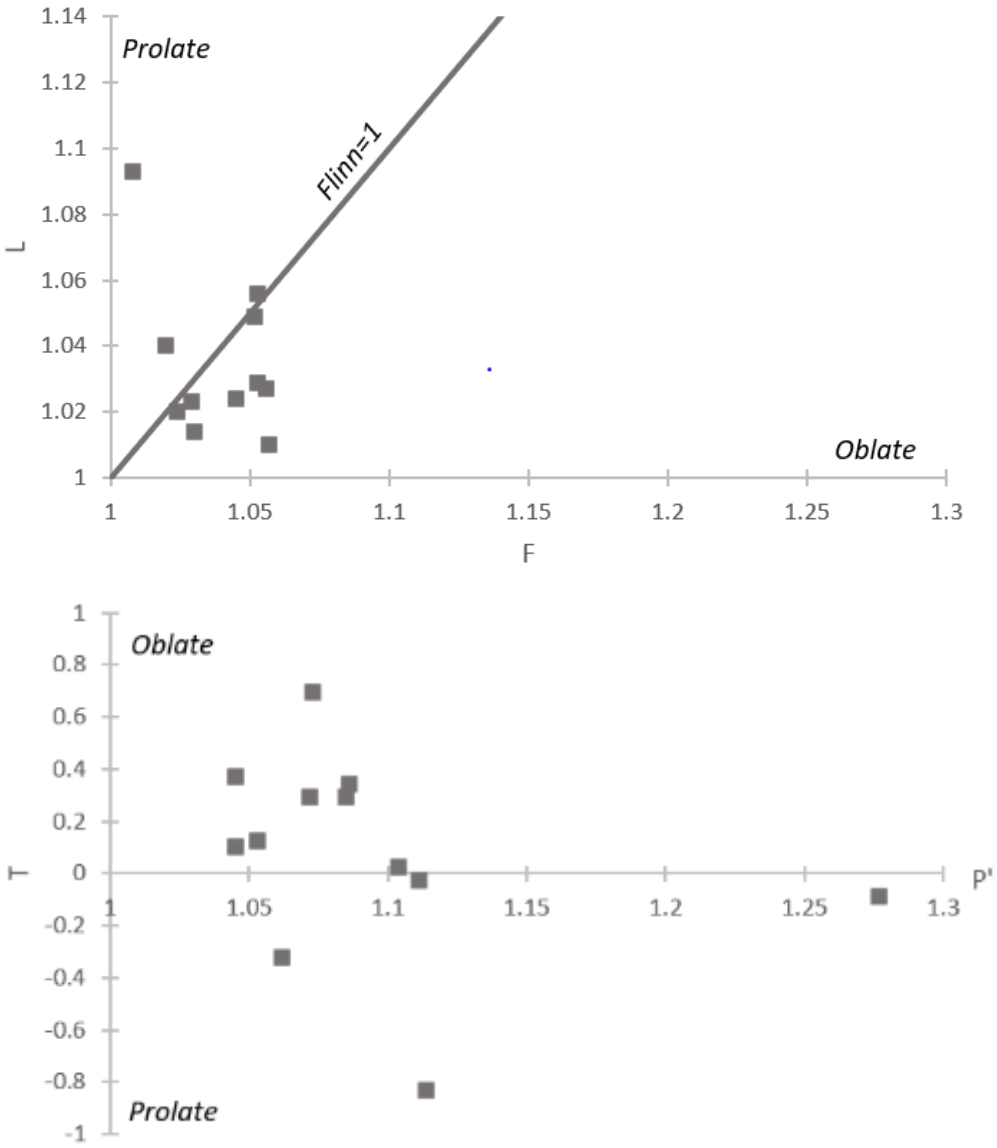

Figure 46. SPO scalar parameters (a) Lineation vs. Foliation (b) Shape Factor vs. Corrected Degree of Anisotropy

e. Comparison of Fabric Measurement Techniques

Three different methods were used to quantify magmatic fabric orientations: measurement of field fabric, analysis of AMS, and image analysis of SPO. Each of these techniques measure different aspects of magmatic fabric and each have their own strengths and limitations. For example, measurements of fabric in the field are often limited by the quality of igneous exposure and is a qualitative measurement, however, it is a nondestructive technique that requires little time to complete. On the other hand, AMS and SPO provide much more quantified results. However, they utilize different measurements in doing so. In the henry mountains porphyry AMS acts as a proxy for the orientation of microcrystalline magnetite grains while SPO directly measures the orientation of hornblende phenocrysts. So, it is useful to compare the results of each technique.

For twelve samples the orientations K1, K2, and K3 for SPO and AMS analyses, and the orientation of K1 for field measurements are plotted on equal area lower hemisphere stereographic projections. Several samples display very similar results across all three fabric measurement techniques. Samples SR61, SR71, SR78, and SR79 display very strong correlations between each of the techniques (Fig. 47). However, other samples display only a correlation between two of the techniques (SR55, SR87, SR88, SR93) (Fig. 48), while some display little to no correlation across techniques (SR74, SR85, SR92, SR94) (Fig. 49).

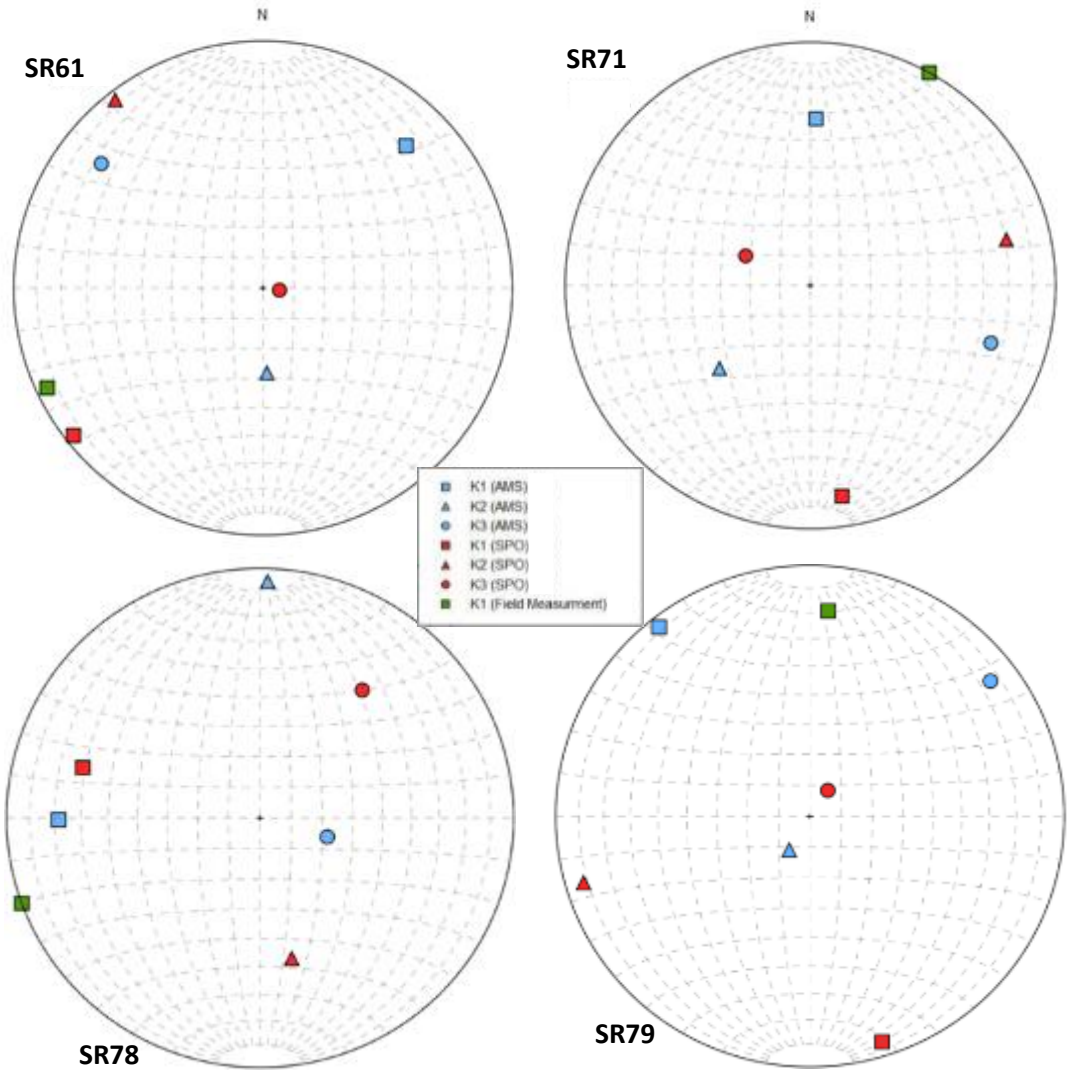

Figure 47. Equal area lower hemisphere projections comparing all fabric measurement techniques for samples SR61, SR71, SR78, and SR79.

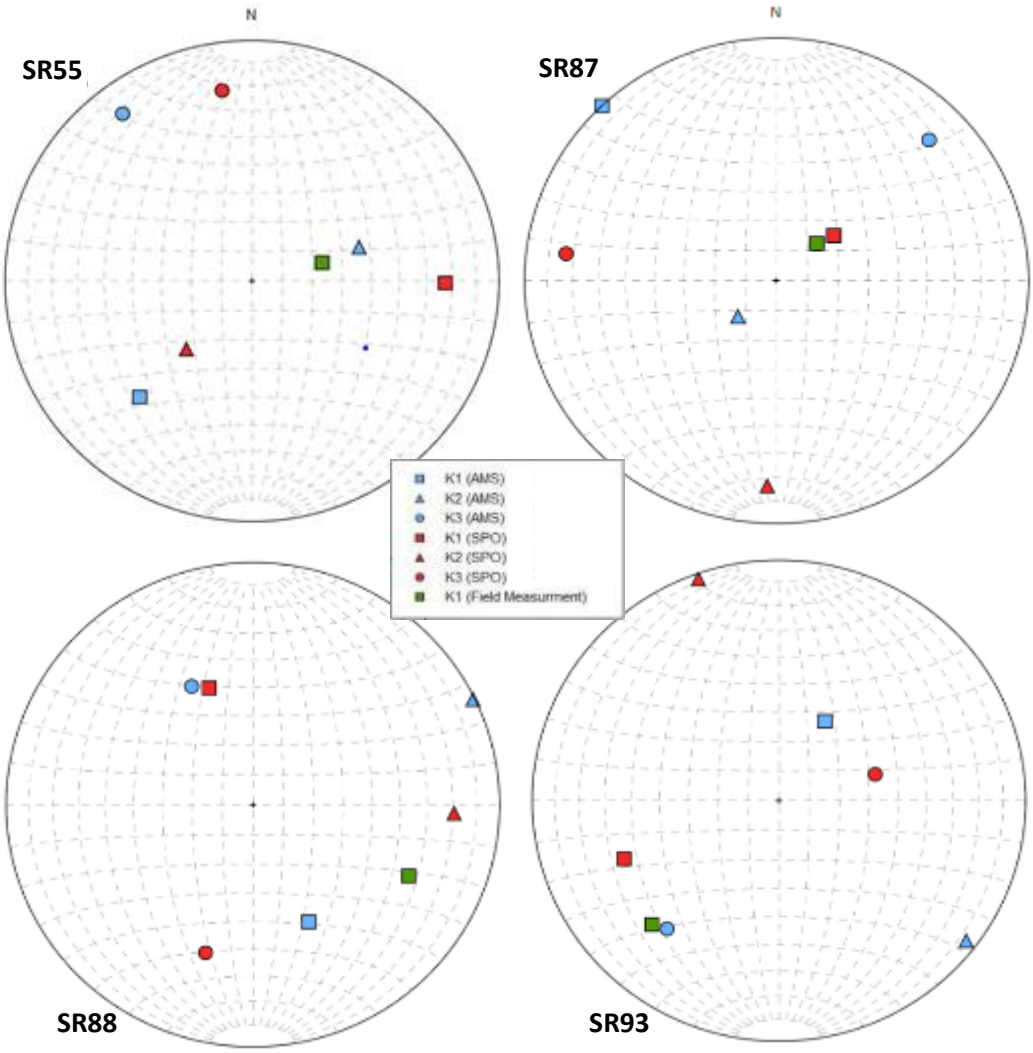

Figure 48. Equal area lower hemisphere projections comparing all fabric measurement techniques for samples SR55, SR87, SR88, and SR93.

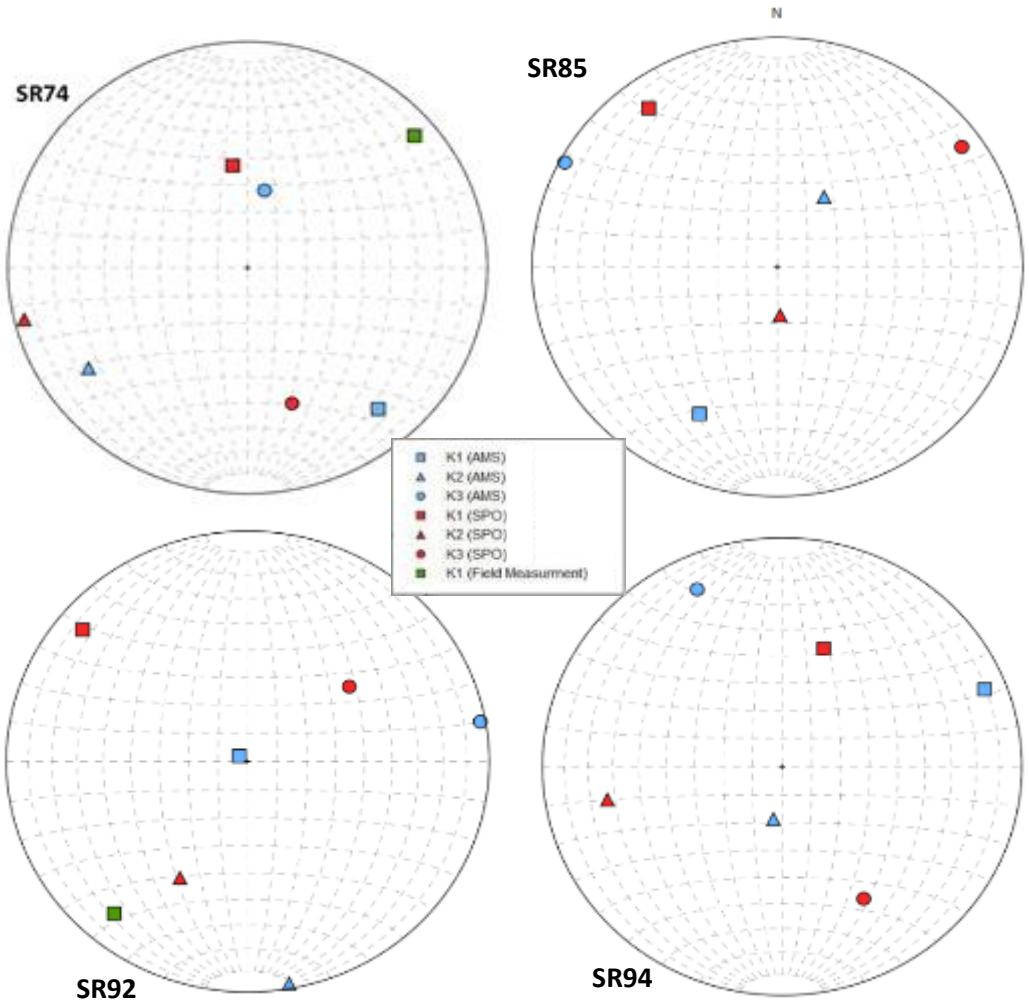

Figure 49. Equal area lower hemisphere projections comparing all fabric measurement techniques for samples SR74, SR85, SR92, and SR94.

f. Magnetic Anomaly Modelling

Magnetic anomaly data were collected along three transects over the Sawtooth Ridge intrusion to provide constraints on the intrusion's subsurface geometry. The locations of these transects are shown in Figure 50. Transect 1is 620 meters long and crosses a feature with which there are strong constraints on subsurface geometry; a dike extending several kilometers from the SE face of the Sawtooth Ridge intrusion. Transects 2 and 3 were chosen to constrain the subsurface geometries of the SW and NE ends of the intrusion, and are 575 and 750 meters long, respectively. Magnetic data were collected every second along each transect using a Geometrics G858 cesium-vapor magnetometer. Data were picked to remove anomalies from nearby culverts, de-spiked, and smoothed.

To test possible intrusion geometries, anomaly data were forward modelled as dikes, sills, and finger-like lobes/tubes using GeoSoft's GM-SYS software. Each block represents a 2.5-dimensional model that attempts to simulate a block of Morrison Formation country rock intruded by varying porphyry geometries. The magnetic susceptibility of porphyry samples was determined using a magnetic susceptibility bridge during AMS analysis, and the magnetic susceptibility of Morrison Formation rocks was assumed to be zero because the susceptibilities of clastic sedimentary rocks are typically several orders of magnitude lower than magnetite-containing igneous rocks. Dikes were modelled as vertical tabular features extending to an infinite depth and ending a few meters below the surface based on the depth of the dike intersected by Transect 1. Sills and finger-like bodies were modelled as horizontal tabular features at a depth approximately equal to the base of the of the Brushy Basin member of the Morrison Formation, a typical depth of intrusion for porphyry in this location (Hunt et al., 1953). Exact shapes of finger-like geometries were modified to most accurately fit calculated to

observed anomaly data. Dike widths and sill thicknesses were modified to provide a best fit. Transect 1 (Figure 50) anomaly values range from negative 50 to positive 500 γ/m and has a large positive anomaly at approximately 380 meters. Transects 2 (Figure 51) and 3 (Figure 52) have several large positive and negative anomalies with anomaly values ranging from negative 250 to positive 250 γ/m, and negative 275 to positive 350 γ/m, respectively. A large anomaly can be traced between transects 2 and 3. Two pipes/tubes can be seen in both transects at approximately the same location on the Sawtooth Ridge intrusion (325m Transect 2, 200m Transect 3).

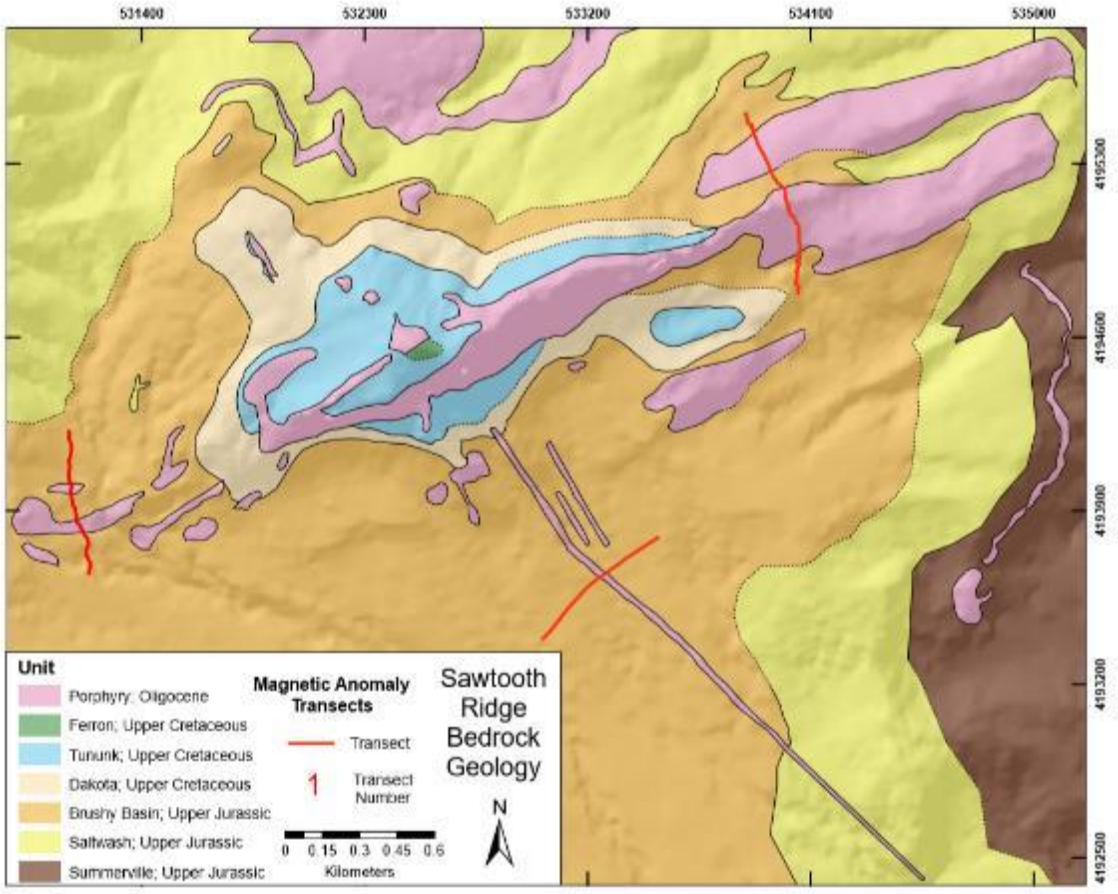

Figure 50. Magnetic transects/traverses plotted atop Sawtooth Ridge bedrock geology.

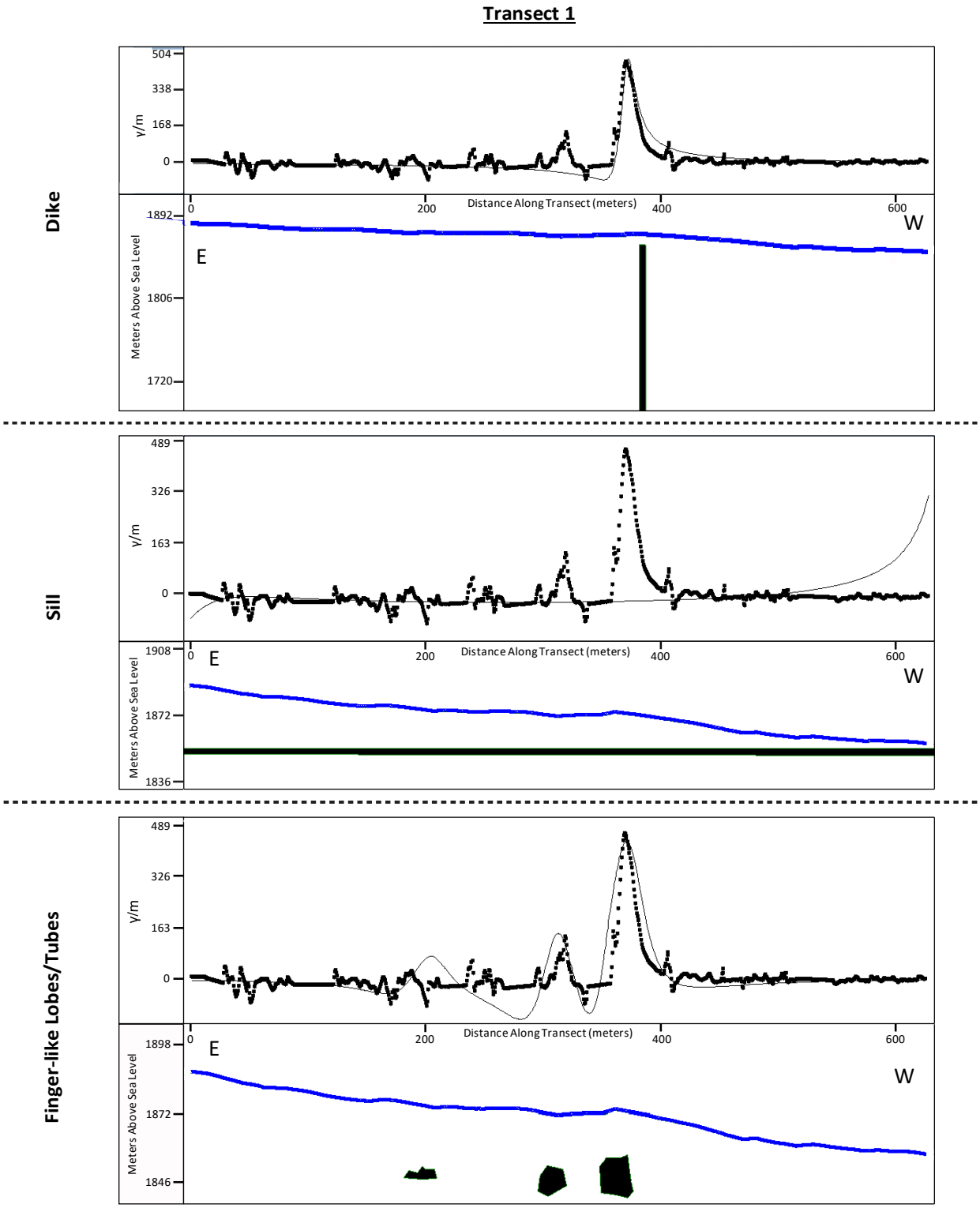

Figure 51. Magnetic anomaly transect 1. Topographic surface is represented by the blue line, measured magnetic data is represented by the thick black line/black points, magnetic curves calculated by the software are represented by the thine black line, and modeled igneous geometries are shown in solid black features outlined in green. Three geometries were modeled.

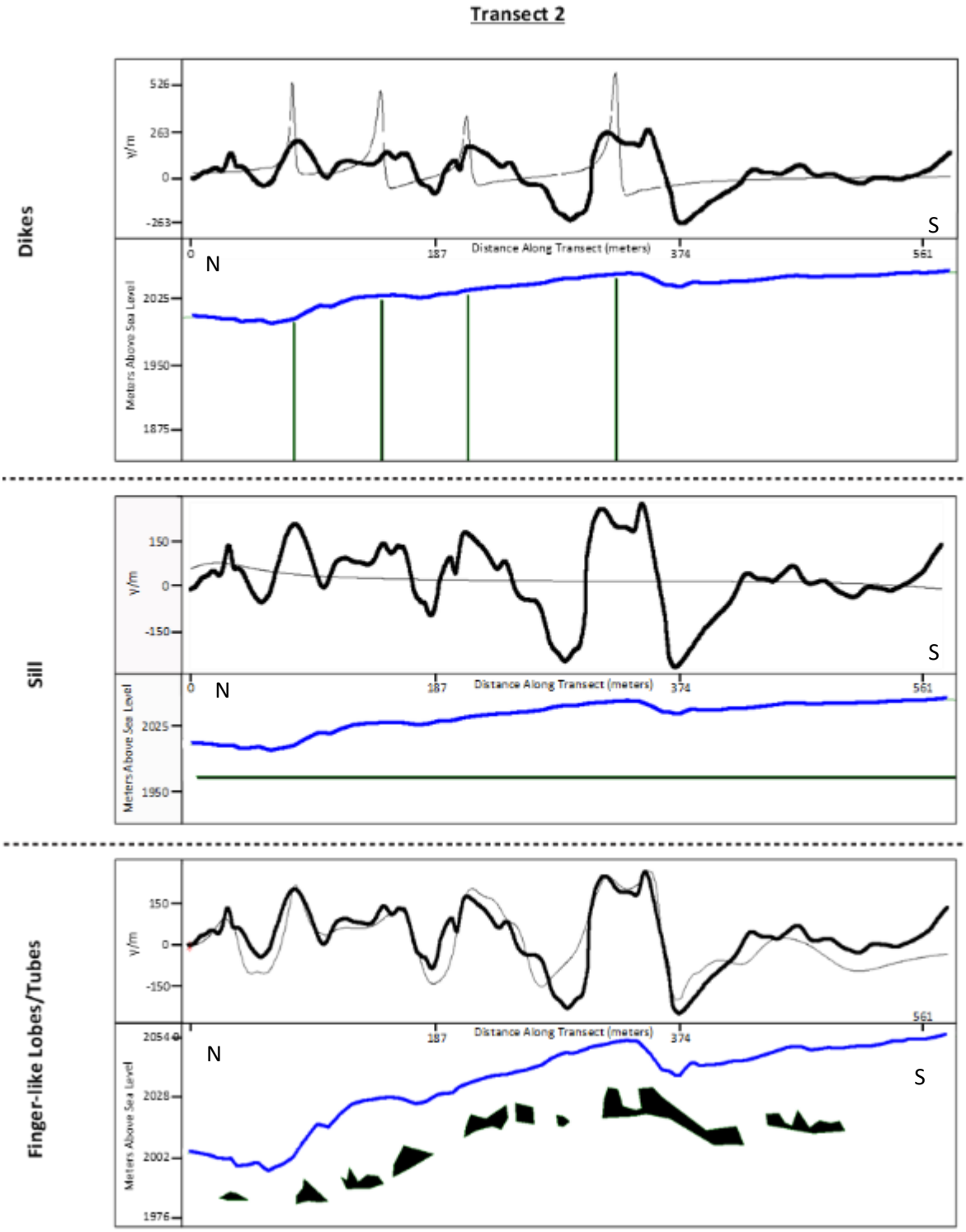

Figure 52. Magnetic anomaly transect 2. Topographic surface is represented by the blue line, measured magnetic data is represented by the thick black line/black points, magnetic curves calculated by the software are represented by the thine black line, and modeled igneous geometries are shown in solid black features outlined in green. Three geometries were modeled.

Transect 3

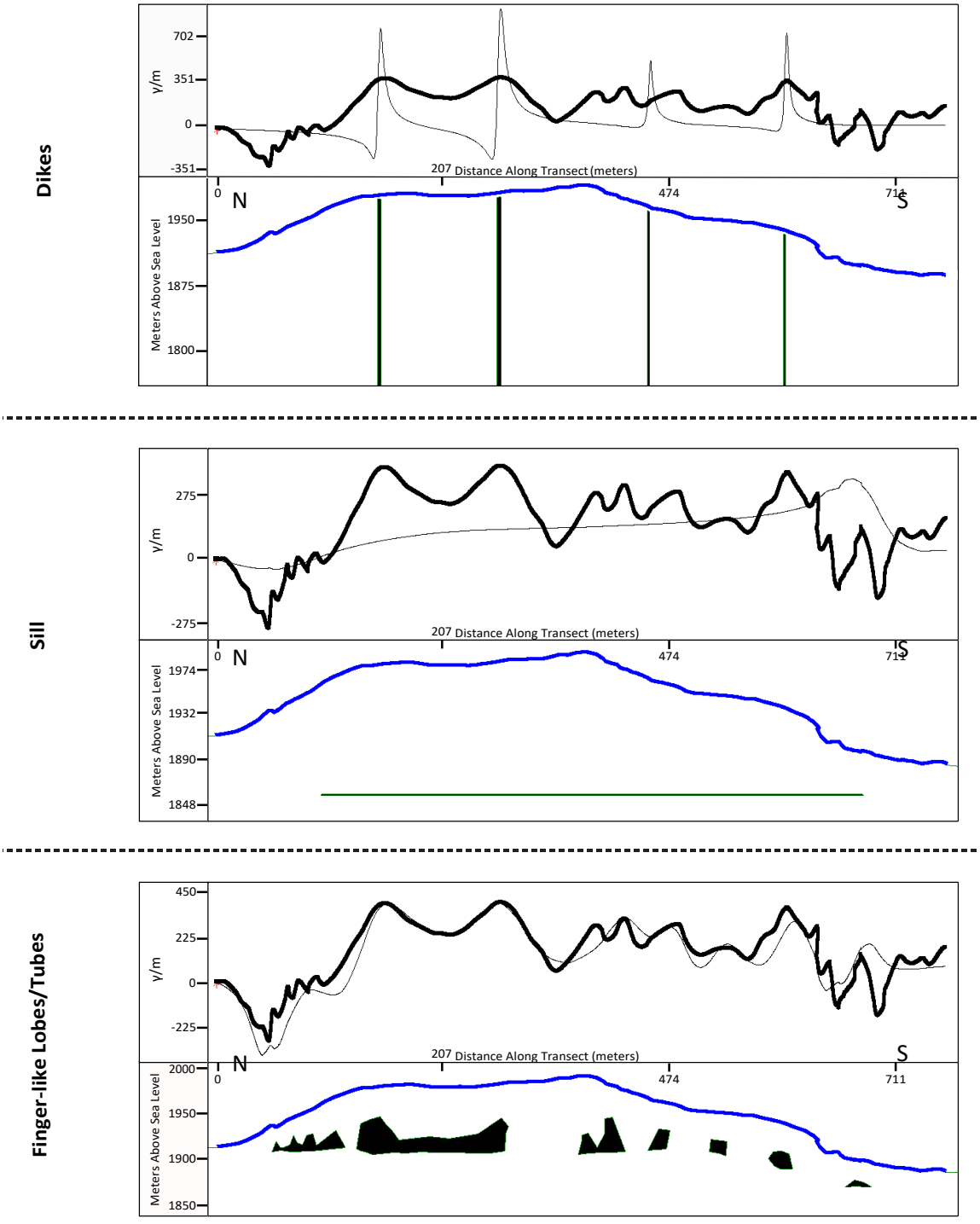

Figure 53. Magnetic anomaly transect 3. Topographic surface is represented by the blue line, measured magnetic data is represented by the thick black line/black points, magnetic curves calculated by the software are represented by the thine black line, and modeled igneous geometries are shown in solid black features outlined in green. Three geometries were modeled.

6. Discussion

a. Field Observations

The geometry of the Sawtooth Ridge intrusion is complex even in map view. There is a mixture of discordant and concordant intrusion-host contacts, and several features extending perpendicularly from the main intrusive feature. To interpret this complexity, it is useful to recall that the transport of magma in the upper crust is often facilitated through pre-existing fractures and that fractures open parallel to the least principal stress directions. As such, the orientation of sheet intrusions is controlled by the orientation of local principal stress directions and, subsequently, the orientation of fracture opening. The variety of intrusion-orientations seen across Sawtooth Ridge suggests that there was a rotation in principal stress directions during emplacement. For example, in the SW portion of the intrusion, the parallel dike-like features could have been emplaced when the minimum principal stress direction was oriented horizontally towards the SE/NW (i.e. magma was propagating vertically and towards the NE/SW) (Fig. 54a). The middle and North eastern portions of the intrusion that display a more tube-like geometry may have been emplaced during a period where the minimum principal stress direction was oriented vertically (i.e. magma was propagating horizontally) (Fig. 54b). Finally, the dike-like features extending perpendicularly from the ridge could have been emplaced when the minimum principal stress direction was oriented horizontally towards the NE/SW (i.e. magma was propagating vertically and towards the SE/NW) (Fig. 54c).

Textural groupings suggest that there are multiple injections of magma responsible for the construction of the Sawtooth Ridge intrusion. While not exact, the spatial distribution of these textures also correlates with the textures and relative ages of L. Murdoch (Fig.18). Similar relative age relationships exist in the interpretive emplacement model of the Sawtooth Ridge intrusion (Fig. 54). However, more detailed observations of outcrop scale textural relationships and igneous-igneous are required to further distinguish separate component intrusions.

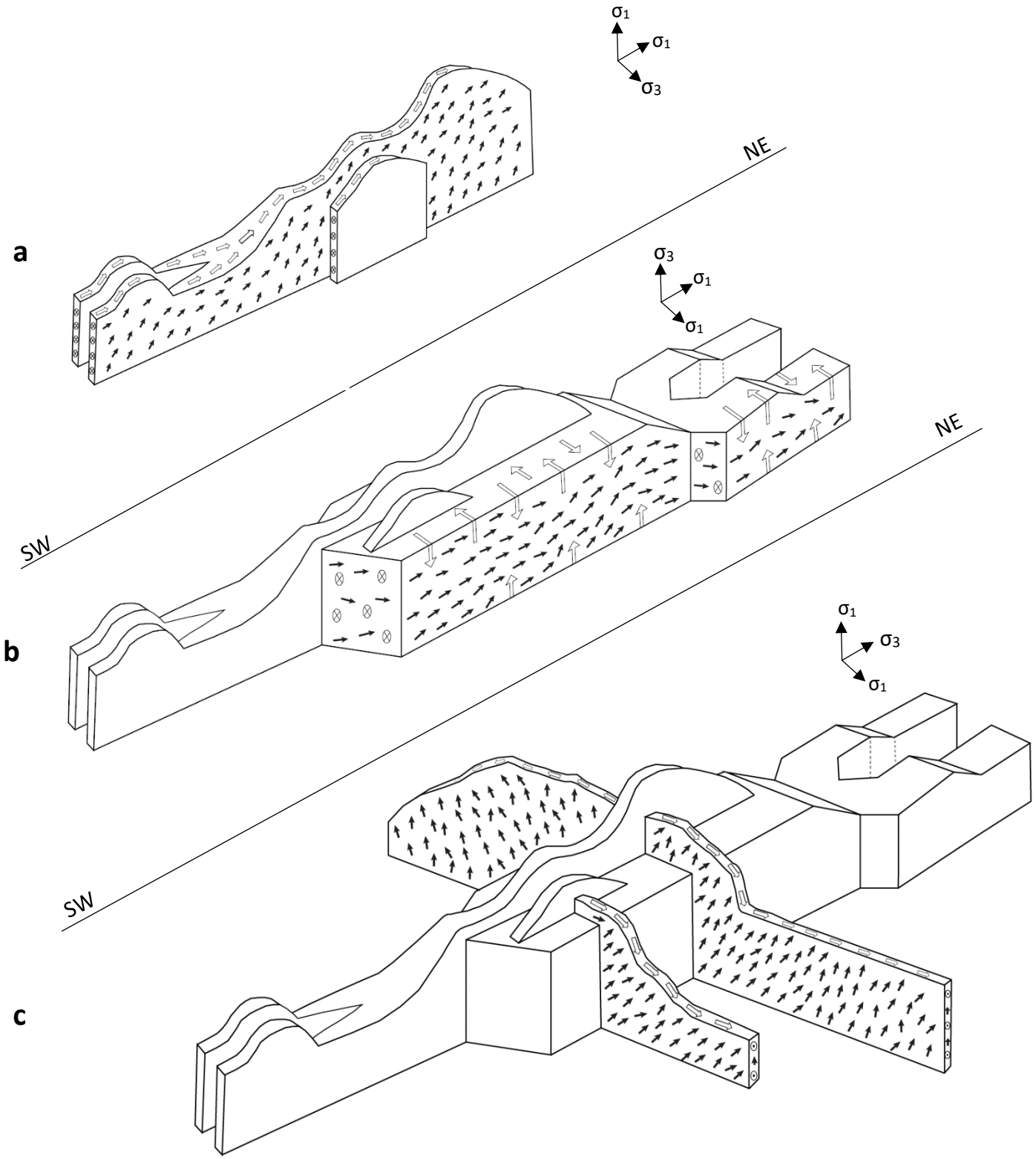

Figure 54. A schematic showing the inferred Sawtooth Ridge emplacement model. Small black arrows represent the internal flow/fabric orientation, hollow arrows represent the flow/fabric orientation near the intrusion margins and on the map surface, and proposed principal stress directions during emplacement are plotted beside each schematic. (a) The first stage of emplacement. Magma was fed from the SW (Mount Hillers intrusive center) and flowed vertically and towards the NE in a dike-like conduit. The minimum stress direction is oriented horizontally towards the SE. (b) The second stage of emplacement. Magma was fed either from the SW or from below, and was flowing sub horizontally toward the NE. This stage also involved the inflation/expansion of a tube-like conduit. The minimum stress direction is oriented vertically. (c) The third stage of emplacement. Magma was fed either from the SW or from below, and magma flowed vertically and towards the SE/NW. The minimum stress direction is oriented horizontally toward the NE/SW.

b. Fabric Analysis

Three techniques were used when analyzing the orientation of petrofabrics in the Sawtooth Ridge intrusion (AMS, SPO, field fabric measurements). The patterns of fabric orientation produced through analysis of AMS are broadly consistent across all three techniques and the general correlation between K_1 orientations can be observed in Figures 47, 48, 49.

The shape and distribution of magnetite grains in the Henry Mountains is assumed to be governed by the primary silicate framework. This suggests that, if AMS fabrics in the Henry Mountains porphyry were created by magma flow, K_1 may correspond to the primary flow axis. Because of the lack of post-emplacement deformation and the apparent alignment between some K_1 lineations and the inferred intrusion plane, these fabrics are interpreted to record primary magma flow. Magnetic mineralogy was not determined in this study, so, it is unknown if magnetite grains are single-domain or multi-domain. As such, the possibility exists that magnetic fabrics are inverse/intermediate and are oriented orthogonally to the primary flow axis, and this should be considered when making interpretations (Ferre, 2003; Magee et al., 2016).

Beginning with the SW end of the Sawtooth Ridge intrusion, magnetic fabrics measured on the parallel, dike-like features trend parallel to the main crest of the intrusion with steep to moderate plunges. This would imply that an upward magma flow to either the SW or the NE (Figure 53a) (Magee et al., 2016). It is more likely that magma was fed from the main Mount Hillers intrusive center and flowed from SW to NE. Moving NE along the intrusions crest. This pattern of flow-axis-parallel lineations (NE-SW) continues until the peak or just beyond the peak. Plunge directions shift closer to moderate/sub-horizontal in this section.

Magnetic lineations become perpendicular to the inferred flow-axis about halfway along the crest of the ridge until the NE end. Plunges remain moderate/sub-horizonal. This rotation in

magnetic lineation orientation from flow-parallel to flow-perpendicular can be interpreted in different ways. First, there may be single domain magnetite producing an inverse magnetic fabric orientation in this area. Second, this orthogonal lineation orientation could suggest the in-situ expansion of a pipe during emplacement. As a tube/pipe expands, the core of the tube will reflect the major flow-axis, however, the edges or margins of the tube will expand in a direction perpendicular to the major direction of flow (Figure 53b). Through increased drag at intrusion contacts, this may have caused magnetic minerals to orient along the expansion-axis rather than the flow-axis. This change in magnetic fabric orientation could also be cause by the incremental compartmentalization of magma flow pathways as the intrusion is constructed. Slight rheologic differences of magma pulses may cause compartmentalized channels for higher velocity magma flow, leading to highly variable fabric orientations across the intrusion (Magee et al., 2016).

Features extending perpendicularly from the main intrusive feature show fabrics trending generally orthogonal to the main crest and parallel to sub-parallel to their inferred planes of intrusion (i.e. dike display lineations trend parallel to down-dip direction and/or the length of the dike) (Figure 53c). This may suggest that they were emplaced separately from the main intrusive body and these fabric orientations are consistent with the geometry of dikes extending perpendicularly from the main body (Magee et al., 2016).

c. Geochemistry

The significant difference in silica concentrations between the 'silica rich' and 'silica poor' groupings suggest the possibility of two separate batches of magma contributing to the construction of the Sawtooth Ridge intrusion. It is unclear whether the separate batches were extracted from the same parent source at different points in a single process of crystallization and differentiation, if they were extracted at the same time and experienced different degrees of chemical evolution before emplacement, or if they were extracted from two different magmatic origins. Because of the seemingly backward relationship between silica concentrations and RRE concentrations, and the overlapping standard deviations of RRE concentrations of the 'silica rich' and 'silica poor' groups, it is unclear whether RRE elements provide any insight.

d. Magnetic Modelling

The forward modelling of magnetic anomaly data can provide constraints on subsurface intrusion geometries. However, interpretations of magnetic data are often subject to ambiguity because different geometric shapes in the subsurface can produce similar perturbations in Earth's magnetic field. As the depth of magnetic anomalies increases, interference from over- or underlying magnetic rocks may also construe interpretations (Abdelrahman et al., 2012). Consequently, magnetic anomaly data often results in simple geometric interpretations, and is much more reliable at shallow intrusion depths.

To mitigate some of this ambiguity, a bulk magnetic susceptibility value for igneous rock was determined with an AGICO magnetic susceptibility bridge. Also, three intrusion geometries (dike, sill, finger-like tubes) were modelled for each dataset in hopes of eliminating improbable interpretations. The dataset in Transect 1 represents a simple planar intrusion (i.e. a

dike) with well-understood geologic and geometric constraints and was included to test the validity of anomaly data and interpretations.

These models show that along each transect a finger-like/tube geometry more accurately reflects the observed magnetic anomalies than dike or sill. They also show that the finger/tube geometries show significant relief and may be more accurately described as tube/dike hybrids. It must be noted that these interpretations of are most valid at shallow intrusions depths and are likely over-simplified when compared to true intrusion geometries.

A more detailed magnetic survey could be conducted to make this technique more useful. The survey conducted here provides information for only two, 2d slices through the Sawtooth Ridge intrusion and surrounding host rock. A high-resolution 3d gridded survey, ideally conducted by satellite or drone, would allow much more detail about geometric constraints. In conjunction with this survey, detailed measurements of magnetic susceptibility in both porphyry and host rock could provide a more realistic model.

e. Sawtooth Ridge and Mount Hillers

The transport of magma through shallow crust, as we know, is facilitated by fractures and the orientation at which they initially open. Fractures open in the direction parallel to least principal stress. Jackson and Pollard (1990) present a generalized model of fault/fracture development that relates principal stress directions to host rock deformation and fracture orientation during the inflation/assembly of Mount Hillers. The earliest stage of laccolith emplacement seen at Mount Hillers is produced when a sill intrudes between two layers and beings to inflate causing elastic deformation in the host rock. This deformation is accommodated by slip between bedding planes in host rock. This first stage of sill inflation produced radial features extending parallel to the dip of host rocks and is the result of primarily isotropic stress conditions. Any significant contrast in

principal stress directions would not allow for the radial symmetry seen in this stage of intrusion. Second, the flexural stage of doming occurs when slippage between layers can no longer accommodate deformation and stretching begins to take over. This causes tangential features to propagate and cross-cut preexisting features while the maximum principal stress is oriented vertically, and the other two principal stress directions are equal in magnitude. The most advanced stage of doming seen at Mount Hillers is caused by the outward inflation of intrusive center. This produced sub-radial intrusive features with steep dips.

The model described by Jackson and Pollard (1990) can be thought of in the context of Sawtooth Ridge. Did these inflation events of Mount Hillers and their subsequent effects on local stress fields have an impact on the emplacement of the Sawtooth Ridge intrusion? The first stage of emplacement inferred for the Sawtooth Ridge intrusion (Fig. 54a) depicts a dike propagating radially from Mount Hillers and non-isotropic stress conditions, while Jackson and Pollard's first stage of doming requires isotropic stress conditions and favors sill formation. The second stage of the Sawtooth Ridge intrusion depicts both radial propagation towards the NE, tangential propagation of the expanding tube, a minimum principal stress direction oriented vertically, and equal horizontal principal stresses. This is very similar to the conditions described n the second stage of doming at Mount Hillers. The third and final stage of emplacement of the Sawtooth Ridge intrusion involves the tangential propagation of dikes and a maximum principal stress direction oriented to the NE. The final stage of doming at Mount Hillers involves both radial and tangential propagation, and due to horizontal inflation has a maximum stress direction oriented horizontally. In summary, the different stages of doming and their subsequent effects on local stress conditions could have possibly influenced the stages of emplacement of the Sawtooth Ridge intrusion. Detailed geochronological data from both intrusive features would be useful in further exploring this idea.

7. Conclusions

Subvolcanic plumbing systems are important drivers of volcanic activity and are often constructed through the successive emplacement of shallow sheet intrusions. Because the processes behind the construction of modern magma systems are difficult to observe directly, it is important to study ancient intrusive complexes now exposed at the surface where the indirect observation of construction processes is possible. The Henry Mountains are group of five, well-exposed upper crustal intrusions have been considered ancient analogues to modern subvolcanic systems. Interpretations made from these intrusive complexes are not by complicated post-emplacement tectonic strain or deformation, making them an ideal location to study the processes behind their construction.

The Sawtooth Ridge intrusion is a relatively understudied igneous body extending NE from the Mount Hillers intrusive center and provides an opportunity to conduct a high-resolution study of the processes behind its construction. Previous studies have constrained the geometries and emplacement histories of nearby, similarly sized intrusions, but previous studies of Sawtooth Ridge intrusion remain inconclusive.

This study aimed to better understand the processes behind the construction of Sawtooth Ridge by providing constraints on its subsurface geometry and emplacement history. A combination of field and laboratory techniques including field observations, major- and trace-element geochemistry, anisotropy of magnetic susceptibility, shape preferred orientation, and magnetic anomaly modelling were used and they test the following hypothesis: Sawtooth ridge is a horizontal pipe-like intrusion fed from the Mount Hillers intrusive center and is constructed from two or more intrusive events.

Field observations provide details about the first-order geometry of the intrusion and the nature of intrusions-host contacts. AMS, SPO, and field fabric measurements were used to quantify petrofabric orientations and provide information on magma flow directions during the last increment of strain recorded before crystallization. Major- and trace-element geochemistry were used to quantify and compare chemical compositions of porphyry at Sawtooth Ridge, providing information on the number of intrusions responsible for its construction and the relative chemical evolutions of these intrusions/injections prior to crystallization. Magnetic anomaly modelling was used to provide basic constraints on subsurface geometry. It must be noted that these techniques and the interpretations that arise from them are subject to ambiguity. Each dataset provides significantly different 3-dimensional information, and, in an attempt to eliminate some of this ambiguity, their interpretations are most useful when considered conjunctively rather than separately. By comparing the results and interpretations of each technique, the following conclusions were made:

The geometry of Sawtooth Ridge is complex and unlike that of many similarly sized intrusions around Mount Hillers (Maiden Creek Sill; Trachyte Mesa Laccolith; Black Mesa Bysmalith). Field observations and laboratory data suggest the geometry of Sawtooth Ridge is a dike/tube hybrid constructed by several intrusions or injections. First, as magma was fed from the Mount Hillers intrusive center a dike conduit extended vertically and towards the NE. Second, as the dike became shallow enough to decrease the overlying compressive pressure, the minimum stress direction was oriented vertically allowing for the horizontal propagation and expansion of the tube/pipe that composes the main body of the intrusion. Third, as the intrusion inflated horizontally and vertically, it may have reached a critical aspect ratio where it was no longer viable to continue inflation and the minimum stress direction became horizontal once

again. This allowed for the propagation of the dike-like features extending perpendicularly from the ridge. The stress conditions during emplacement of the Sawtooth Ridge intrusion may have been influenced by the progressive doming of the Mount Hillers intrusive center. However, detailed geochronological data from both intrusions would aid in making this correlation. More detailed observations of textures and igneous-igneous contacts would be beneficial in mapping component intrusions that constructed Sawtooth Ridge. More detailed geochemical and textural analyses should be done to be certain which phase of magnetite is present at Sawtooth Ridge, the chemical and petrologic evolution of the magmas contributing to the intrusion, and the number and nature of sources/injections of magma.

References:

Abdelrahman, EM, Abo-Ezz, ER, and Essa, KS, 2012, Parametric inversion of residual magnetic anomalies due to simple geometric bodies: Exploration Geophysics, v. 43, no. 3, p. 178-189.

Anderson, EM, 1951, The dynamics of faulting and dyke formation with applications to Britain (Second ed.): Oliver and Boyd Ltd., Edinburgh and London.

Anderson, TL, 2005, Fracture mechanics; fundamentals and applications (third edition): Taylor and Francis Group.

Broda, RJ, 2014, Geometry and progressive development of a shallow crustal intrusive complex, Mount Hillers, Henry Mountains, Utah. Master's Thesis: East Carolina University, 111 p.

Brown, EH, and McClelland, WC, 2000, Pluton emplacement by sheeting and vertical ballooning in part of the Southeast Coast plutonic complex, British Columbia: Geological Society of America Bulletin, v. 112, p. 708–719.

Coleman, DS, Gray, W, and Glazner, AF, 2004, Rethinking the emplacement and evolution of zoned plutons: Geochronologic evidence for incremental assembly of the Tuolumne Intrusive Suite, California: Geology, v. 32, no. 5, p. 433-436.

Fridleifsson, IB, 1977. Distribution of large basaltic intrusions in the Icelandic crust and the nature of the layer 2–layer 3 boundary: Geol. Soc. Amer. Bull. 88, 1689–1693.

Gilbert, GK, 1877, Report on the geology of the Henry Mountains: U.S. Geological Survey, 170 p.

Glazner, AF, Bartley, JM, Coleman, DS, Gray, W and Taylor, RZ, 2004. Are plutons assembled over millions of years by amalgamation from small magma chambers? GSA Today: v.14, p.4–11.

Harrison, TM, and Clarke, GKC, 1979, A model of the thermal effects of igneous intrusion and uplift as applied to Quottoon pluton, British Columbia: Canadian Journal of Earth Sciences, v. 16, p. 411–420.

Horsman, E, Broda, RJ, Gwyn, NZ, Maurer, EA, Thornton, ED, and Ward, MD, 2018. Progressive construction of laccolithic intrusive centers, Henry Mountains, Utah, U.S.A: Breitkreuz, C. & Rocchi, S. (eds), Physical Geology of Shallow Magmatic Systems, 327-347., doi: 10.1007/978-3-319-14084-1.

Horsman, E, Morgan, S, de Saint-Blanquat, M, Habert, G, Nugent, A, Hunter, RA, and Tikoff, B, 2010, Emplacement and assembly of shallow intrusions from multiple magma pulses, Henry Mountains, Utah: Earth and Environmental Science Transactions of the Royal Society of Edinburgh, v. 100, no. 1-2, p. 117–132.

Horsman, E., Morgan, S., de Saint Blanquat, M. & Tikoff, B., 2010. Emplacement and assembly of shallow intrusions, Henry Mountains, Utah. Field trip guidebook for the LASI 4 conference, 22-26 September 2010, Moab and Henry Mountains, Utah.

Horsman, E, Tikoff, B, and Morgan, SS, 2005. Emplacement-related fabric and multiple sheets in the Maiden Creek sill, Henry Mountains, Utah, USA: Journal of Structural Geology, v. 26, p. 1426-1444.

Hunt, C, Averitt, P, and Miller, RL, 1953. Geology and geography of the Henry Mountains region, Utah. US Geological Survey: Professional Paper 228.

Hunt, CB, 1956, Cenozoic Geology of the Colorado Plateau: US Geological Survey Professional Paper 279, 99 p.

Jackson, MD, and Pollard, DD, 1988, The laccolith-stock controversy: New results from the southern Henry Mountains, Utah: Geological Society of America Bulletin, v. 100, no. 1, p. 117–139.

Jackson, M.D. and Pollard, D.D., 1990. Flexure and faulting of sedimentary host rocks during growth of igneous domes, Henry Mountains, Utah. Journal of Structural Geology, 12(2), pp.185-206.

Johnson, AM, and Pollard, DD, 1973, Mechanics of growth of some laccolithic intrusions in the Henry Mountains, Utah, I: Field observations, Gilbert's model, physical properties and flow of the magma: Tectonophysics, v. 18, no. 3–4, p. 261–309.

Kavanagh, JL, Menand, T, and Sparks, RSJ, 2006, An experimental investigation of sill formation and propagation in layered elastic media: Earth and Planetary Science Letters, v. 245, no. 3–4, p. 799–813.

Knight, MD, and Walker, GPL, 1988, Magma flow directions in dikes of the Koolau Complex, Oahu, determined from magnetic fabric studies: Journal of Geophysical Research: Solid Earth, v. 93, no. B5, p. 4301–4319.

Launeau, P, Bouchez, JL, and Benn, K, 1990. Shape preferred orientation of object populations: automatic analysis of digitized images: Tectonophysics 180, 201-211.

Launeau, P, and Cruden, AR, 1998. Magmatic fabric acquisition mechanisms in a syenite: Results of a combined anisotropy of magnetic susceptibility and image analysis study: Journal of Geophysical Research 103, 5067-5089.

Launeau, P, and Robin, PY, 2005. Determination of fabric and strain ellipsoids from measured sectional ellipses - implementation and application: Journal of Structural Geology 27, 2223-2233.

Launeau, P, Archanjo, CJ, Picard, D, Arbaret, L, and Robin, PY, 2010. Two- and three-dimensional shape fabric analysis by the intercept method in grey levels: Tectonophysics 492, 230-239.

Magee, C, O'Dricscoll, B, Petronis, MS, and Stevenson, CTE, 2016. Three-dimensional magma flow dynamics within subvolcanic sheet intrusions: Geosphere, v. 12, n. 3

Maurer, EA, 2015. Geometry and construction history of the Copper Ridge laccolith, Mount Ellen, Henry Mountains, Utah. Master's Thesis, East Carolina University, 122 p.

McNulty, BA, Tong, W, and Tobisch, OT, 1996, Assembly of a dike-fed magma chamber: The Jackass Lakes pluton, central Sierra Nevada, California: Geological Society of America Bulletin, v. 108, p. 926–940.

Menand, T, 2011. Physical controls and depth of emplacement of igneous bodies: A review: Tectonophysics, 500(1), 11-19.

Morgan, S, Stanik, A, Horsman, E, Tikoff, B, Saint-Blanquat (de), M, and Habert, G, 2008. Emplacement of multiple magma sheets and wall rock deformation: Trachyte Mesa intrusion, Henry Mountains, Utah. Journal of Structural Geology, v. 30, n. 4, p. 491-512.

Murdoch, L, unpublished mapping.

Nelson, ST, Davidson, JP, and Sullivan, KR, 1992. New age determinations of central Colorado Plateau laccoliths, Utah: Recognizing disturbed K-Ar systematics and reevaluating tectonomagmatic relationships. Geological Society of America Bulletin, v. 104, p. 1547–1560.

Nelson, ST, and Davidson, JP, 1993, Interactions between mantle-derived magmas and mafic crust, Henry Mountains, Utah: Journal of Geophysical Research: Solid Earth, v. 98, no. B2, p. 1837–1852.

Parsons, T, Sleep, NH, and Thompson, GA, 1992. Host rock rheology controls on the emplacement of tabular intrusions: implications for underplating of extending crust: Tectonics 11, 1348–1356.

Paterson, SR, Fowler Jr., TK, Schmidt, KL, Yoshinobu, AS, Yuan, ES, and Miller, RB, 1998. Interpreting magmatic fabric patterns in plutons: Lithos 44, 53–82.

Petford, N, Cruden, AR, McCaffrey, KJW, and Vigneresse, JL, 2000, Granite magma formation, transport and emplacement in the Earth's crust: Nature, v. 408, no. 6813, p. 669–673.

Petford, N, Kerr, RC, and Lister, JR, 1993, Dike transport of granitoid magmas: Geology, v. 21, no. 9, p. 845–848.

Pollard, DD, Muller, OH, and Dockstader, DR, 1975, The form and growth of fingered sheet intrusions: Geological Society of America Bulletin, v. 86, no. 3, p. 351–363.

Rochette, P, Jackson, M, and Aubourg, C, 1992, Rock magnetism and the interpretation of anisotropy of magnetic susceptibility: Reviews of Geophysics, v. 30, no. 3, p. 209–226

Saint-Blanquat (de), M, Habert, G, Horsman, E, Morgan, S., Tikoff, B, Launeau, P, and Gleizes, G, 2006, Mechanisms and duration of non-tectonically assisted magma emplacement in the upper crust: The Black Mesa pluton, Henry Mountains, Utah: Tectonophysics, v. 428, no. 1-4, p. 1–31.

Saint-Blanquat (de), M, Horsman, E, Habert, G, Morgan, S, Vanderhaeghe, O, Law, R and Tikoff, B, 2011. Multiscale magmatic cyclicity, duration of pluton construction, and the paradoxical relationship between tectonism and plutonism in continental arcs. Tectonophysics, v. 500, p. 22-33.

Saint-Blanquat (de), M, Law, RD, Bouchez, JL and Morgan, SS, 2001. Internal structure and emplacement of the Papoose Flat pluton: An integrated structural, petrographic, and magnetic susceptibility study. Geological Society of America Bulletin, v. 113(8), p.976-995.

Thomson, K, and Hutton, D, 2004. Geometry and growth of sill complexes: insights using 3D seismic from the North Rockall Trough: Bull. Volcanol. 66, 364–375.

Vigneresse, JL, and Clemens, JD, 2000, Granitic magma ascent and emplacement: Neither diapirism nor neutral buoyancy: Geological Society, London, Special Publications, v. 174, no. 1, p. 1–19.

Weymouth, JW, and Nickel, R, 1977. A magnetometer survey of the Knife River Indian villages: Midwest Archeological Center, Lincoln, Nebraska.

Wetmore, P.H., Connor, C.B., Kruse, S.E., Callihan, S., Pignotta, G., Stremtan, C. and Burke, A., 2009. Geometry of the Trachyte Mesa intrusion, Henry Mountains, Utah: Implications for the emplacement of small melt volumes into the upper crust. Geochemistry, Geophysics, Geosystems, 10(8).

Wilson, P.I., McCaffrey, K.J. and Holdsworth, R.E., 2019. Magma-driven accommodation structures formed during sill emplacement at shallow crustal depths: The Maiden Creek sill, Henry Mountains, Utah. Geosphere, 15(4), pp.1368-1392.

Appendix A: Geochemistry Data

Group 1 Geochemistry Data - Major Element							
	Sample name						
Major Element (wt%)	SR67	SR80	SR81	SR89	SR92	SR95	Average
SiO_2	61.39	61.06	61.43	60.81	61.54	61.33	61.26
Al_2O_3	18.08	18.09	18.28	18.06	17.83	17.72	18.01
Fe_2O_3	5.06	4.96	4.98	5.17	5.26	5.03	5.07
MgO	1.36	1.3	1.2	1.37	1.35	1.32	1.31
CaO	5.66	5.85	5.39	4.54	5.57	5.76	5.46
Na_2O	4.44	4.6	4.63	5	4.66	4.43	4.62
K_2O	1.96	1.94	2.02	1.93	1.89	1.99	1.95
TiO_2	0.49	0.49	0.48	0.48	0.5	0.49	0.48
P_2O_5	0.19	0.19	0.19	0.22	0.22	0.2	0.20
MnO	0.15	0.14	0.14	0.19	0.15	0.13	0.15
Cr_2O_3	0.0030	<0.0020	0.0030	0.0030	<0.0020	0.0020	0.0027
LOI	0.90	1.10	10	20	0.80	1.30	1.18
Total	99.68	99.72	99.74	99.77	99.77	99.70	99.73

Group 2 Geochemistry Data - Major Element							
	Sample name						
Major Element (wt%)	SR57	SR71	SR75	SR86	SR90	SR91	Average
SiO_2	59.07	59.94	59.37	59.19	59.49	59.04	59.35
Al_2O_3	17.99	16.97	17.87	17.41	17.66	17.58	17.58
Fe_2O_3	5.32	4.73	5.33	5.07	5.50	5.37	5.22
MgO	1.37	1.38	1.57	1.41	1.66	1.43	1.47
CaO	5.54	5.99	6.18	6.23	6.04	6.16	6.02
Na_2O	4.69	4.14	4.06	4.17	4.08	4.26	4.23
K_2O	1.92	1.93	1.96	1.87	1.84	1.83	1.89
TiO_2	0.54	0.49	0.54	0.52	0.52	0.53	0.52
P_2O_5	0.22	0.20	0.22	0.21	0.22	0.22	0.21
MnO	0.12	0.12	0.15	0.15	0.15	0.16	0.14
Cr_2O_3	0.0030	<0.0020	0.0030	0.0030	0.0020	0.0030	0.0028
LOI	30	3.80	2.50	3.50	2.60	3.10	3.083
Total	99.78	99.69	99.75	99.73	99.76	99.68	99.73

Group 1 Geochemistry Data - Trace Element							
	Sample name						
Trace Element (PPM)	SR67	SR80	SR81	SR89	SR92	SR95	Average
Sc	7	6	6	7	7	7	6.67
Ba	913	927	942	909	912	963	927.67
Be	1	<1	<1	2	3	1	1.75
Co	6.3	6.5	6.5	6.8	6.9	6.5	6.58
Cs	1.4	1.3	1.6	1.5	1.1	0.5	1.23
Ga	18.7	19.1	19	19.1	19.1	18.5	18.92
Hf	3.6	3.8	3.6	3.7	3.5	3.7	3.65
Nb	5.4	5.3	5.3	5.4	5.8	5.1	5.38
Rb	29.3	30.9	31.8	26	28.2	28.4	29.10
Sn	<1	<1	<1	<1	<1	<1	-
Sr	862.3	847.4	872.6	784.1	856.3	911.5	855.70
Ta	0.3	0.3	0.3	0.4	0.4	0.2	0.32
Th	4.4	4.1	3.6	4.1	3.9	3.4	3.92
U	1.5	1.6	1.3	1.6	1.5	1.2	1.45
V	69	67	67	62	65	74	67.33
W	<0.5	<0.5	0.6	0.7	<0.5	<0.5	-
Zr	135.1	136.8	142.9	136.9	138.6	142.6	138.82
Y	19.8	19.5	19.1	21.3	23	17.4	20.017
La	23.5	20.7	18.9	20.2	20	19.3	20.43
Ce	46.6	39.5	37.5	40.8	39.9	37.9	40.37
Pr	5.51	4.89	4.54	5	4.93	4.61	4.91
Nd	23.3	20.2	18.8	20	20.3	20.3	20.48
Sm	4.44	4.01	3.76	4.26	4.27	4.12	4.14
Eu	1.3	1.26	1.18	1.33	1.4	1.23	1.28
Gd	4.03	3.85	3.66	4.09	4.17	3.63	3.91
Tb	0.6	0.58	0.56	0.63	0.63	0.56	0.59
Dy	3.57	3.43	3.46	3.79	3.91	3.14	3.55
Ho	0.71	0.72	0.74	0.8	0.84	0.66	0.75
Er	2.1	2.05	2.02	2.36	2.48	2.07	2.18
Tm	0.32	0.31	0.3	0.34	0.35	0.28	0.32
Yb	2.03	2.06	1.99	2.4	2.38	1.89	2.13
Lu	0.3	0.31	0.3	0.37	0.37	0.29	0.32
Mo	0.2	0.3	0.3	0.4	0.2	0.3	0.28
Cu	11.3	12.7	9	3.4	10.9	9.5	9.47
Pb	4	5.5	5	3.8	5.4	7.3	5.17
Zn	51	58	56	101	56	66	64.67
Ni	3.5	3	3.4	3.8	2.9	2.9	3.25
As	0.6	0.7	2.4	1.9	0.8	1	1.23

Group 1 Geochemistry Data - Trace Element Continued							
	Sample name						
Trace Element (PPM)	SR67	SR80	SR81	SR89	SR92	SR95	Average
Cd	0.1	<0.1	<0.1	<0.1	<0.1	<0.1	0.1
Sb	<0.1	<0.1	<0.1	<0.1	<0.1	<0.1	-
Bi	<0.1	<0.1	<0.1	<0.1	<0.1	<0.1	-
Ag	<0.1	<0.1	<0.1	<0.1	<0.1	<0.1	-
Au (PPB)	<0.5	<0.5	<0.5	0.5	<0.5	<0.5	0.5
Hg	<0.01	<0.01	<0.01	<0.01	<0.01	<0.01	-
Tl	<0.1	<0.1	<0.1	<0.1	<0.1	<0.1	-
Se	<0.5	<0.5	<0.5	<0.5	<0.5	<0.5	-

Group 2 Geochemistry Data - Trace Element							
	Sample name						
Trace Element (PPM)	SR57	SR71	SR75	SR86	SR90	SR91	Average
Sc	8	7	7	7	7	7	7.17
Ba	891	882	899	939	910	858	896.50
Be	<1	3	2	<1	1	<1	2.0
Co	4.6	6.3	7.1	7.1	7.1	7.3	6.58
Cs	0.9	0.7	0.8	0.6	0.9	1.2	0.85
Ga	18.5	18.2	18.7	18.9	18.6	18.9	18.63
Hf	3.5	3.4	3.6	3.6	3.7	3.4	3.53
Nb	5.6	4.6	6	5.6	5.5	6	5.55
Rb	32.6	28.3	28.4	29.4	27.9	27.4	29.0
Sn	4	<1	<1	<1	<1	<1	4.0
Sr	780.7	811.1	816.3	897.6	868.3	854	838
Ta	0.3	0.3	0.3	0.3	0.4	0.4	0.33
Th	4	3.2	4.9	4.8	4.5	4.2	4.27
U	1.5	1.3	1.7	1.5	1.7	1.4	1.52
V	65	73	68	77	68	69	70
W	<0.5	<0.5	<0.5	<0.5	<0.5	<0.5	-
Zr	129.4	133.4	146.2	144.2	139.8	137.3	138.38
Y	23.2	16.2	23.9	22.4	21	22.9	21.6
La	19.5	17.6	24.4	23.9	21.7	19.7	21.13
Ce	40.1	33.9	50.2	45.1	43.7	39.5	42.083
Pr	4.76	4.16	5.82	5.53	5.27	4.88	5.07
Nd	20.2	17.9	24.3	22.8	21.7	20.3	21.20
Sm	4.34	3.54	4.87	4.66	4.32	4.53	4.38
Eu	1.39	1.07	1.5	1.41	1.43	1.37	1.36
Gd	4.34	3.4	4.64	4.41	4.27	4.44	4.25
Tb	0.67	0.48	0.7	0.64	0.63	0.68	0.63
Dy	4.35	2.92	4.34	4.07	3.66	3.9	3.87
Ho	0.83	0.56	0.89	0.77	0.78	0.85	0.78
Er	2.57	1.79	2.59	2.37	2.22	2.75	2.38
Tm	0.37	0.24	0.36	0.35	0.33	0.37	0.34
Yb	2.43	1.76	2.52	2.27	2.37	2.53	2.31
Lu	0.4	0.25	0.37	0.35	0.35	0.38	0.35
Mo	0.4	0.3	0.4	0.3	0.3	0.2	0.32
Cu	12.4	14.8	7.1	12	12.7	10.5	11.58
Pb	3.6	1.9	3.3	6.7	2.5	2.4	3.4
Zn	65	64	72	82	76	88	74.5
Ni	3.3	3.7	4	6.9	5	5.4	4.72
As	16.7	<0.5	1.4	1	1.4	<0.5	5.13

Group 2 Geochemistry – Trace Element Continued							
	Sample name						
Trace Element (PPM)	SR57	SR71	SR75	SR86	SR90	SR91	Average
Cd	<0.1	<0.1	<0.1	0.1	<0.1	0.4	0.25
Sb	<0.1	<0.1	0.2	<0.1	<0.1	<0.1	0.2
Bi	<0.1	<0.1	<0.1	<0.1	<0.1	<0.1	-
Ag	<0.1	<0.1	<0.1	<0.1	<0.1	<0.1	-
Au (PPB)	<0.5	<0.5	<0.5	<0.5	<0.5	0.6	0.6
Hg	<0.01	<0.01	<0.01	<0.01	<0.01	<0.01	-
Tl	<0.1	<0.1	<0.1	<0.1	<0.1	<0.1	-
Se	<0.5	<0.5	<0.5	<0.5	<0.5	<0.5	-

Appendix B: Anisotropy of Magnetic Susceptibility Data

			AMS Data							
Name	UTM E	UTM N	Num. Spec.	K1	K2	K3	K1dec	K1inc	K2dec	K2inc
	Zone 12N (NAD83)									
SR53	531827	4194934	4	1.013	0.999	0.988	123.3	32.1	218.5	8.2
SR55	532173	4194809	6	1.006	1.004	0.990	223.3	34.1	72.0	52.4
SR57	532433	4194563	6	1.007	0.999	0.994	302.9	18.5	203.5	26.0
SR61	535057	4195759	5	1.010	1.006	0.984	44.9	19.8	177.4	61.9
	534702	4195205	6	1.008	1.004	0.988	349.1	58.1	203.8	27.1
SR71	533933	4195385	6	1.007	1.001	0.992	1.9	32.0	227.4	48.3
SR73	533771	4195377	6	1.012	1.002	0.987	49.0	6.8	146.0	45.4
SR74	533921	4195170	6	1.011	1.001	0.988	138.9	18.2	236.2	21.3
SR75	534851	4194832	6	1.009	0.999	0.991	41.8	36.9	191.5	49.0
SR77	532589	4194497	6	1.022	1.005	0.972	81.6	33.9	226.1	50.4
SR78	532712	4194625	6	1.011	1.001	0.988	269.5	21.6	1.8	5.8
SR79	532806	4194723	6	1.014	0.998	0.987	321.8	4.6	211.2	77.2
SR80	533089	4194846	7	1.007	1.001	0.992	307.7	24.2	182.7	51.9
SR81	533297	4194899	6	1.005	1.001	0.994	283.2	18.7	187.6	16.3
SR82	532252	4194448	6	1.012	1.000	0.987	30.8	1.1	300.7	0.7
SR83	532137	4194352	5	1.011	0.999	0.990	78.4	46.0	171.4	2.8
SR84	531792	4194416	6	1.008	1.002	0.990	129.4	42.7	315.9	47.2
SR85	533030	4193807	6	1.008	1.001	0.990	206.4	29.3	32.0	60.6
SR87	532750	4193946	6	1.005	1.003	0.992	316.1	0.0	226.1	72.7
SR88	533096	4194467	6	1.008	0.999	0.994	154.9	45.6	64.0	0.9
SR89	533510	4194324	6	1.007	0.997	0.995	192.7	7.4	2.9	82.5
SR90	533944	4192932	6	1.009	1.001	0.990	125.1	47.2	11.9	20.1
SR91	532148	4195333	6	1.009	0.998	0.993	348.6	3.67	78.7	1.6
SR92	531421	4193871	6	1.005	0.999	0.996	305.0	86.6	169.9	2.4
SR93	531264	4193892	6	1.007	1.001	0.992	29.4	58.9	127.5	4.9
SR94	531218	4193979	6	1.013	1.002	0.985	68.2	9.9	189.0	71.1
SR95	530883	4193787	6	1.014	0.998	0.988	262.4	9.6	3.5	48.8

AMS Data Cont.								
Name	K3dec	K3inc	Km SI	K_m 1S*	L	F	P’	T
SR53	321.2	56.6	0.0155	0.00137	1.014	1.011	1.025	-0.127
SR55	323.0	14.0	0.00708	0.000213	1.001	1.014	1.017	0.807
SR57	64.3	57.2	0.000284	0.00000768	1.008	1.005	1.013	-0.214
SR61	307.8	19.0	0.0132	0.000138	1.004	1.022	1.029	0.672
SR67	105.7	15.6	0.00536	0.000350	1.005	1.015	1.021	0.501
SR71	107.8	23.7	0.00634	0.000325	1.006	1.009	1.015	0.178
SR73	312.4	43.8	0.00808	0.000311	1.010	1.015	1.025	0.191
SR74	11.7	61.4	0.00787	0.000379	1.010	1.014	1.024	0.174
SR75	299.9	15.3	0.0107	0.000331	1.010	1.008	1.018	-0.098
SR77	339.1	17.9	0.000390	0.0000150	1.017	1.034	1.051	0.330
SR78	105.9	67.5	0.00561	0.000378	1.010	1.013	1.023	0.151
SR79	52.8	11.9	0.00966	0.000241	1.016	1.011	1.027	-0.208
SR80	51.2	27.5	0.00810	0.000248	1.006	1.009	1.015	0.242
SR81	59.2	64.8	0.00699	0.000765	1.003	1.007	1.011	0.368
SR82	178.7	88.7	0.00125	0.000384	1.012	1.013	1.026	0.059
SR83	264.1	43.8	0.00811	0.000441	1.011	1.009	1.021	-0.90
SR84	222.4	3.3	0.00903	0.000180	1.006	1.013	1.019	0.367
SR85	297.7	2.4	0.00136	0.000233	1.007	1.011	1.018	0.198
SR87	46.2	17.3	0.00106	0.000465	1.002	1.010	1.013	0.665
SR88	333.1	44.4	0.00676	0.000187	1.009	1.005	1.015	-0.267
SR89	102.6	1.3	0.00774	0.000216	1.010	1.002	1.013	-0.701
SR90	266.5	35.9	0.0106	0.0000699	1.008	1.010	1.019	0.099
SR91	192.9	86.1	0.00899	0.000257	1.010	1.005	1.016	-0.374
SR92	79.8	2.4	0.00926	0.000377	1.006	1.003	1.009	-0.342
SR93	220.4	30.7	0.00830	0.000228	1.006	1.009	1.015	0.185
SR94	335.4	15.9	0.00109	0.000282	1.012	1.017	1.029	0.199
SR95	164.3	39.6	0.0124	0.000152	1.016	1.010	1.027	-0.216

*One standard devaition

Appendix C: Shape Preferred Orientation Data

SPO Data									
Name	UTM E	UTM N	K1	K2	K3	K1dec	K1inc	K2dec	K2inc
	Zone 12N (NAD83)								
SR55	532172	4194808	1.055	0.999	0.949	90.6	22.8	223.2	58.1
SR61	535057.8	4195759.9	1.019	1.005	0.976	231.9	3.8	322.1	3.9
SR71	533933.4	4195385.4	1.037	1.009	0.956	171.5	13.5	76.7	19.0
SR74	533921.4	4195170.2	1.021	1.002	0.978	352.2	52.4	256.2	4.6
SR78	532712.2	4194625.6	1.134	0.993	0.888	286.1	28.1	167.5	41.9
SR79	532806.3	4194723.1	1.025	1.002	0.974	162.5	6.3	253.4	7.9
SR85	533030.4	4193807.8	1.064	0.974	0.966	322.8	14.3	177.1	72.8
SR87	532750.3	4193946.5	1.050	1.001	0.951	50.6	66.0	182.5	16.5
SR88	533096.2	4194467.4	1.033	0.994	0.974	339.8	47.4	92.5	19.5
SR92	531421.1	4193871.3	1.025	1.015	0.960	309.9	11.8	209.1	41.8
SR93	531264.9	4193892.6	1.031	1.007	0.963	248.9	33.2	340.5	2.5
SR94	531218.9	4193979	1.037	1.008	0.957	18.6	44.8	258.8	26.6

SPO Data Cont.							
Name	K3dec	K3inc	√F	L	F	P’	T
SR55	351.3	21.0	1.6%	1.056	1.053	1.111	-0.025
SR61	97.3	84.6	2.0%	1.014	1.030	1.045	0.371
SR71	294.8	66.3	3.0%	1.027	1.056	1.086	0.342
SR74	162.8	37.2	1.4%	1.020	1.024	1.045	0.104
SR78	38.2	35.1	1.7%	1.142	1.118	1.277	-0.089
SR79	34.4	79.9	3.7%	1.023	1.029	1.053	0.123
SR85	55.2	9.3	2.0%	1.093	1.008	1.114	-0.831
SR87	277.6	16.9	1.5%	1.049	1.052	1.104	0.025
SR88	197.4	36.1	1.3%	1.040	1.020	1.062	-0.324
SR92	52.3	45.8	2.5%	1.010	1.057	1.073	0.696
SR93	74.3	56.7	1.5%	1.024	1.045	1.072	0.293
SR94	149.5	33.4	1.3%	1.029	1.053	1.085	0.292